AN ANALYSIS OF THE NEUTRAL BEAM INJECTOR PENETRATIONS IN CURRENT TOKAMAK FUSION REACTOR DESIGNS

41

A Thesis

Submitted to the Graduate Faculty of the
Louisiana State University and
Agricultural and Mechanical College
in partial fulfillment of the
requirements for the degree of
Master of Science

in

The Department of Nuclear Engineering

by
Joe Lynn Burton
B.S., Mississippi State University, 1973
December 1979

DEDICATED TO KARIN

ACKNOWLEDGEMENT

The author wishes to express his gratitude to Mr. Robert Kropp of Gibbs & Hill, Inc., Dr. M. A. Abdou of Argonne National Laboratory, Mr. T. J. Woods of General Atomic Company, and Mr. Eliot Whitesides of Oak Ridge National Laboratory for their assistance in obtaining and clarifing resource materials. An additional measure of appreciation is due my employer, Gulf States Utilities Company, for their financial aid and patience during this course of study. Lastly, the author gives special thanks to Dr. Robert E. Miles for his assistance and guidance in this endeavor.

FOREWORD

At the outset, it should be mentioned that this thesis will contain considerable background information on such subjects as fusion reactor design, computer-aided shielding analysis, and particle accelerator theory. While some of these digressions may not seem entirely pertinent to this presentation, it must be remembered that these are areas of an esoteric nature, and are somewhat removed from the mainstream of current nuclear engineering practice. If the inclusion of this additional information clarifies the reader's understanding of the subject, then its presence is justified.

TABLE OF CONTENTS

TABLE OF CONTENTS (CON'T)

TABLE OF CONTENTS (CON'T)

LIST OF TABLES

LIST OF TABLES (CON'T)

Table | Page

LIST OF FIGURES

LIST OF FIGURES (CON'T)

ABSTRACT

One problem with the design of Tokamak fusion reactors is the presence of penetrations through which beams of neutral particles can be injected to heat the plasma. While the ducts allow the energetic particles to reach the plasma, they also provide an undesirable streaming pathway for the exit of fusion neutrons. These neutrons can have detrimental effects on the neutral beam injector internals, the superconducting toroidal magnetic field coils, and the reactor operating personnel. The limiting of this neutron streaming, without the introduction of excessive neutral beam particle or energy losses, is the subject of this thesis.

The author analyzed the behavior of the neutron fluxes which arise from three current methods of calculating neutral beam transport through the ducts: the Emittance Method, the Modified Emittance Method, and Geometrical Transport. To perform these analyses, the ANISN and DOT3.5 computer programs were utilized, with cross section data from the DLC-41/VITAMIN C library. The reactor model used in the analysis of each beam transport method is included in the text. These analyses indicate that the lowest total neutron flux received by the toroidal field coils of the reactor results from the beam path predicted with the Emittance Model.

The beam power losses were attributed to two mechanisms: particle "scrape off" or the collision of beam particles with the duct walls, and dissociative collisions between beam particles and excess gas from the injector neutralizer. The author developed an approximation to give particle scrape off losses, and found that these are nearly constant for ducts with side lengths greater than 10 cm. This left dissociative collisions as the predominant source of beam power losses. Using an approximation based on binary collision theory, the author demonstrated that the beam path described by the Emittance Method resulted in the least beam power loss due to dissociative collisions. This result, coupled with the neutron flux data, make the Emittance Method the preferred method for describing the neutral beam path.

The appendices contain copious background information, intended to clarify the text. Included are ANISN and DOT3.5 parameter sensitivity tests, TAPEMAKER input data, beam transport calculation methods, duct modeling techniques, and power calculations for Tokamak reactors and beam injectors.

CHAPTER ONE

Introduction

The development and utilization of controlled thermonuclear reactors for power production is one of the most challenging technological problems ever undertaken. One reason for this is that various, seemingly unrelated elements of the design of fusion reactors are, in fact, strongly coupled. This thesis is an attempt to analyze one such set of elements and to address their relative impacts on a given fusion reactor design.

The elements in question are the radiation load on the toroidal field coils which confine the plasma, and the efficiency of the neutral beam injectors which heat the plasma. The factors which join these two dissimilar quantities are the dimensions of the penetrations which provide the pathways for neutral beam injection into the plasma. As the penetration size is decreased to limit neutron streaming from the reactor, and hence, lower the flux to the coils; the efficiency of the neutral beam injectors can be hampered by increases in beam particle losses. Two of the mechanisms responsible for these losses are "scrape off", the collision of beam particles with the duct liner; and dissociative collisions between beam particles and deuterium gas molecules in the duct.

Current literature on the subject of fusion reactors does not address this interrelationship in detail. Indeed, judging from the differing penetration dimensions being dealt with by shielding analysts and injector designers, it would seem that the two groups are working toward two different results. The author has found only one recent paper[1] in which the radiological calculations were developed using data in agreement with neutral beam injector parameters. For this reason, the author used accepted analytical shielding techniques and developed beam power approximations to test the impacts of various beam transport calculation methods. The end result is a beam penetration which limits both neutron fluxes at the toroidal field coils and injector power losses.

CHAPTER TWO

Current Tokamak Fusion Reactor Designs

2.1. Design Basis

For the foreseeable future, one of the major areas of interest in efforts to develop a magnetically confined, controlled thermonuclear reactor will center on the Tokamak configuration. Current plans call for a Tokamak Fusion Test Reactor (TFTR) to become operational in 1980, at Princeton Plasma Physics Laboratory. This project will be followed by the Tokamak Experimental Power Reactor (TEPR) in about 1987, and the Tokamak Demonstration Power Reactor (TDPR) by 2000(2). Also proposed is TNS (The Next Step), a program to bridge the gap between TFTR and TEPR using the "Doublet" technology developed by General Atomic Company.(3)

Regardless of the stage of development or design selection, all Tokamaks share certain basic characteristics. First, they are toroidal in shape, with external magnets which force the plasma to follow the torus. They have external coils which provide ohmic heating through plasma compression. Lastly, they have some type of additional plasma heating system to augment ohmic heating, and raise the plasma to ignition temperature. In the TFTR, this is a beam of neutral deuterons.

Figure 2.1(4) shows an idealized Tokamak, and indicates the electric currents (I) and magnetic fields (B) present in a

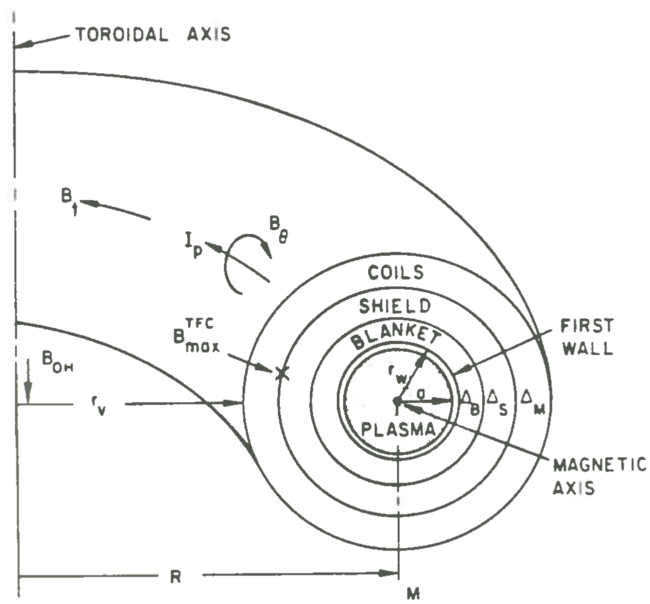

Figure 2.1. Idealized Tokamak configuration. (Nuclear Technology, 30, 3, Sept. 1976, page 264).

reactor of major (torus) radius R, and minor (plasma) radius a. The various components are as follows:

1) B_t is the magnetic field generated by the toroidal field coils (TFC) along the axis of the plasma. This field forces the plasma into a toroidal shape.

2) B_{OH} is the ohmic heating field, produced by the ohmic heating coils (OHC). Due to the direction of the field, a current (I_p) is set up along the plasma axis. This current, in turn, creates a poloidal field (B_θ) which encircles the plasma. By increasing B_{OH}, I_p is strengthened. This increases B_θ and compresses the plasma.

3) Equilibrium coils (EC) are also present around the reactor, and are used to produce a vertical field which stablilizes the plasma by reducing particle drift.

The above coils are shown on Figure 2.2[5].

An interesting result of this reliance on magnetic fields is that as reactor shielding increases, reactor power decreases. This follows from the fact that reactor power is given by:

$$P \propto (B_{max}^{TFC})^4 \left(1 - \frac{r_w + \Delta_B + \Delta_s}{R}\right)^4 , \qquad (2.1)$$

where

B_{max}^{TFC} = maximum field strength of TFC,

r_w = radius to the first wall of the reactor,

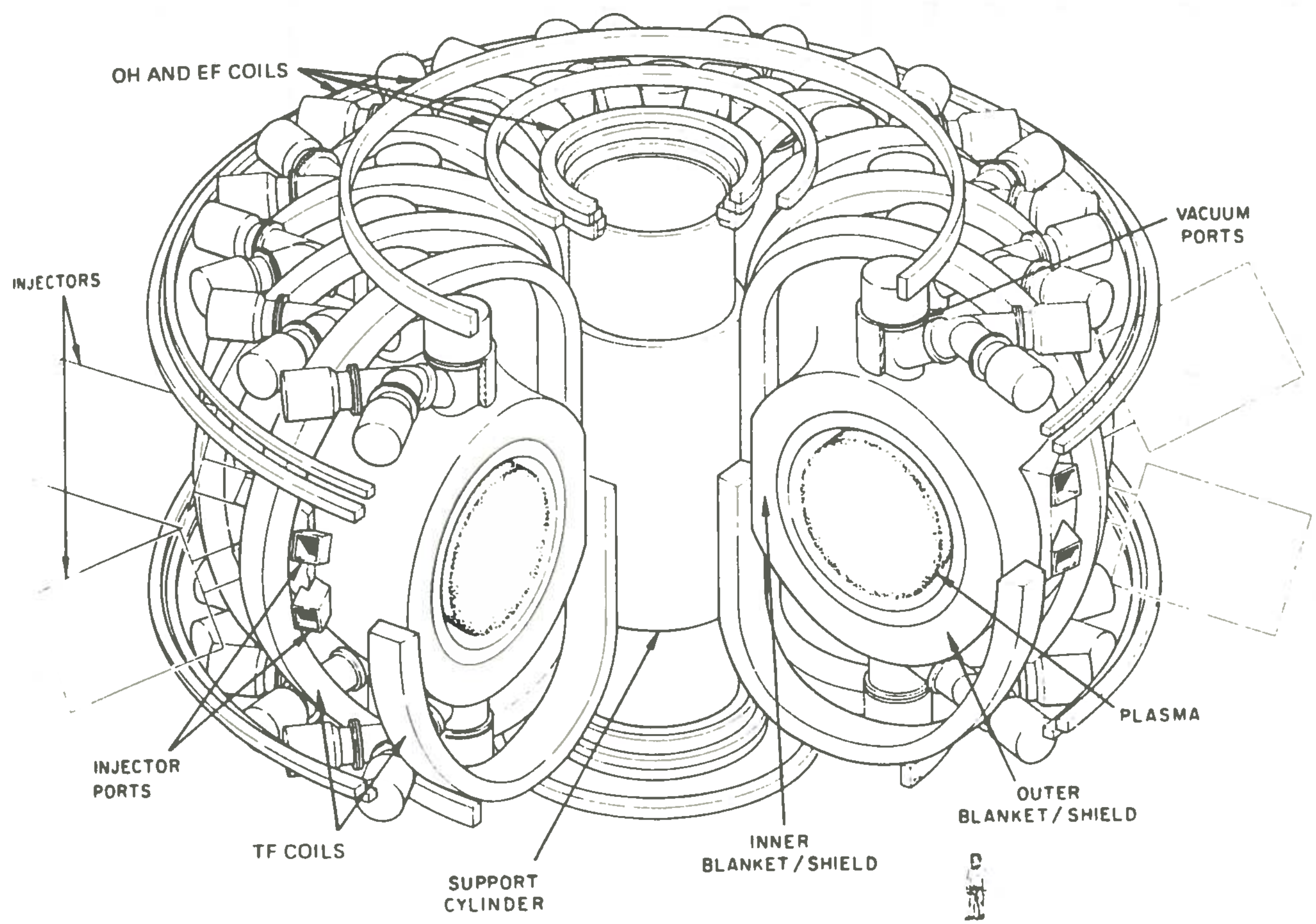

Figure 2.2. TEPR perspective view. (Nuclear Technology, 30, 3 Sept. 1976, page 271).

Δ_B = blanket thickness,

Δ_s = shield thickness.

A derivation of this relation is given in Appendix A.

2.2. Blanket/Shield Structure

As shown in Figure 2.2, the plasma is surrounded by a structure known as the blanket/shield. As the name implies, its purpose is two-fold. First is a blanket region of special materials which is separated from the plasma by only a narrow vacuum region and the thin first wall of the plasma chamber. The blanket materials are chosen to fulfill certain functions. For instance, if the reactor is to breed tritium for use as fuel in the D-T reaction, then layers of some lithium compound such as lithium oxide will be included in the blanket[(6)]. Should heat removal for thermal power production be required, then the blanket will contain coolant channels. The other function of the blanket/shield is to shield the external reactor equipment and operating personnel from the neutron and gamma fluxes generated during reactor operations.

As shown above, reactor power is dependent on the thickness of three items; the first wall, the blanket, and the shield. To obtain maximum reactor output, each of these layers must be of minimum allowable thickness. The first wall in most designs is an ablative layer which is thick enough to be structurally sound and able to withstand several years of deterioration due to sputtering. Likewise, the blanket must be of such composition and thickness as to achieve its purposes of breeding and heat removal. And while both these regions can be optimized or subject to variations such as choice of material, coolant selection or flow rate, etc.; there are limitations to the amount of material which can be deleted. This leaves the shield as a good candidate for variation to optimize power generation. However, the shield must be of sufficient thickness to reduce dosages to the TFC and other reactor externals to levels which are tolerable.

In light of this, the ideal shielding configuration for the reactor would be one which is uniform and unbroken. In actual practice, however, the blanket/shield region is penetrated by numerous ducts and openings as follows:

1) maintenance and access ports,
2) diagnostic channels,
3) divertor ports for plasma purity control,
4) vacuum pumping ports,
5) coolant channels, and
6) supplementary plasma heating ducts.

Of these, the first four categories may be neglected, since they are openings which either can be plugged during reactor operations (#1, 3, & 4), or can be run in labyrinthine patterns to inhibit streaming (#2). Though coolant channels will be small and numerous, it may be possible to run them in some circuitous manner to avoid streaming. This leaves the ducts used for plasma heating as the main source of radiation streaming pathways through the shield region. Therefore, any comprehensive attempt to minimize shield thickness as a means of increasing reactor power must consider the effect of heating penetrations.

2.3. Neutral Beam Injection System

Referring again to Figure 2.2, the reader will note the neutral beam injection system as consisting of pairs of injectors, enclosed in box-like structures, and connected to the reactor by square ducts. The boxes surrounding the injectors are vacuum chambers. The ducts are beam penetrations which pass through the blanket, shield, and first wall of the reactor.

As mentioned previously, the purpose of this reactor system is to inject a beam of energetic particles directly into the plasma at an angle which will assure that the particle energy is fully expended in heating the plasma. To minimize the energy loss of the particle beam and insure its proper penetration into the plasma, neutral deuterons have been chosen as the heating particles in TFTR(7) and other fusion projects.(8, 9)

The design of neutral beam injectors for fusion machines is an on-going effort, with the designs being tailored to meet the particular needs of the reactors under consideration. However, current design trends can be seen in the following schematics of two injectors. Figure 2.3a)(10) is the type of injector to be used in the TFTR facility at Princeton, while Figure 2.3b)(11) illustrates an injector for TNS. The units are similar in layout, however, the

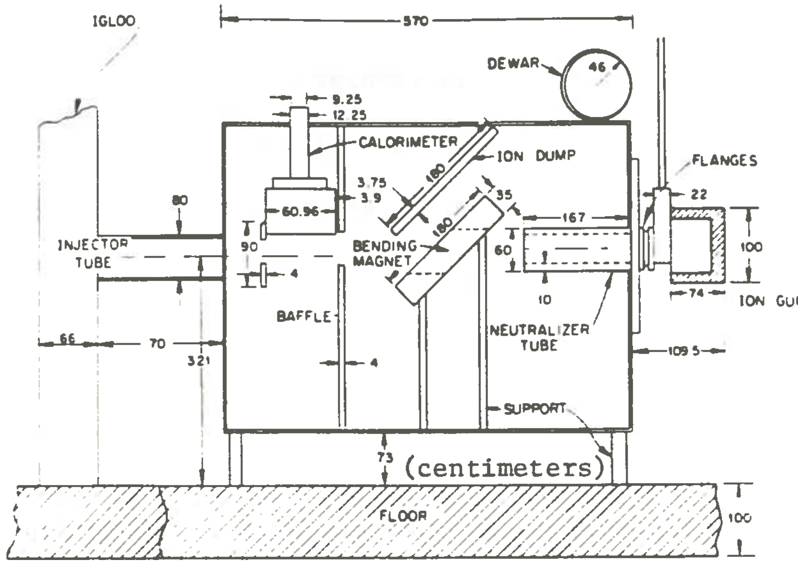

(a)

(ORNL-TM-6354 (1978), page 7)

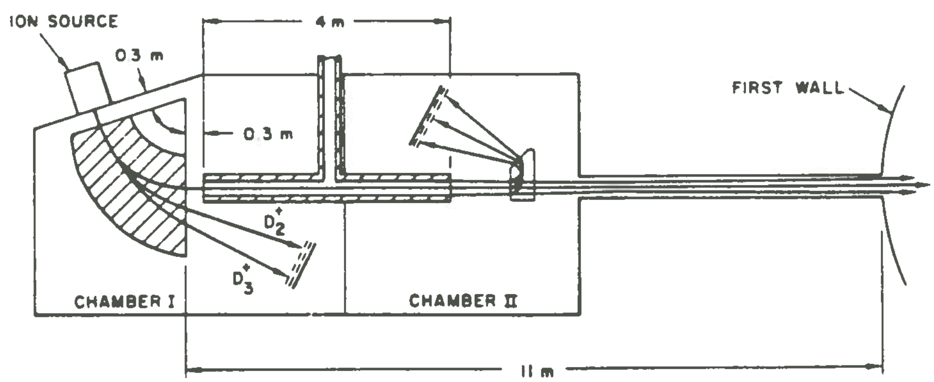

(b)

(<u>TNS Scoping Studies</u>, Vol. V (1978), page 5.5-23)

Note: Drawings are not to scale

Figure 2.3. Schematics of neutral beam injectors for (a) the Tokamak Fusion Test Reactor and (b) the Next Step Reactor.

TNS injector is designed to recover energy direct conversion from D^+, D_2^+, and D_3^+ ions removed from the D^o beam. This will be accomplished by dual bending magnets. Apparently, the TFTR injector will perform the same function with one magnet.

In detail, the TNS injector works in the following manner. The ion source consists of a multiaperture grid and an accelerator to produce and energize a beam of D^+, D_2^+, and D_3^+ ions. The beam is then sent through a bending magnet which splits the beam into components of various masses. Only the D^+ component leaves the magnet in such an alignment as to enter the neutralizer section of the device. Both the D_2^+ and D_3^+ components are diverted to a direct converter beam dump.

The neutralizer portion of the injector is a chamber through which the D^+ beam travels, and into which a stream of deuterium gas is also fed. Through interactions with the D_2 molecules, some D^+ ions are neutralized and become D^o atoms. Thus the beam leaving the neutralizer consists of both D^+ ions and D^o atoms, and is ready for the final phase of beam preparation. This occurs when the beam passes through a second bending magnet which removes the D^+ ions. These are diverted to a second direct conversion beam dump. As a result, a beam of neutral deuterons exits the injector and enters the beam duct; a channel which not only admits the deuterons to the plasma, but also allows fusion neutrons to bypass the reactor shielding.

Further information on the neutral beam injector system is included in Appendix A. It consists of the injector power flows as proposed by Stacey, et al.[12]

CHAPTER THREE

Shielding Analysis

3.1. General Considerations

The shielding analysis problem in question consists of a long, narrow, square or rectangular duct extending from the vacuum region surrounding the toroidal plasma, through a blanket/shield composed of layers of various materials. The duct enters the reactor at an angle tangent to the torus,[13] and passes between gaps in the toroidal field coils.

A description such as this tends to direct the shielding analyst toward any calculation method capable of approximating three-dimensional solutions. Techniques of interest at this time are the Monte Carlo codes, such as VIM[14, 15] and MORSE[16]; and multi-dimensional, discrete ordinate programs, such as DOT3.5. The capability of the discrete ordinate method to duplicate Monte Carlo results was of particular interest to the author. For this reason, a good deal of this chapter will be devoted to the comparison of fluxes calculated by others using Monte Carlo program versus flux calculations obtained by the author using ANISN and DOT3.5.

These two programs are very similar, in that they both approximate the Boltzmann transport equation using discrete ordinates. In addition, they treat anisotropic scattering by the use of Legendre polynomials.[17, 18] The problem to be solved with one of the codes is modeled in terms of spatial mesh intervals.

Since ANISN is one-dimensional, this means that the model will consist of i intervals in the R, X, Y, or Z direction. Likewise, a two-dimensional DOT3.5 model is made up of ixj mesh spaces in the X-Y, R-Z, or R-θ planes.

Naturally, the addition of a second dimension renders a DOT3.5 problem more difficult to model, and also makes it more time-consuming to run on a computer. The situation is further complicated by the fact that the solution method employed can exhibit strong dependence on some input parameters. These factors suggest that a problem to be run using DOT3.5 should first be run on some limited scope with ANISN. This allows the programmer to determine the magnitude of various parametric impacts on both the speed and accuracy of the solution. In addition, the programmer is able to test the validity of his modeling methods. It is especially advisable to attempt preparatory ANISN runs if "bench mark" calculations are available which can be correlated to both ANISN and DOT3.5 runs.

The above line of reasoning led the author to search the available literature for just such a set of bench mark results. The search was not in vain. A pair of curves was found which were applicable to both ANISN and DOT3.5 neutron flux calculations for a neutral beam injector duct. The curves were generated by Abdou and Jung, at Argonne National Laboratory (ANL), and are shown in Figure 3.1.[19]

Curve 3.1a) represents the total neutron flux from the first wall of the reactor to the exterior of the blanket/shield

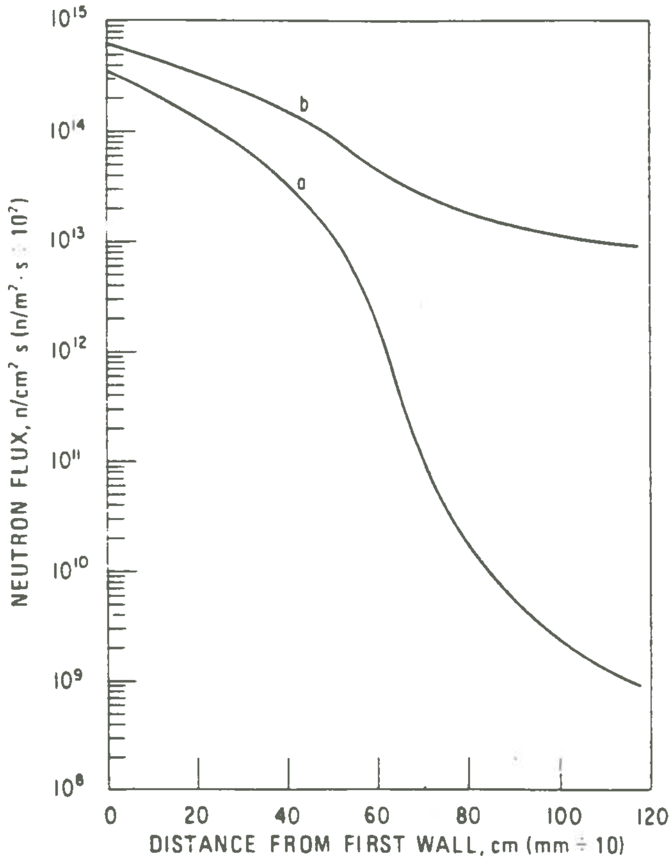

Figure 3.1. Total neutron flux (normalized to a neutron wall loading of 1 Mw/m^2) as a function of depth within the blanket and bulk shield at two locations: (a) a radial line far removed from penetration effects and (b) a surface parallel to the walls of the neutral beam duct and 5 cm away. (Nuclear Technology, 35, Mid-August 1977, page 73).

region, along a radial line an infinite distance from the duct. This negates the effects of the penetration, and also renders the problem soluble by the use of a one-dimensional, line-of-sight calculation. This means that the results can be duplicated with ANISN as well as DOT3.5. The b) curve is for a radial line 5 cm from the duct liner. This introduces penetration effects, and renders the problem insoluble to one-dimensional techniques. Taken as whole, this data provides a method of confirmation of both the ANISN and DOT3.5 codes which are available at LSU.

3.2. Program Testing Concepts

Once data were located which could determine program accuracy, the next step was to develop an adequate model of the problem and run a sample case for comparison using DOT3.5. This was not, however, a straightforward task. Questions remained regarding the selection of appropriate neutron cross section data, modeling parameters such as the number of mesh intervals, and the impact of various other parameters on the accuracy of the DOT3.5 solution method. As a result, a simple problem was attempted using ANISN to determine the impact of the above input data on the program output. This information would be used to model the ANL problem in an ANISN run for comparison to Figure 3.1a). Only after the technique and the model were fully developed would a DOT3.5 run to attempted for correlation with Figure 3.1b).

Once again, data were available with which to test ANISN. This time, however, the information was found in the literature of the Japanese Atomic Energy Research Institute (JAERI). Figure 3.2[20] illustrates neutron fluxes from the first wall through the blanket/shield of the JAERI Tokamak for three conditions: total flux, flux for neutrons with energy greater than 0.1 MeV, and the flux for 14.1 MeV neutrons. The reader will note that results for both ANISN and TWOTRAN-GG (a two-dimensional code similar to DOT3.5) are shown on the graph.

As mentioned above, the JAERI problem definition satisfied the requirements of a simple problem with which to test ANISN. This problem is much more basic than the ANL problem. Table 3.1 is included to show a comparison between the ANL parameters, as developed by the author, and the JAERI information as presented in Figure 3.2.

3.3. ANISN Evaluations

3.3.1. JAERI Problem

Initially, it was intended to directly correlate ANISN output with the JAERI results. For this reason, the model derived was intended to bear as close a resemblance as possible to the JAERI model (see Figure 3.3). However, it proved necessary for the author to make several assumptions based on other information sources:

1) The plasma region is composed of either hydrogen or a deuterium-tritium mixture, depending on cross section data available, and has a density of 1.0 x 10^{-10} ions-barn^{-1}-cm^{-1} [21].

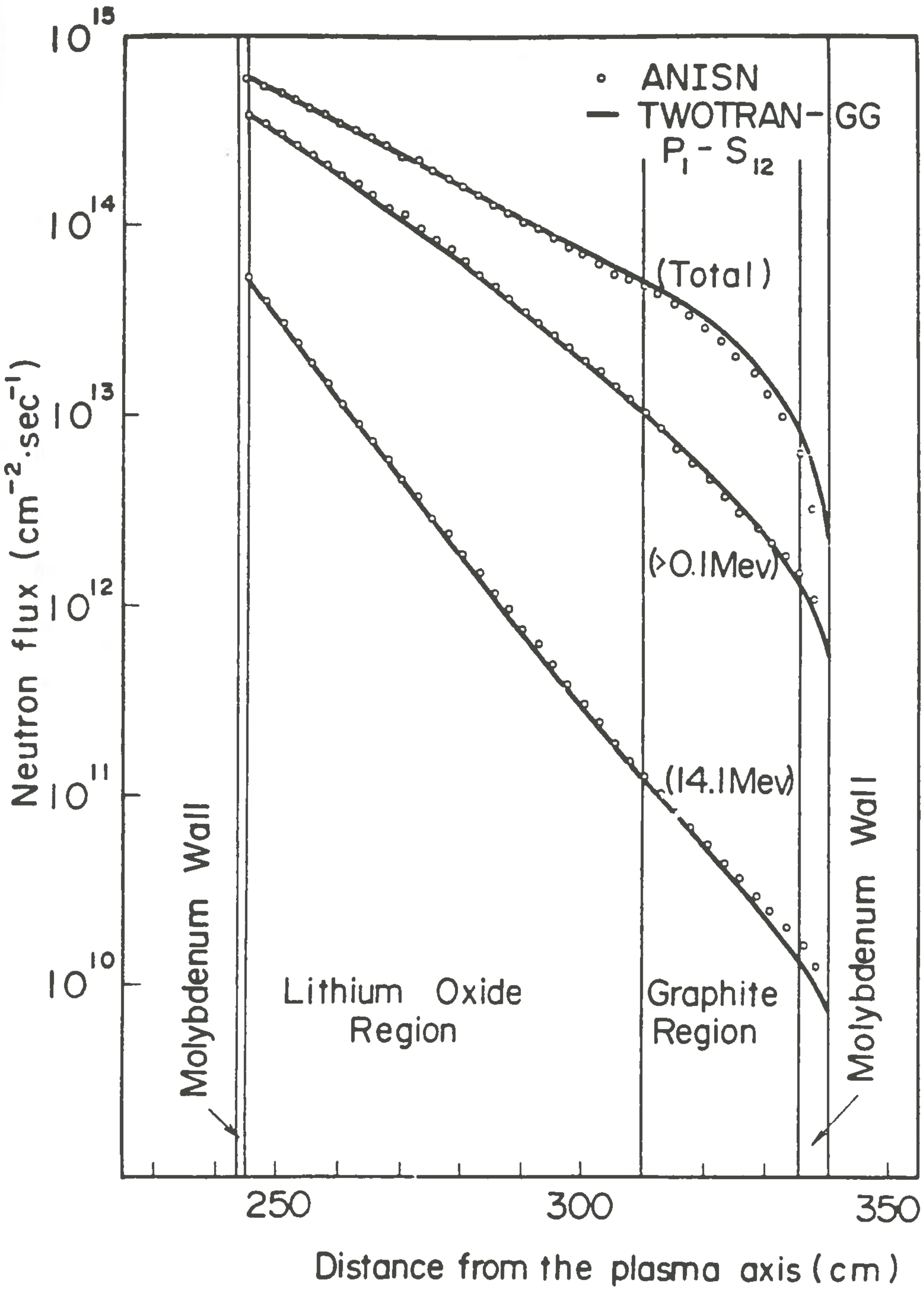

Figure 3.2. Comparison of neutron fluxes calculated by ANISN and TWOTRAN-GG. (JAERI-M6475 (1976), pg. 10).

Table 3.1

Comparison of Parameters Derived for ANISN Calculations of ANL and JAERI Tokamak Models

	ANL	JAERI
Number of Intervals	149	58
Number of Zones	38	6
Number of Materials	114	15
Order of Scatter	2	1
Order of Angular Quadrature	10	12

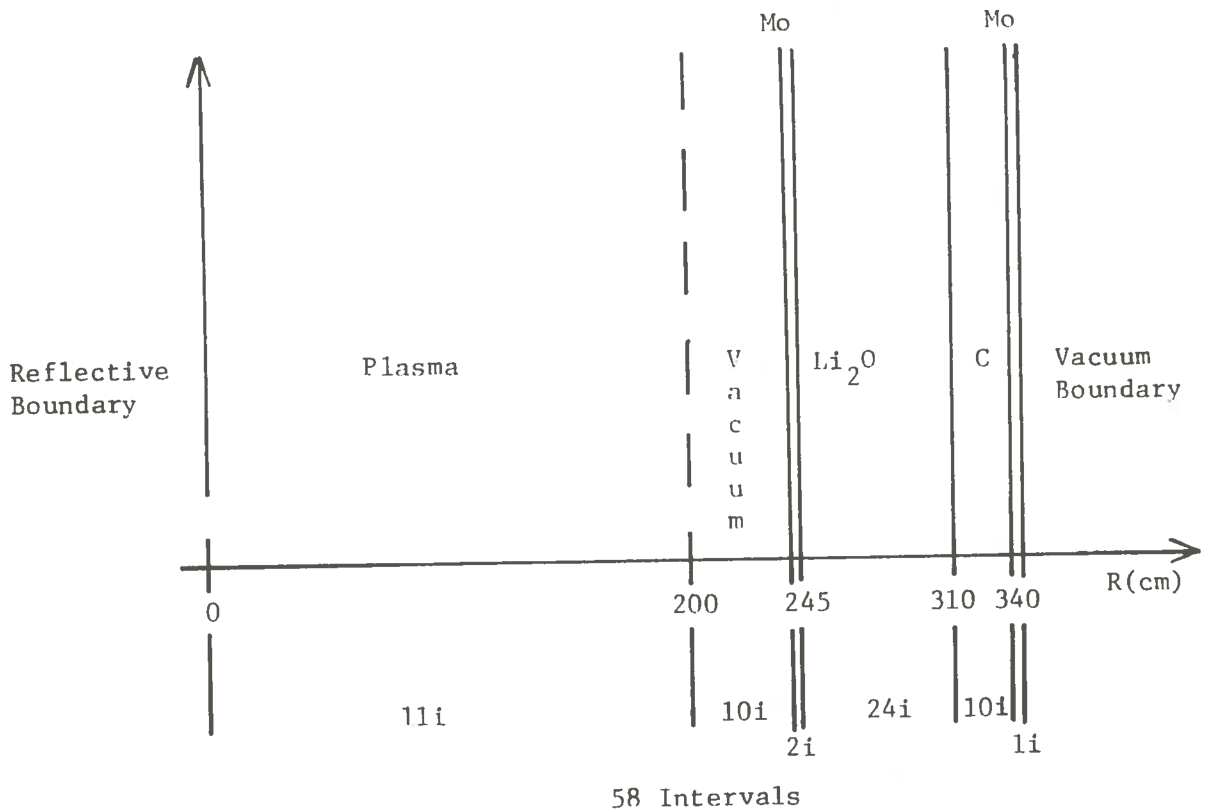

Figure 3.3. Model developed for ANISN neutron flux calculations in the blanket/shield region of the JAERI Tokamak.

2) The vacuum region is to be treated as a region of sputtered atoms of first wall material (molybdenum) with a density of 5.0×10^{-13} atoms-barn^{-1}-cm^{-1}. This is due to a sputtering rate of 5.0×10^{-3} atoms-ion^{-1} (22).

3) The lithium oxide region contains natural lithium (7.5% Li^6 and 92.5% Li^7).

The ANISN parametric studies of cross section libraries, source term definition, orders of scatter and angular quadrature, mesh interval number, and various other inputs are included for reference purposes in Appendix B. The net result of the sensitivity tests indicated that a good method of modeling and solving the JAERI problem as a test of ANISN would be to run a P_2-S_{10} calculation using 58 intervals. The plasma was modeled as a distributed source, composed of 50% deuterium and 50% tritium. Cross section data were obtained from the 56 group DLC-41/VITAMIN C library (see Appendix C). The model used a reflective left boundary with a vacuum right boundary, and represented the endless toroidal geometry as a cylinder 1×10^6 cm long. Unfortunately, this model did not give satisfactory results for comparison with the JAERI fluxes. Figure 3.4 shows a plot of the ANISN output versus the JAERI curves for total flux and 14.1 MeV flux.

As will be seen later, the author was able to obtain fairly good agreement between his ANISN runs and the ANL fluxes illustrated in Figure 3.1. Since the model and techniques used to analyze the ANL problem were a direct result of what was learned

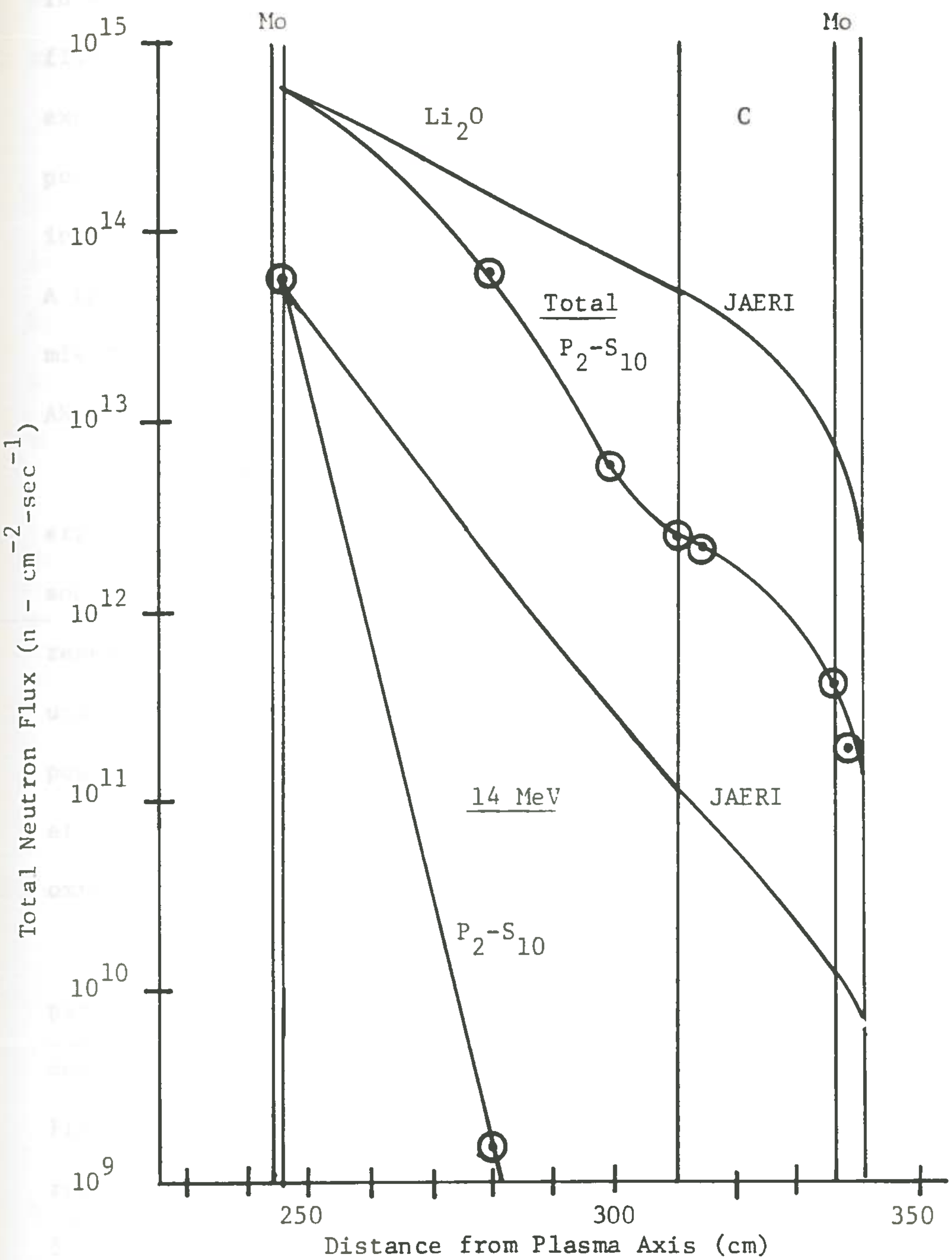

Figure 3.4. Comparison of neutron fluxes obtained from ANISN (P_2-S_{10}) vs. fluxes from JAERI calculations.

in solving the JAERI problem, then the lack of corresponding flux curves in Figure 3.4 was very disturbing. Several possible explanations were considered and explored. First, the possibility of error existed in the modeling used by the author, in his preparation of data, and his interpretation of results. A thorough check of the problem did not indicate any such mistakes. Furthermore, as mentioned above, good agreement with ANL was obtained with similar methods.

Another possibility was that the JAERI fluxes were in error. Admittedly, this reasoning was not easy to accept, however, some justification for this was provided. It was learned that researchers at Oak Ridge National Laboratory (ORNL) had been unable to duplicate some of the JAERI results.[23] In fact, a possible source of error was indicated in the author's early efforts. While using incorrect cross section data for the lithium oxide blanket, good agreement with JAERI was obtained.

A third possibility is suggested which exonerates both parties. Comparison of the pair of total flux curves in Figure 3.4 demonstrates some similarity to the pair of total flux curves in Figure 3.1. It will be recalled that the latter curves were representations of flux at two different distances from the duct, 5 cm and infinity. Perhaps, through manipulation of the source term inputs, the JAERI researchers were able to simulate, in ANISN, the effects of a duct near the location of interest. In contrast, the author's data was for a location an infinite distance from the penetration, hence the discrepancy in the curves. This is speculation on the author's part.

3.3.2. ANL Problem

On completion of the JAERI studies, efforts were concentrated on obtaining a suitable model of the TFTR as presented by ANL. It was decided to use the same solution method as that set forth above for the JAERI problem. The only difference between the two problems was one of size, as can be seen in Table 3.2.

The material compositions and thicknesses of the regions were, for the most part, obtained from ANL literature.(24) However, certain assumptions, some identical to those used previously, were also included as follows:

1) The plasma is 50% deuterium and 50% tritium, with density equal to 1.0×10^{-10} ions-barn^{-1}-cm^{-1}.
2) The vacuum regions consist of sputtered atoms of first wall material (316-stainless steel) with density of 5.0×10^{-13} atoms-barn^{-2}-cm^{-1}.
3) The cryogenic tubing around the TFC is 316-SS.
4) TFC insulation is alumina (Al_2O_3) and epoxy ($C_{10}H_{30}O_2$).

These materials were used to prepare a group-independent-tape from DLC-41/VITAMIN C, using the TAPEMAKER program.(25)

The results of the 149 interval, 56 group, P_2-S_{10} calculation were normalized to the total flux at the first wall of the reactor, 3.5×10^{14} neutrons-cm^{-2}-sec^{-1}. Figure 3.5 provides

Table 3.2

Reactor Modeling Information for ANL Tokamak*

Region	Radius (cm)	Thickness (cm)	Intervals per Region	Material
1	210	210	4	D-T
2	240	30	2	Vacuum
3	241	1	1	SS
4	242	1	1	SS + H_2O
5	272	30	15	SS
6	273	1	1	Vacuum
7	276	3	2	SS
8	291	15	10	C + 1% B
9	296	5	5	SS
10	361	65	26	Pb Mortar
11	370	9	6	Al
12	436.3	66.3	2	Vacuum
13	439.8	3.5	2	Al
14	440.8	1	1	Vacuum
15	441.05	0.25	1	SS
16	441.55	0.5	1	Liquid N_2
17	441.8	0.25	1	SS
18	442.05	0.25	1	Epoxy
19	442.3	0.25	1	Al_2O_3
20	447.3	5	2	Al
21	448.3	1	1	Vacuum
22	449.05	0.75	1	Epoxy
23	449.8	0.75	1	Al_2O_3
24	451	1.2	2	SS
25	521.5	70.5	40	TFC
26	529.8	8.3	5	He Bath
27	531	1.2	2	SS
28	531.75	0.75	1	Al_2O_3
29	532.5	0.75	1	Epoxy
30	533.5	1.0	1	Vacuum
31	538.5	5.0	2	Al
32	538.75	0.25	1	Al_2O_3
33	539	0.25	1	Epoxy
34	539.25	0.25	1	SS
35	539.75	0.5	1	Liquid N_2
36	540	0.25	1	SS
37	541	1.0	1	Vacuum
38	544.5	3.5	1	Al
			149	

* Adapted from <u>Nuclear Technology</u>, 35, Mid-August (1977), pages 57 and 58.

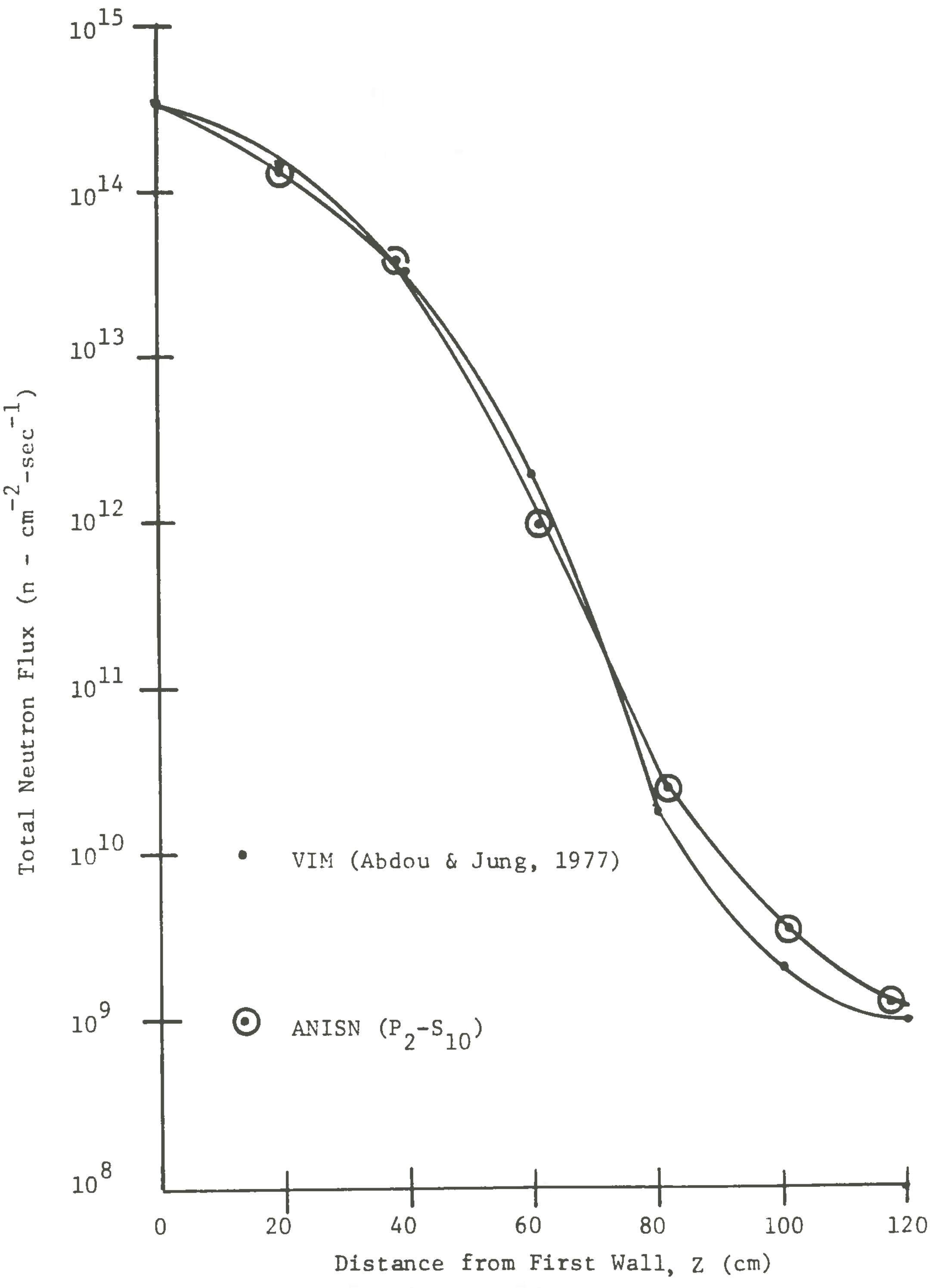

Figure 3.5. Comparison of ANISN results with no duct present vs. VIM fluxes for a radial line an infinite distance from the duct.

a comparison between the ANISN output and curve a) in Figure 3.1. The ANISN fluxes vary from -67% to +43% with respect to the VIM calculated fluxes generated by ANL. This indicates that a one-dimensional, discrete-ordinate code can, under the proper circumstances, yield results which compare favorably with more sophisticated, multi-dimensional, Monte Carlo routines.

3.4. DOT3.5 Evaluations

One purpose of the previous sections and Appendix B, was to illustrate the need for a proper understanding, by the shielding analyst, of the various criteria which must be addressed to properly use the ANISN program. In the process, a one-dimensional model of the TFTR was developed and found to be a reasonably accurate representation of the machine. Also, this learning exercise indicated many areas of potential error which a programmer might experience. This building process brought the author to a point at which an accurate two-dimensional model of the TFTR could be developed and tested with DOT3.5, the standard of comparison being Figure 3.1b).

Figure 3.6 shows the model of a neutral beam injector duct used in most of the ANL calculations.[26, 27] It can be seen that the duct enters the plasma at some angle, θ_b, with respect to a line perpendicular to the plasma centerline. This arrangement seriously complicates the modeling of the penetration by the use of a two-dimensional mesh. The accurate representation of a duct for any θ_b not equal to zero requires a very fine grid, and hence,

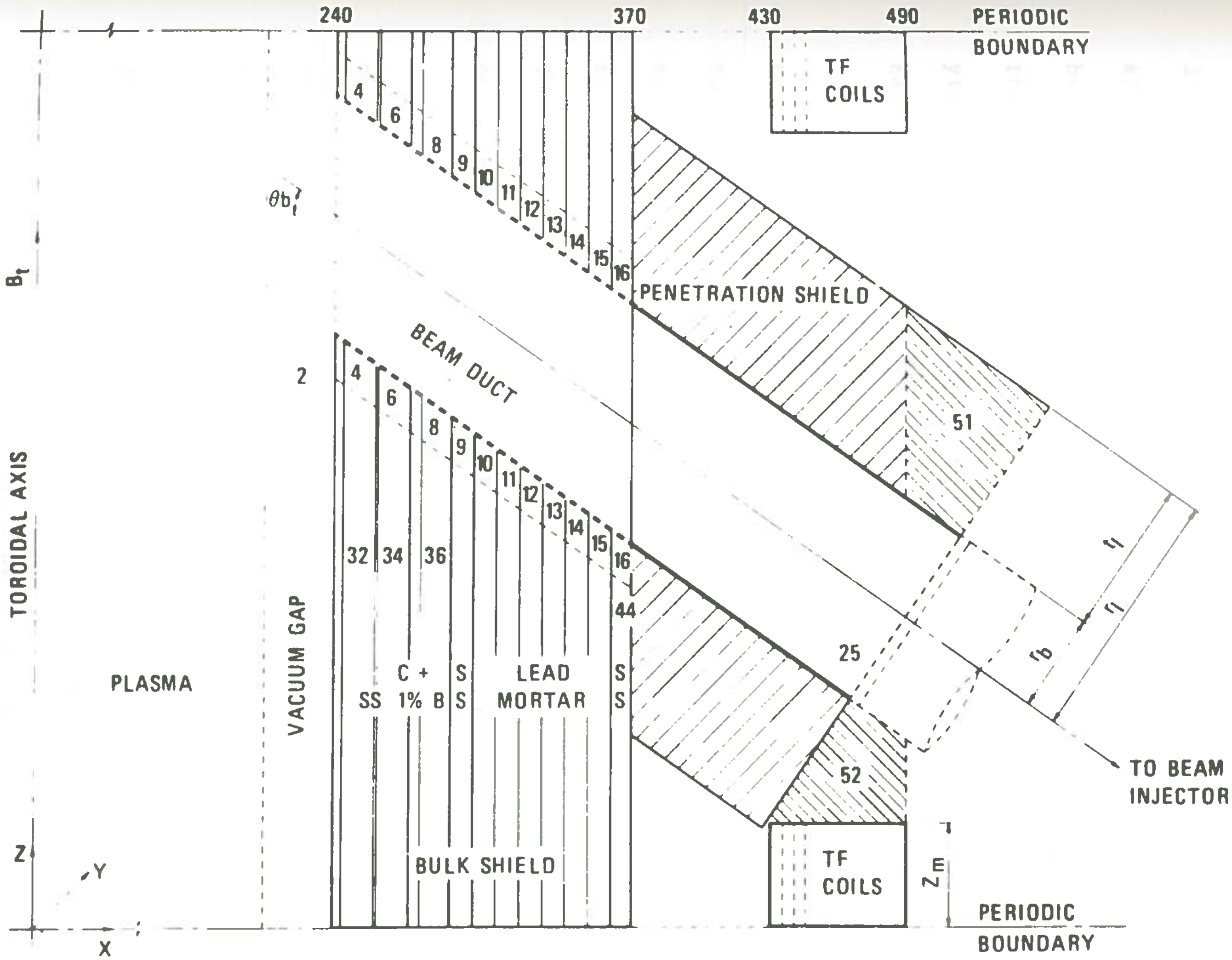

Figure 3.6. Schematic of geometry representation for analysis of neutral beam penetrations and their shield. (Nuclear Technology, 35, Mid-August 1977, page 70).

a large number of intervals in the R and Z directions. This tends to make both the modeling and the solution extremely time-consuming. Fortunately, it has been found[28] that for $0° \leq \theta_b \leq 35°$, the flux variations are small and within the range of statistical uncertainty inherent in the VIM calculations performed by the ANL research group. Therefore, for the DOT3.5 problem, the angle of incidence of the duct was assumed to be zero. This yielded the duct model shown in Figure 3.7, with the plasma centerline (R-axis) perpendicular to the duct centerline (Z-axis).

It was decided to use this R-Z geometry configuration so that the beam duct would appear as a right circular cylinder surrounded by disks of varying composition, and resting on a disk source. The thicknesses of the disks, and the intervals defining them are identical to the region data supplied in Table 3.2. Therefore, there are 149 intervals in the Z-direction. This far outweighs the number of intervals in the R-direction, since only 35 intervals are used. These intervals include boundaries of material variation, and also interval #4. This particular point was specified to yield output for a line 5 cm from the duct, which can be used to correlate the DOT3.5 fluxes to the curve 3.1b).

Since the model represents only one-fourth of a reactor section, then the boundary conditions on each side must be reflective. Similarly, only a portion of the plasma is shown, so the bottom boundary must also be reflective. The top boundary is one through which no particles enter, and the region beyond it

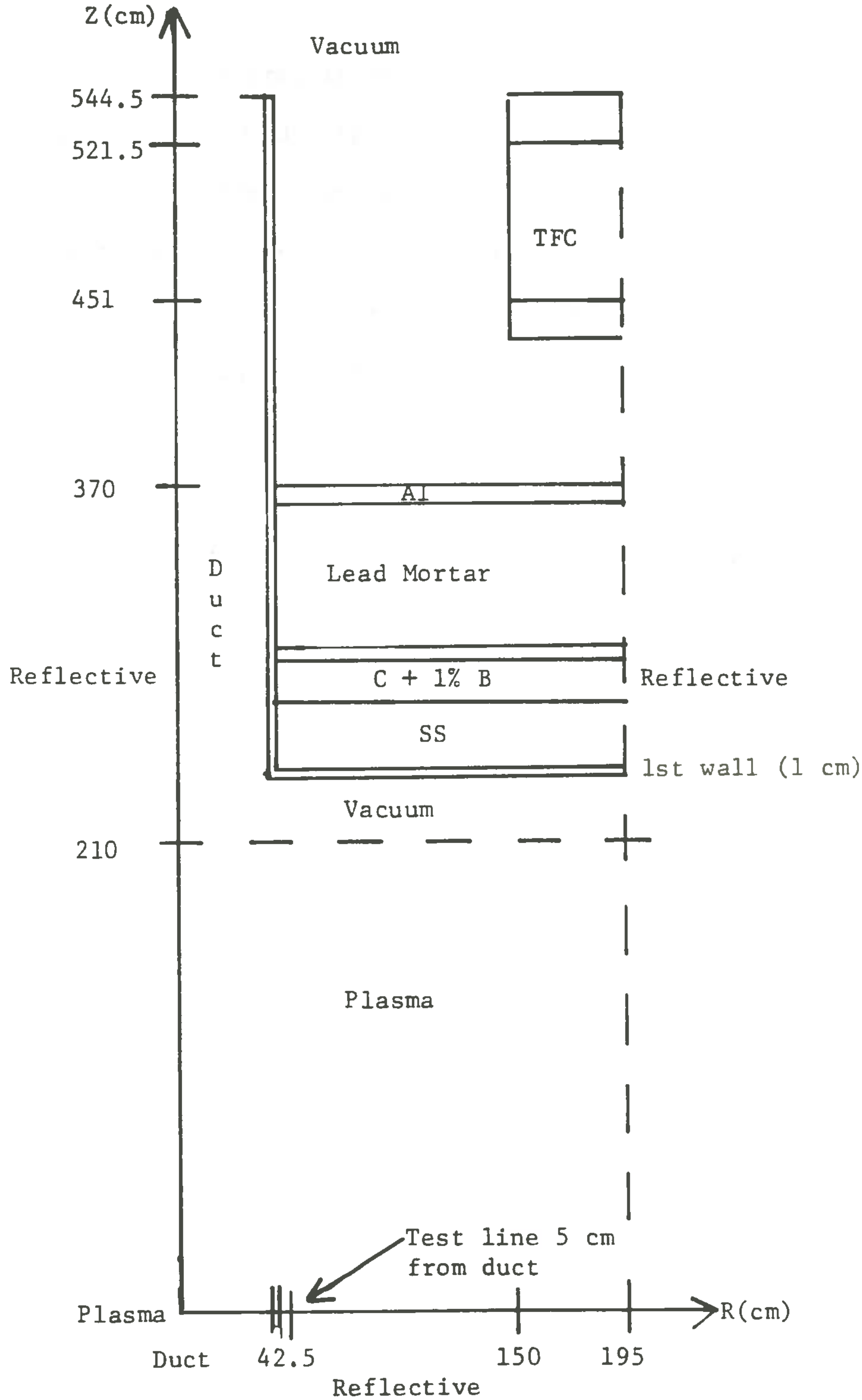

Figure 3.7. DOT3.5 model of the ANL beam duct in R-Z geometry.

is of no interest; therefore, it is treated as a vacuum boundary. Additional data for the DOT3.5 test run, and information regarding parametric analyses are included in Appendix D. Of special interest are the variations caused by the computational[29] and iterative[30] methods as described in the DOT3.5 manual.

Figure 3.8 provides a comparison between the total fluxes from DOT3.5 and the ANL run for points 5 cm from the duct. It should be recalled that the ANL fluxes were obtained using the VIM Monte Carlo routine. The DOT3.5 fluxes were normalized to 6.0×10^{14} neutrons-cm^{-2}-sec^{-1} at the first wall of the reactor, yielding variations of from -36% to +75% with respect to VIM.

Figure 3.9 demonstrates the impact of duct diameter on total neutron flux for a surface parallel to the duct axis and 5 cm from that axis. It is readily apparent that increasing the size of the duct will increase the total flux. This effect can be seen in the figure. What may not be apparent in Figure 3.9 is that the change in flux with respect to duct diameter is asymmetrical. The lack of symmetry is distinct in Figure 3.10. This drawing plots the total flux along the axis of the duct versus the distance from the first wall outward to the top boundary of the model. As in Figure 3.9, the duct diameters used in Figure 3.10 range from 21.25 cm to 170 cm, and double in each case. The total fluxes for the points indicated on these curves were then used to check the relationship between duct cross sectional area and total flux. The results are shown in Table 3.3. From this table, it can be seen that the change in duct area is a constant 300% from case to

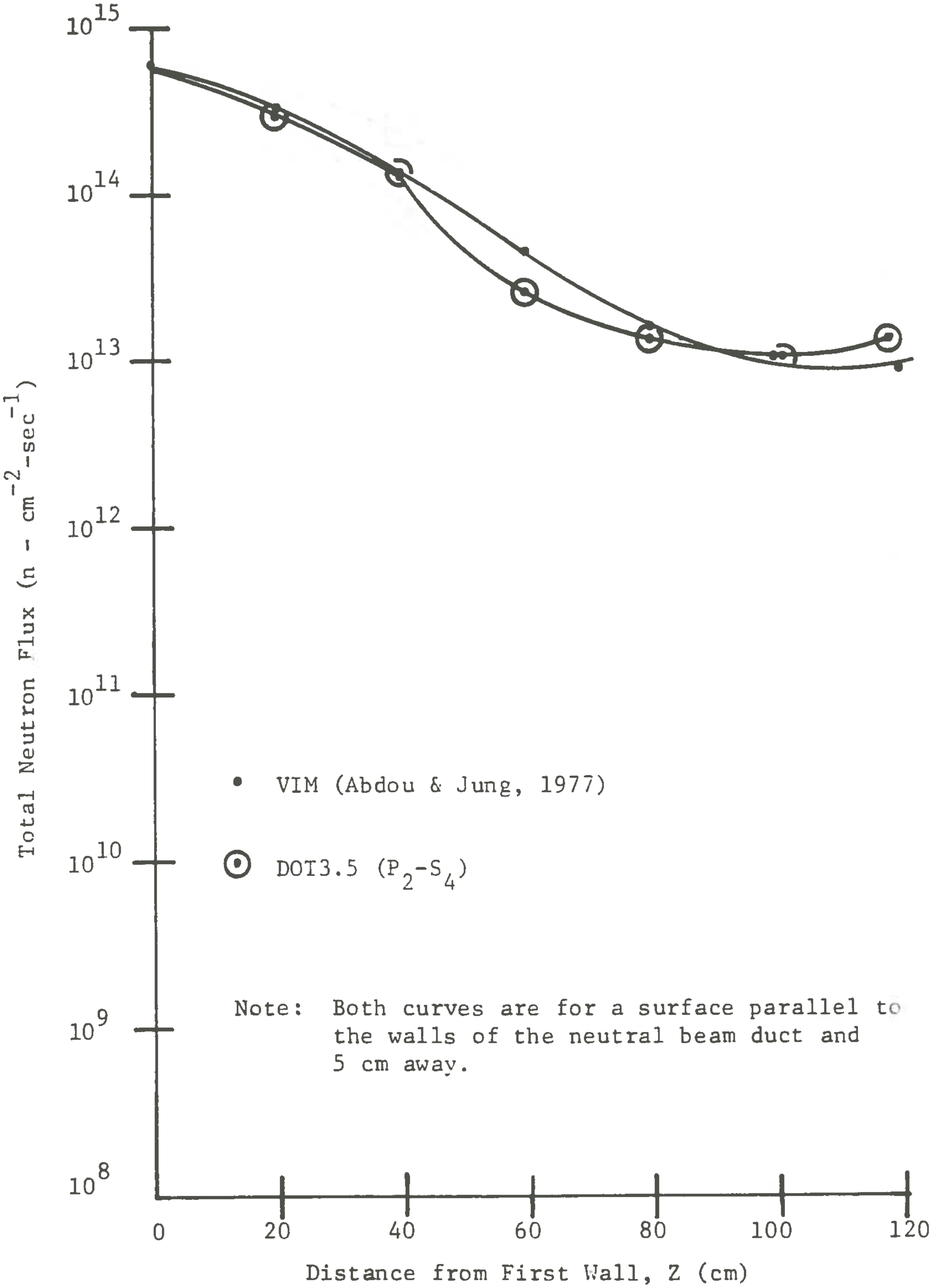

Figure 3.8. Comparison of DOT3.5 results vs. VIM fluxes for the ANL Tokamak.

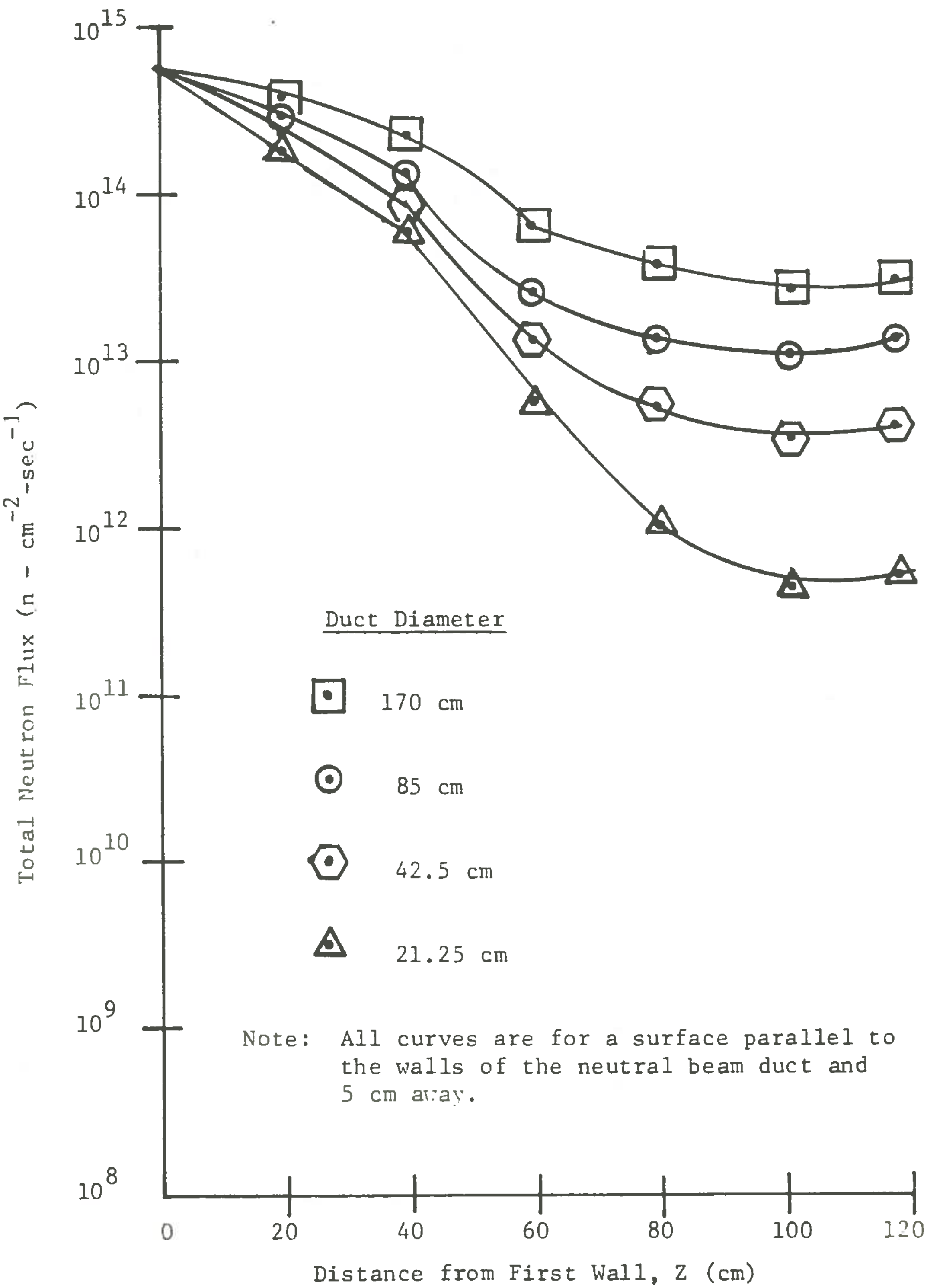

Figure 3.9. Effect of duct diameter on the DOT3.5 total neutron fluxes.

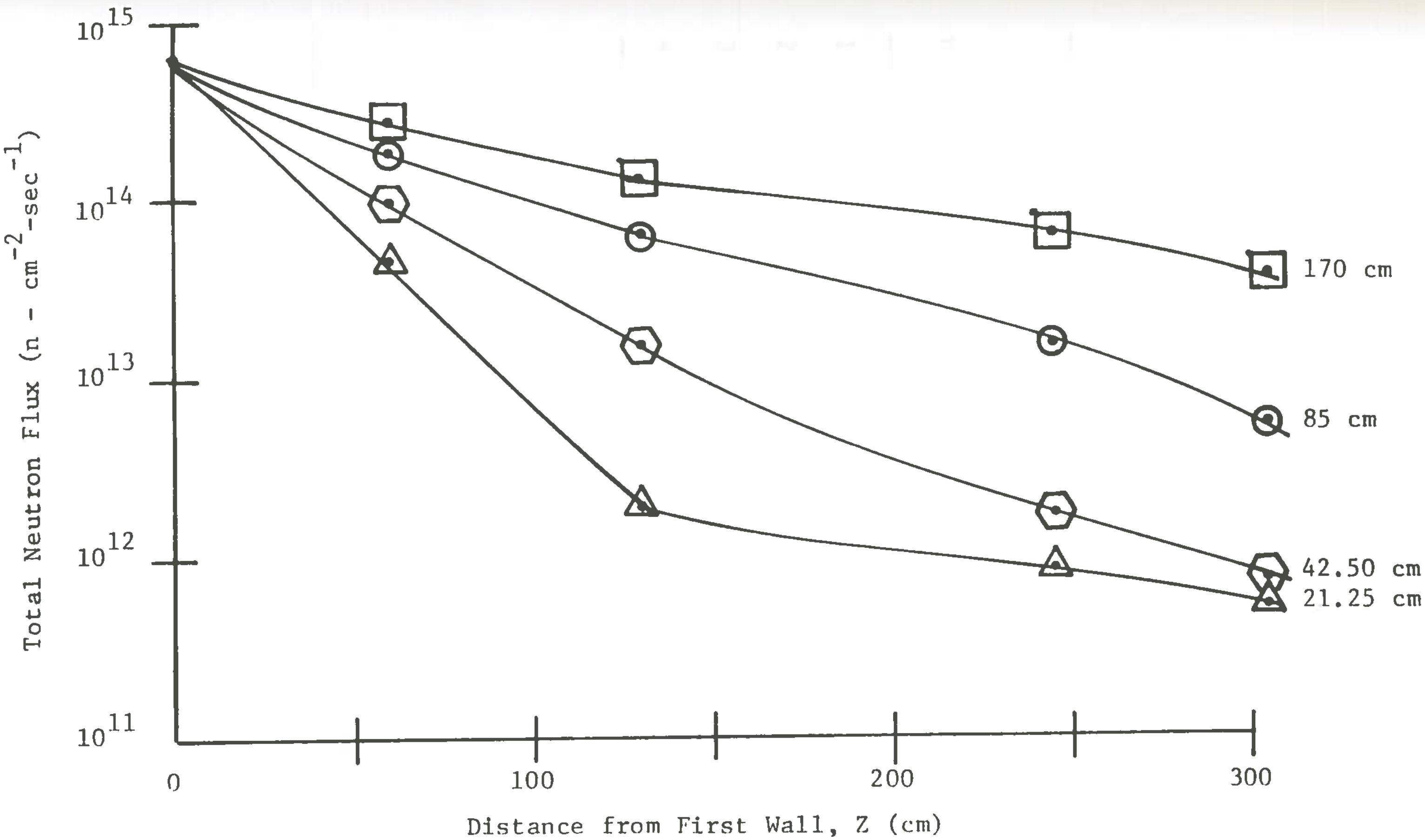

Figure 3.10. Total flux vs. distance from first wall, calculated along the duct axis for various duct diameters.

Table 3.3

Effect of Duct Area Variations on Total Flux
at Selected Distances from the First Wall

			$\frac{\phi_n - \phi_{n-1}}{\phi_{n-1}}\%$			
n	d_n (cm)	$\frac{A_n - A_{n-1}}{A_{n-1}}\%$	60 cm	130 cm	246 cm	304.5 cm
1	21.25	--	--	--	--	--
2	42.50	300	132	720	99	37.5
3	85.00	300	70	311	769	674
4	170.00	300	52	105	557	557

case. However, no such change is seen for any total flux comparisons, regardless of duct size or distance from the first wall. Clearly, various mechanisms such as multiple reflections and absorption by liner materials must be at work within the ducts to yield such anomalous results.

3.5. Duct Representation Techniques

Once an accurate model of the reactor had been obtained for two-dimensional geometry, the next step was to develop a technique which would allow a reasonably good representation of the duct. Due to modeling limitations, DOT3.5 was solved for a cylindrical duct, however, this is not a precise image of the penetration. Contrary to the shielding models offered in some literature[31, 32], the duct does not have a circular cross section. In actual fact, the cross section is square[33] or rectangular[34] (see Chapter 4).

For this reason, an approximation technique was developed to estimate equivalent rectangular or square duct sizes. This technique is based on the anlytical equations for the uncollided fluxes from ducts of rectangular, square, and circular cross sectional areas. For a rectangular duct of height, H, and width, W, the uncollided flux[35] at some distance, z, from an isotropic source is

$$\phi_u(z) = \frac{2\phi_o}{\pi} \tan^{-1} \frac{ab}{\sqrt{1 + a^2 + b^2}} . \qquad (3.1)$$

In this equation,

$$a = \frac{H/2}{z} ,$$

$$b = \frac{W/2}{z} ,$$

and ϕ_o is the initial flux.

For a square duct, $a = b = s/2z$,

and so,

$$\phi_u(z) = \frac{2\phi_o}{\pi} \tan^{-1} \frac{s^2}{2z\sqrt{4z^2 + 2s^2}} . \qquad (3.2)$$

Similarly, for a cylindrical duct[36], the uncollided flux is

$$\phi_u(z) = \frac{N_o}{2} \ln (1 + a^2/z^2). \qquad (3.3)$$

for an isotropic source of strength N_o and a duct of diameter, $d = 2a$.

From Appendix E, a correlation of these relations yields

$$\theta = \frac{\pi}{4} \ln x , \qquad (3.4)$$

where

$$\theta = \tan^{-1} \frac{s^2}{2z\sqrt{4z^2 + 2s^2}},$$

and

$$x = 1 + a^2/z^2.$$

Furthermore, for $z = 544.5$ cm and $s < 200$ cm, Appendix E demonstrates that equivalent circular and square duct sizes are related by

$$d = 2s/\sqrt{\pi} . \tag{3.5}$$

Since the duct sizes in question are smaller than 200 cm, the above approximation was used. This meant that the DOT3.5 fluxes for cylindrical ducts of diameter, d, were used to estimate the fluxes for square ducts of side length

$$s = \sqrt{\pi}\ d/2. \tag{3.6}$$

Using this formula, it was possible to calculate the dimensions of square ducts which have cross sectional areas equal to those of the circular ducts tested in the preceding section. Table 3.4 shows these dimensions.

Table 3.4

Dimensions of Circular and Square Ducts of Equivalent Area

Circular d(cm)	Square* s(cm)
0.0	0.0
21.25	18.83
42.50	37.66
85.00	75.33
170.00	150.66

* $s = \frac{\sqrt{\pi}}{2} d$

CHAPTER FOUR

Neutral Beam Analysis

4.1. Beam Parameters

The cross sectional area, length, and shape of the neutral beam duct are important considerations in not only the shielding analysis, but also in the neutral beam injector analysis. These parameters are directly related to the injector design, and impact greatly on both the beam's behavior and efficiency. Of these, the most important parameter is the beam half-width. It determines neutralizer size and gas load, which governs gas line density, beam loss, and injector efficiency. In addition, the half-width is a measure of duct size and first wall opening.

After the beam leaves the neutralizer portion of the injector (see Chapter 2), it passes through a "waist" in the duct before reaching the first wall. The location and size of this waist are functions of the D^+ bending angle. Figure 4.1[37] is a graph of the relation between bending angle and various injector parameters, including waist location.

For the injector shown in Figure 2.3b), the D^+ bending angle was chosen to minimize the duct opening size at the first wall. From Figure 4.1, this results in a bending angle of 72° and a distance (S_w) of 6.9 m from the magnet exit to the beam waist. The beam half-widths corresponding to this bending angle are 0.24 m at the neutralizer entrance, 0.17 m at the exit of the neutralizer,

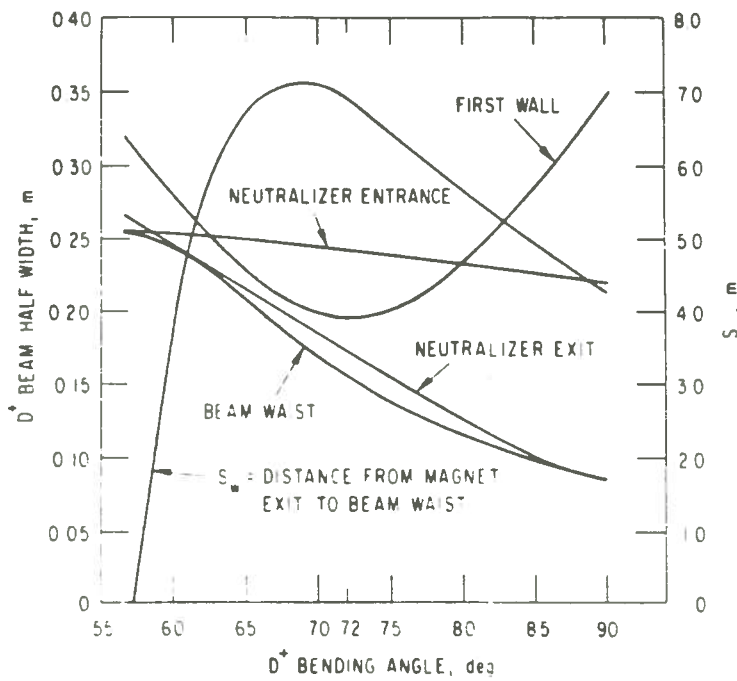

Figure 4.1. Location of beam waist versus D^+ bending angle and beam half-widths at several locations for a D^0 beam injector. (<u>TNS Scoping Studies</u>, Vol. V (1978), page 5.5-24).

0.15 m at the beam waist, and about 0.2 m at the first wall opening.

4.2. Calculational Methods

Preparatory to any discussion of the computations required to deal with neutral beam dynamics, is the presentation of the concept of phase space. In Appendix F, a brief explanation is offered using Hamiltonian methods as given by Lawson.[38] Without going into detail here, phase space is treated as an expansion of Cartesian coordinates from three to six dimensions. The three additional dimensions are actually terms of particle momentum.

Several techniques are available to calculate the beam parameters. The most exact involves the geometrical transport matrices derived from the equations governing the behavior of a particle beam downstream from a converging magnetic quadrapole lens. For such a lens, the beam equations as given by Livingood[39] are of the form,

$$\begin{pmatrix} x \\ x' \end{pmatrix} = \begin{pmatrix} A & B \\ C & D \end{pmatrix} \begin{pmatrix} x_1 \\ x_1' \end{pmatrix} , \qquad (4.1)$$

where

x = any beam position,

$x' = \frac{dx}{dz}$ = additional space component which augments x,

x_1 = beam position at the magnet entrance,

$x_1' = \frac{dx_1}{dz}$,

and A, B, C, and D are beam parameters.

A complete derivation for the lens system in the injector is provided in Appendix F, and is based on information supplied in the General Atomic reports[40]. The resulting matrices for both horizontal and vertical displacement take the same form as those above. However, from the development in Appendix F, the matrices will be written as

$$\begin{pmatrix} y \\ y' \end{pmatrix} = \begin{pmatrix} A & B \\ C & D \end{pmatrix} \begin{pmatrix} y_o \\ y'_o \end{pmatrix} , \qquad (4.2)$$

where y can represent either the x or z directions, and the subscript o refers to the beam at the accelerator grid. Also, the beam parameters are

$$A = \cos \theta/\sqrt{2} - (S/\rho\sqrt{2}) \sin \theta/\sqrt{2},$$

$$B = S_1 \cos \theta/\sqrt{2} + \rho\sqrt{2} \sin \theta/\sqrt{2} + S (\cos \theta/\sqrt{2} - (1/\rho\sqrt{2}) \sin \theta/\sqrt{2}),$$

$$C = - (1/\rho\sqrt{2}) \sin \theta/\sqrt{2},$$

$$D = \cos \theta/\sqrt{2} - (S_1/\rho\sqrt{2}) \sin \theta/\sqrt{2}.$$

In these parameters,

S_1 = free field distance from the exit grid to the first bending magnet.

S = free field distance from the exit of the magnet,

θ = bending angle for the D^+ beam,

and ρ = D^+ beam bending radius.

Although the geometrical transport method is the most exact technique used to calculate beam behavior, a more frequently used technique[41] involves the assumption that the bounding curves of the transverse phase space areas of the beam can be approximated by ellipses. This technique is the emittance method as presented in Lawson[42] (see Appendix F). Emittance is a quantitative measure of the quality of the beam, and is defined as the area of the transverse phase space divided by π.

From a solution to the paraxial equation for a non-laminar particle beam, the emittance can also be defined by the equation

$$\varepsilon = \gamma_o Y^2 + 2\alpha_o Y\, Y' + \beta_o Y'^2, \tag{4.3}$$

where

$$\alpha_o = -\omega\omega',$$

$$\beta_o = \omega^2,$$

$$\gamma_o = \frac{1 + \alpha_o^2}{\beta_o},$$

and ω is a function of the distance of beam travel.

When this equation is modified using geometrical transport beam parameters indicated earlier, the emittance equation can be written as

$$\varepsilon = \gamma y^2 + 2\alpha y y' + \beta y'^2, \tag{4.4}$$

where

$$\alpha = -\gamma_o DB + \alpha_o(BC + DA) - \beta_o AC,$$

$$\beta = \gamma_o B^2 - 2\alpha_o BA + \beta_o A^2,$$
$$\gamma = \gamma_o D^2 - 2\alpha_o DC + \beta_o A^2,$$

The phase space area corresponding to this emittance is

$$S = \pi\omega_o y_{o_{max}}, \tag{4.5}$$

where ω_o is the maximum initial half-angle divergence of the beam. And the beam half-width is given by

$$y_{max} = \sqrt{\beta\varepsilon}, \tag{4.6}$$

where β is defined above.

In the analyses performed by General Atomic,[43] a slightly modified version of this technique was used. This modification involves treating the phase space area as rectangular instead of elliptical. To accomplish this, the phase space area is given by

$$S = 4\omega_o y_{o_{max}}, \tag{4.7}$$

with the resulting emittance defined as

$$\varepsilon = \frac{4}{\pi}\omega_o y_{o_{max}}. \tag{4.8}$$

The change introduces a new value for the parameter β_o such that

$$\beta_o = \frac{\pi y_{o_{max}}}{4\omega_o} \tag{4.9}$$

The characteristics of the particle beam as calculated by each method for the TNS injector (see Figure 2.3b) are listed in Table 4.1[44]. Views of the beam path in the xy-plane are shown

Table 4.1

Some Results of D^+, D^o Beam Transport Calculations

	Case I	Case II	Case III
Initial beam size, 2 y_o max (mxm)	0.348 × 0.348	0.348 × 0.348	0.348 × 0.348
Initial beam 1/2 angle divergence, Ω_o (rad)	0.078	0.078	0.078
Maximum initial beamlet 1/2 angle divergence, ω_o (rad)	0.020	0.020	0.020
Emittance definition	$\omega_o\ y_{o\ max}$	$(4/\pi)\ \omega_o\ y_{o\ max}$	Geometrical transport
β_o definition	$y_{o\ max}/\omega_o$	$(\pi/4) y_{o\ max}/\omega_o$	Geometrical transport
Beam size at neutralizer entrance (mxm)	0.487 × 0.487	0.487 × 0.487	0.572 × 0.572
Beam size at neutralizer exit (mxm)	0.330 × 0.330	0.344 × 0.344	0.472 × 0.472
Beam size at first wall (mxm)	0.306 × 0.306	0.390 × 0.390	0.304 × 0.304
Gas flow out of neutralizer (torr • ℓ/s)	68.5	73.0	142

(<u>TNS Scoping Studies</u>, Vol. V (1978), page 5.5-31) for each method in Figure 4.2. It should be mentioned that the beam bending magnet, ion source, and initial beam size are identical for each case. However, for convenience, they are shown only on the sketch of Case III.

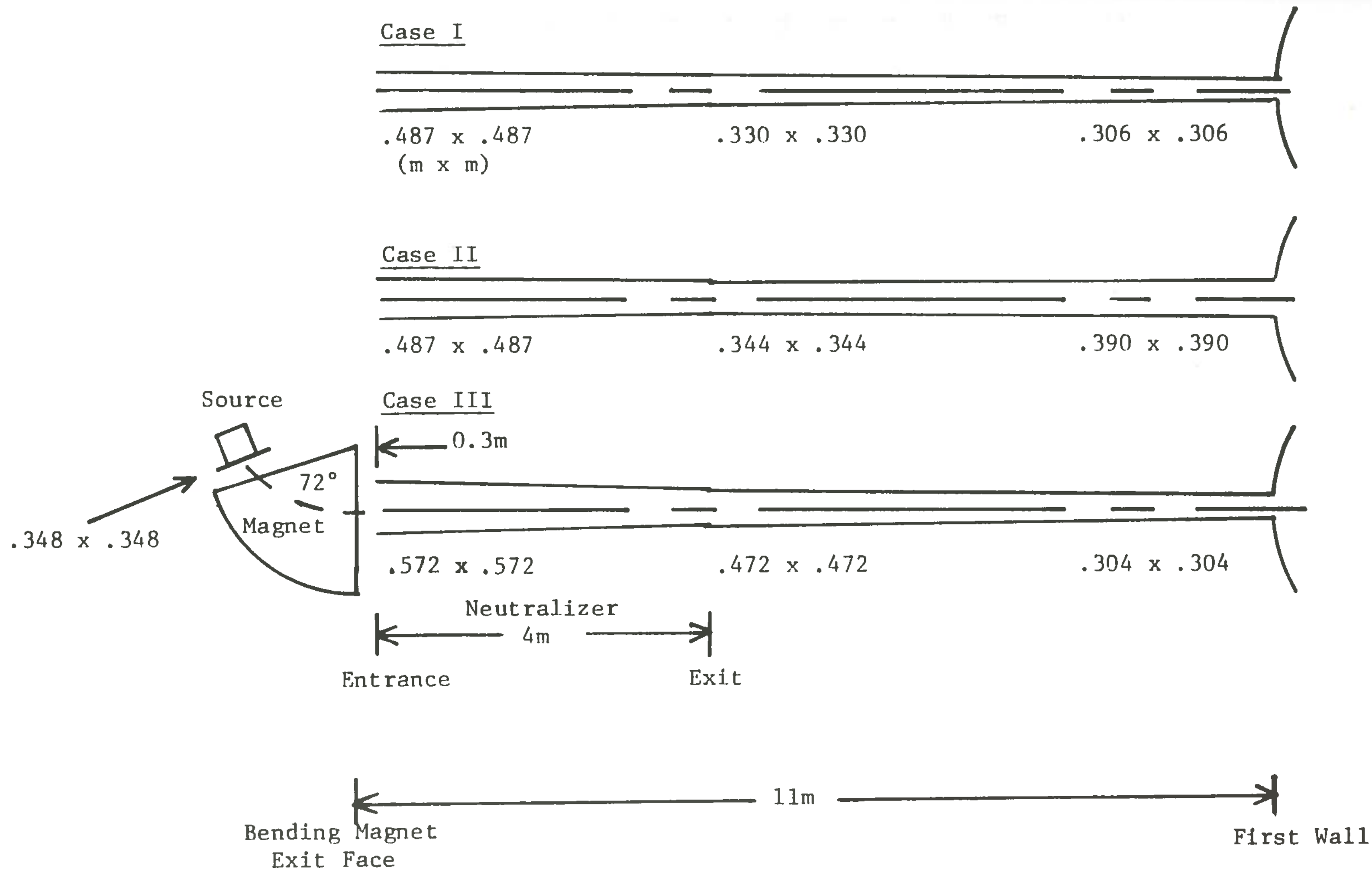

Figure 4.2. Effects of beam transport calculations on the beam shape for TNS injectors.

CHAPTER FIVE

Results, Conclusions, and Recommendations

5.1. General Considerations

The preceding chapters and their appropriate appendices provide a reference base covering the shielding and beam analysis methods for a Tokamak reactor. The line of inquiry followed was intended to establish order-of-magnitude results for both radiological and beam efficiency effects induced by various duct shapes. This chapter is an effort to present those results and consolidate them into a reasonable conclusion. In addition, some direction for future activity will be provided, so that other interested parties can use this thesis as a data base or starting point for their analyses.

5.2. Radiological Impacts of Beam Transport Calculations

The shielding analysis comparisons included here are in terms of the total flux obtained for the ducts in Figure 4.2. The DOT3.5 method developed in Chapter 3 was used, hence, all runs are 7 energy group, P_2-S_4 calculations. The mesh intervals varied from case to case with 41 x 149 (R x Z) in Case I, 43 x 149 in Case II, and 50 x 149 in Case III. A full development of the models is given in Appendix G.

Figure 5.1 illustrates the flux variations resulting from the three duct modeling methods. Each curve represents the total

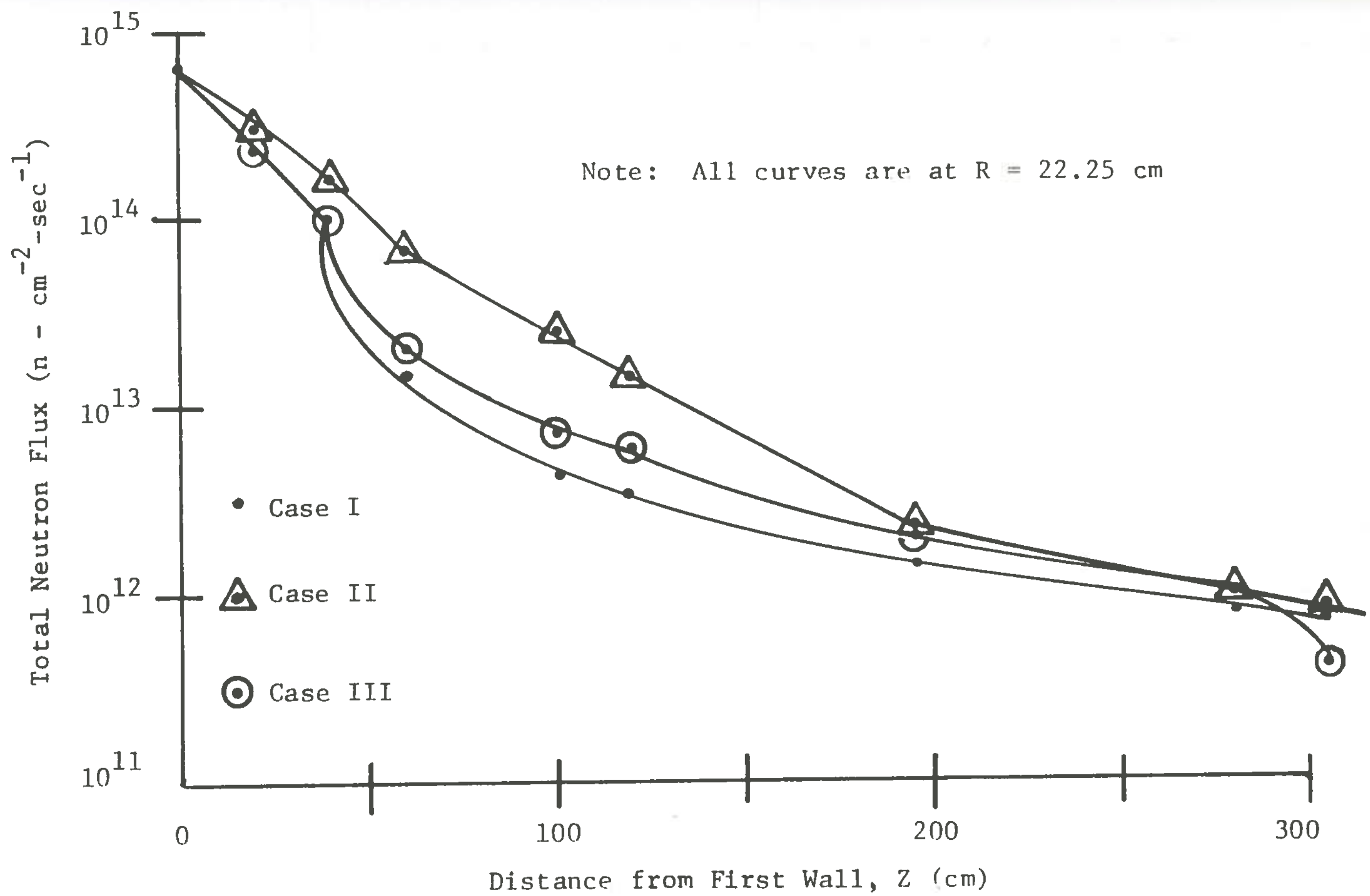

Figure 5.1. Effects of beam transport calculations on DOT3.5 total neutron fluxes.

flux at a distance of 22.25 cm, in the R-direction, from the duct axis. This distance corresponds to about 5 cm from each duct liner. The program results were normalized to a first wall total flux of 6.0×10^{14} neutrons-cm^{-2}-sec^{-1} for each case. The mean percent difference in total flux between Case I and Case III is about 19.5%, with Case III yielding the higher fluxes. A comparison between Cases II and Case III yields a mean percent difference of 121.7%, with Case II being the higher. The variations between cases can be explained by referring to Figure 4.2. In this sketch, it is apparent that Case I should yield the lowest fluxes. The duct in this case has a first wall opening scarcely larger than that of the duct in Case III. In addition, its various cross sectional areas are considerably less than those in Case III. This should render Case I fluxes lower than those in Case III. However, Case III was still expected to yield lower fluxes than Case II, simply because of the considerably larger first wall opening in Case II.

Examination of the total flux at the left and right boundaries of the model is also illuminating, since the left boundary is the duct axis, while the right bisects the TFC. For the left boundary, flux data was highlighted at Z = 544.5 cm, and was assumed to represent the total flux "seen" by the injector internals. A similar type of assumption has been used in other treatments of penetration streaming[45]. For the right boundary, the fluxes at Z = 486 cm, correspond to those at the center of the TFC and are

Table 5.1

Comparison of the Total Neutron Fluxes Due to Beam Transport Calculations

Duct Axis at Z = 544.5 cm*

Case	I	II	III
Flux (n - cm^{-2}-sec^{-1})	6.81 (11)	8.07 (11)	4.88 (11)
%Δ Compared to Case III	39.5	65.4	0.0

Center of TFC (R = 195 cm, Z = 486 cm)

Case	I	II	III
Flux (n - cm^{-2}-sec^{-1})	9.08 (12)	9.75 (12)	9.10 (12)
%Δ Compared to Case III	-0.2	7.1	0.0

* Neutralizer exit is at Z = 910 cm, therefore, this is a conservative approximation for the flux at the injector exit.

assumed to represent the total fluxes "seen" by the TFC. These fluxes are shown in Table 5.1.

5.3. Beam Efficiency Impacts of Beam Transport Calculations

From Figure 4.2, it can be seen that different calculation methods yield similar, but not identical, beam configurations. Two factors of special consideration in determining the preferred method are the first wall beam size and the neutralizer size.[46] As the neutralizer cross section decreases, the first wall opening reaches a minimum value and begins to increase again (see Figure 4.1). The bending angle of the first magnet is chosen at this minimum. For larger bending angles however, the neutralizer size continues to decrease, while the first wall beam size increases.

By choosing the minimum first wall opening, radiation streaming may be minimized, but at the expense of the heating system efficiency. Choosing a small first wall opening or a calculation method which results in such an opening could have detrimental effects. First, decreasing duct size can increase beam scrape off loss, and drive up power requirements of the injector. Appendix H offers a demonstration of this effect as an expansion of the basic injector power flows presented in Appendix A. This expansion yielded the relation

$$P_{supply} = 2.12 \left[1 - f_{so_{min}} \left(\frac{s_{max}}{s_d}\right)^2\right] P_B', \qquad (5.1)$$

where

P_B' = power delivered to the plasma,

$f_{so_{min}}$ = minimum fraction of scrape off occurring at some duct size s_{max},

and s_d = duct size of interest.

From Stacey, et al.[47], the power delivered to the plasma is 40 Mw. And assuming that the geometrical transport method results in a maximum beam injection of 99.7%[48], then the scrape off fraction is only 0.003 and occurs for a duct 30.4 cm on a side. This results in the relation

$$P_{supply} = 84.8 \text{ Mw } [1 - 0.003 (\frac{30.4}{s_d})^2]^{-1}. \qquad (5.2)$$

Equation 5.2 is presented graphically in Figure 5.2. This figure indicates that the duct size could be reduced to 10 cm without significantly increasing scrape off power losses.

In addition to scrape off losses, the various beam transport calculation methods can also result in variations in beam power losses due to dissociative collisions. The particles involved in such collisions are the neutral deuterons of the beam and excess deuterium gas molecules from the neutralizer. The gas forms a blanket in the injection duct, through which the beam must pass. The quantity of gas leaving the neutralizer, and its density, are governed by the beam duct size. And size, as demonstrated in the previous chapter, is dependent on which transport calculation mode is used.

To determine the comparative, order-of-magnitude impact of this situation, the author approximated the beam energy loss using

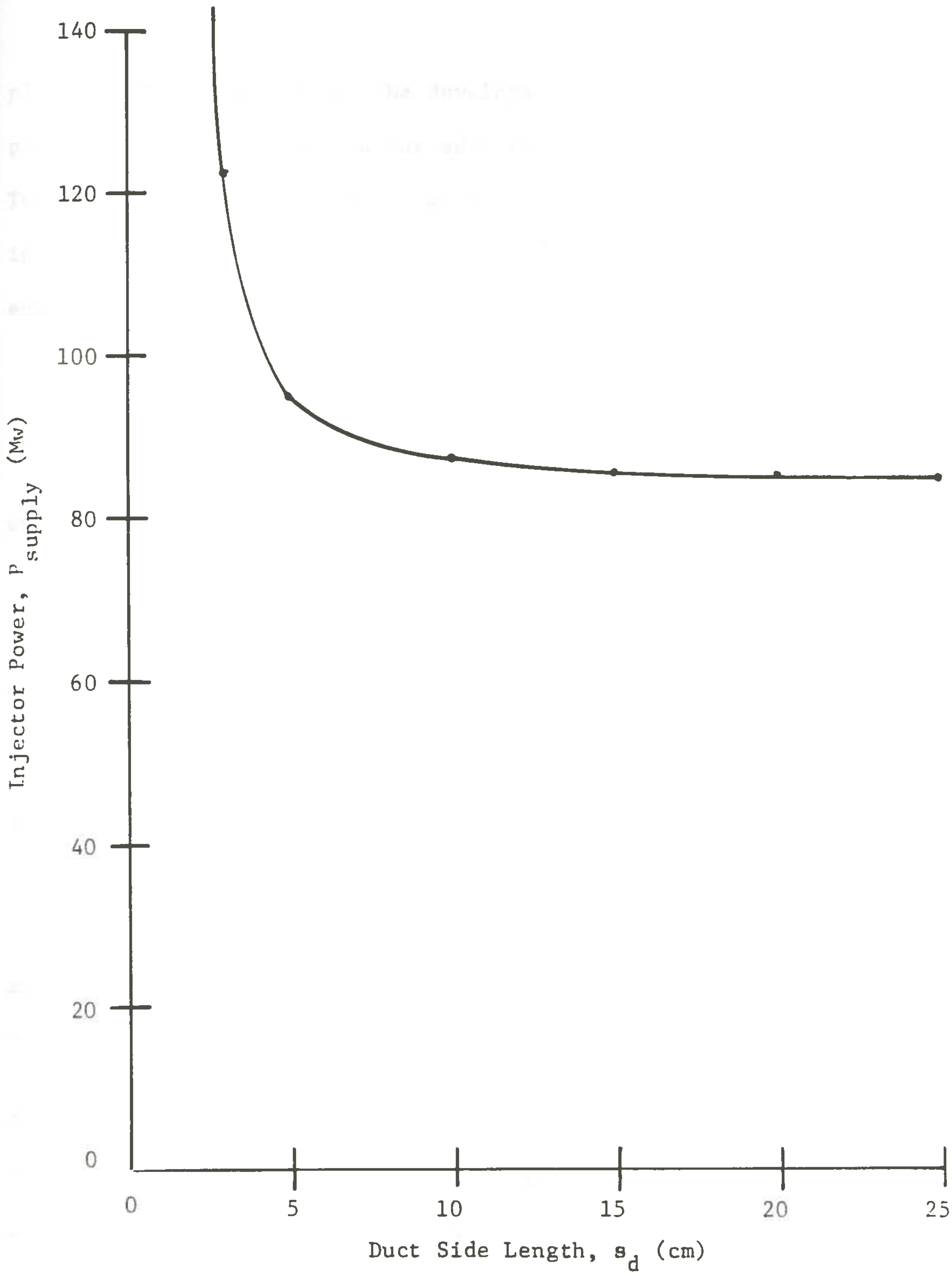

Figure 5.2. Impact of particle scrape off on injector power supply as a function of first wall opening size.

plasma heating equations. The development of these equations is provided in Appendix H, and was adapted from the work of Kammash.[49] The end result was an equation which yields the percent difference in beam energy loss between the various cases in Chapter 4. The equation is

$$\Delta_{a-b}\% = \frac{\ln\,(1/\beta_a^2)}{\ln\,(1/\beta_b^2)} - 1, \tag{5.3}$$

where

a = represents the Base Case,

b = represents a case for comparison,

and β = is a parameter of the gas

$= 1.73 \times 10^{-15}\ n^{1/2}/(kT)^{3/2}$ [50].

In the formula for β,

n = gas density (molecules-cm^{-3}),

T = absolute temperature of gas (°K),

and k = Boltzmann's constant

$= 1.38 \times 10^{-16}$ ergs-$°K^{-1}$.

Assuming that the gas is bled into the neutralizer at 60°F (T = 288.7°K), then kT is 2.48×10^{-5} KeV. Using this assumption and the data presented in Table 4.1, it was possible to calculate $\Delta_{a-b}\%$ (see Appendix H).

Taking Case I as the Base Case, due to the fact that it has the lowest gas density, it was found that Case II resulted in 1.4%

higher energy losses, due to collisions, than the Base Case. Case III had 5.8% higher energy losses than Case I. These percentages can be translated into physically significant values using the injector power flows.

Appendix H contains a modification of the injector equations which includes both scrape off and collision effects. The power requirements for such a system are given by

$$P_{supply} = 2.12\ (1 - f_{so})^{-1}\ (1 - f_c)^{-1}\ P'_B, \qquad (5.4)$$

where P_{supply}, P'_B, and f_{so} have been defined previously. The fractional increase in collisions over the Base Case is given by

$$f_c = \Delta_{a-b}\%/100\%.$$

Table 5.2 presents the results of these calculations, which assume that f_{so} remains constant at 0.003 for all cases (see Figure 5.2), and which hold P'_B constant at 40 Mw. This results in increases in injector power of 1.2 Mw and 5.2 Mw for Cases II and III, respectively. Beam injector efficiency is also given in the table, and represents the ratio of P'_B to P_{supply}.

5.4. Conclusions

Table 5.3 provides a summary of the results obtained in the preceding sections. Based on both radiological and beam efficiency considerations, Case I appears to be the most desirable beam path model. The analysis based on this model provides the

Table 5.2

Relative Effects of Dissociative Collisions on Injector Power Requirements for Various Beam Transport Calculations

	Case I	Case II	Case III
$\Delta_{a-b}\%$	0.0	+ 1.4	+ 5.8
f_c	0.0	0.014	0.058
P_{supply} (Mw)	85.0	86.2	90.2
ΔP_{supply} (Mw)	0.0	1.2	5.2
$\eta_{injector}$ (%)*	47.0	46.4	44.3

$$* \ \eta_{injector} = \frac{\text{Power delivered to plasma } (P_B')}{\text{Power supplied to injector } (P_{supply})} \times 100\%$$

Table 5.3

Summary of the Relative Effects of Beam Transport Calculations on Total Neutron Fluxes and Injector Power

	Case I	Case II	Case III
Radiological:			
Flux @ Injector ($n - cm^{-2}-sec^{-1}$)	6.81 (11)	8.07 (11)	4.88 (11)
Flux @ TFC ($n - cm^{-2}-sec^{-1}$)	9.08 (12)	9.75 (12)	9.10 (12)
Δ% at TFC	-0.2	7.1	0.0
Injector:			
Efficiency (%)	47.0	46.4	44.3
ΔP_{supply} (Mw)	0.0	1.2	5.2

Base Case for collision energy losses, and also yields a total flux at the center of the toroidal field coils which is lower than the geometrical transport calculations in Case III. The reader will recall that Case I is the emittance method defined by

$$\varepsilon = \omega_o y_{o_{max}} .$$

It should be mentioned that researchers at General Atomic selected Case II(51) as their reference beam design. However, this was a tentative selection pending identification of such items as scrape off and dissociative collision losses. The author hopes that the conclusion reached in this thesis will be borne out by detailed analyses of the factors involved.

5.5. Recommendations for Future Studies

One expansion of the trade-off study which seems particularly intriguing, is the development of an "optimum" penetration--a duct which would have the least overall impact on the reactor systems. It would represent the breakpoint at which decreasing radiation loading on the TFC magnets would match increasing injector system efficiency. The correlation of these two dissimilar quantities requires a common frame of reference. Such a reference frame seems to be the station service or auxiliary electrical power requirements of the reactor subsystems involved.

Since the TFC is a superconducting magnet, it consumes station service power in two ways: as current to produce the necessary magnetic fields, and as refrigeration power to drive the helium and nitrogen cooling systems. As the duct size increases, the flux to the magnets increases. This induces heating effects in the coils, and thereby, increases the load which the refrigeration system must bear. In addition, it increases the resistivity of the coils. Both effects drive its electrical consumption upward. Therefore, increasing duct size leads to increasing auxiliary power requirements.

Conversely, beam injector efficiency is the ratio of useful power delivered to the plasma divided by net power consumed in the injector system. As shown in this paper, the power supply of the system is dependent on a number of factors. Two of these are the particle scrape off and the collision losses. Since these factors are functions of duct size, they provide a method of relating duct size to reactor power. As these losses increase, auxiliary power requirements rise, and net output decreases.

The optimum, unshielded duct size should be at the intersection of two curves. One would be TFC power requirements as a function of duct size. The other curve would be injector power supply vs duct size. Determination of this reactor parameter should lead to a cost benefit analysis of the system. It might weigh power costs against capital investment and/or operation and maintenance cost variations induced by the above optimization.

The importance of such an optimization effort lies in the fact that if controlled thermonuclear fusion is to be a viable energy option in the future, then it must be economically viable as well as technically feasible. The revenue received from any power generating facility is determined by the net power output of the plant. Hence, any optimization which can limit the auxiliary power requirements of the reactor will also increase the net power derived from the facility and improve its chances for economical operation.

REFERENCES

1. R. T. Santoro, R. A. Lillie, R. G. Alsmiller, Jr., and J. M. Barnes, "Two and Three-Dimensional Neutronics Calculations for the TFTR Neutral Beam Injectors," ORNL-TM-6354, Oak Ridge National Laboratory (1978).

2. W. M. Stacey, Jr., et al., "A Tokamak Experimental Power Reactor," Nuclear Technology, 30, 3 (1976).

3. Project Staff - General Atomic Company and Argonne National Laboratory, "Program Considerations and Reactor Designs", GAC-ANL TNS Scoping Studies, GA-A14614, Vol. II (1978).

4. W. M. Stacey, Jr., et al., Ref. 2, page 264.

5. W. M. Stacey, Jr., et al., Ref. 2, page 271.

6. T. Ide, Y. Seki, and H. Iida, "Evaluation of Neutron Streaming Through Injection Ports in a Tokamak-Type Fusion Reactor," JAERI-M6475, JAERI (1976).

7. R. T. Santoro, R. A. Lillie, R. G. Alsmiller, Jr., and J. M. Barnes, Ref. 1, page 1.

8. Project Staff - General Atomic Company and Argonne National Laboratory, Ref. 3, page 2.3-14.

9. T. H. Batzer, et al., "Conceptual Design of a Mirror Reactor for a Fusion Engineering Research Facility (FERF)", UCRL-51617, Lawrence Livermore Laboratory (1974).

10. R. T. Santoro, R. A. Lillie, R. G. Alsmiller, Jr., and J. M. Barnes, Ref. 1, page 7.

11. Project Staff - Argonne National Laboratory, "Support Engineering, Tritium and Neutronics", GAC-ANL TNS Scoping Studies, GA-A14614, Vol. V (1978).

12. W. M. Stacey, et al., Ref. 2, page 284.

13. R. T. Santoro, R. A. Lillie, R. G. Alsmiller, Jr., and J. M. Barnes, Ref. 1, page 3.

14. M. A. Abdou, L. J. Milton, J. C. Jung, and E. M. Gelbard, "Multidimensional Neutronics Analysis of Major Penetrations in Tokamaks," Proceedings: Second ANS Topical Meeting on the Technology of Controlled Nuclear Fusion, USERDA-CONF-760935-P3 (1976).

15. M. A. Abdou and J. C. Jung, "Nuclear Analysis of a Tokamak Experimental Power Reactor Conceptual Design", Nuclear Technology, 35, (1977).

16. R. T. Santoro, R. A. Lillie, R. G. Alsmiller, Jr., and J. M. Barnes, Ref. 1, page 2.

17. W. W. Engle, Jr., "A Users Manual for ANISN, a One-Dimensional Discrete Ordinates Transport Code with Anisotropic Scattering," K-1693, CTC, UCC-ND (1973).

18. F. R. Mynatt, et al., "The DOT III Two-Dimensional Discrete Ordinates Transport Code," ORNL-TM-4280, Oak Ridge National Laboratory (1973).

19. M. A. Abdou and J. C. Jung, Ref. 15, page 73.

20. T. Ide, Y. Seki, and H. Iida, Ref. 6, page 10.

21. T. Kammash, Fusion Reactor Physics: Principles and Technology, Ann Arbor Science Publishers, Inc., (1975).

22. T. Kammash, Ref. 21, page 387.

23. R. T. Santoro, telephone conversation with the author, (9/25/78).

24. M. A. Abdou and J. C. Jung, Ref. 15, page 57.

25. F. Dolatshahi, "Preparation of Broad-Group Cross-Sections for Multigroup Calculations--ANISN Computer Code Option," M.S. Thesis, LSU (1978).

26. M. A. Abdou, L. J. Milton, J. C. Jung, and E. M. Gelbard, Ref. 14, page 4.

27. M. A. Abdou and J. C. Jung, Ref. 15, page 70.

28. M. A. Abdou, L. J. Milton, J. C. Jung, and E. M. Gelbard, Ref. 14, page 15.

29. F. R. Mynatt, et al., Ref. 18, page 46.

30. F. R. Mynatt, et al., Ref. 18, page 42.

31. T. Ide, Y. Seki, and H. Iida, Ref. 6, page 1.

32. M. A. Abdou, L. J. Milton, J. C. Jung, and E. M. Gelbard, Ref. 14, page 2.

33. Project Staff - Argonne National Laboratory, Ref. 11, page 5.5-23.

34. R. T. Santoro, R. A. Lillie, R. G. Alsmiller, Jr., and J. M. Barnes, Ref. 1, page 5.

35. N. M. Schaeffer, Editor, Reactor Shielding for Nuclear Engineers, USAEC Office of Information Services, (1973).

36. E. P. Blizzard, Editor, "Shielding", Reactor Handbook, Vol. IIIB, Interscience Publishers, (1962).

37. Project Staff - Argonne National Laboratory, Ref. 11, page 5.5-24.

38. J. D. Lawson, The Physics of Charged-Particle Beams, Clarendon Press, Oxford, (1977).

39. J. J. Livingood, Cyclic Particle Accelerators, D. Van Nostrand Co., Inc., (1961).

40. Project Staff - Argonne National Laboratory, Ref. 11, page 5.5-25 through 5.5-27.

41. Project Staff - Argonne National Laboratory, Ref. 11, pages 5.5-28 through 5.5-30.

42. J. D. Lawson, Ref. 34, pages 184-185.

43. Project Staff - Argonne National Laboratory, Ref. 11, page 5.5-30.

44. Project Staff - Argonne National Laboratory, Ref. 11, page 5.5-31.

45. M. A. Abdou, L. J. Milton, J. C. Jung, and E. M. Gelbard, Ref. 14, page 4.

46. Project Staff - Argonne National Laboratory, Ref. 11, page 5.5-24.

47. W. M. Stacey, Jr., et al., Ref. 2, page 274.

48. Project Staff - Argonne National Laboratory, Ref. 11, page 5.5-32.

49. T. Kammash, Ref. 21, pages 81 through 102.

50. T. Kammash, Ref. 21, page 92.

51. Project Staff - Argonne National Laboratory, Ref. 11, page 5.5-32.

APPENDIX A

Tokamak Power Calculations

A.1. Reactor Power

During the burn phase, the reactor power is given by

$$P = C_1 n^2 \overline{\sigma v}\, V_p, \tag{A.1}$$

where C_1 = constant

n = D-T ion density

$\overline{\sigma v}$ = Maxwellian average fusion cross-section,

and V_p = plasma volume.

The ion density is a function of the ratio of plasma thermal pressure and poloidal field strength, therefore,

$$n \propto \frac{\beta_\theta I_p^2}{a^2 T}, \tag{A.2}$$

where β_θ = the ratio in question,

I_p = plasma current,

a = plasma minor radius,

and T = plasma temperature.

The plasma current is limited by stability considerations, such that

$$I_p \propto \frac{aB_t}{qA}, \tag{A.3}$$

where B_t = toroidal field strength,

A = major radius/minor radius

= R/a

and q = stability factor.

The above relations yield

$$P = C_1 [\frac{\beta_\theta}{a^2 T} (\frac{aB_t}{qA})^2]^2 \overline{\sigma v} V_p. \qquad (A.4)$$

In the above equation, all parameters are nearly constant except B_t. Therefore,

$$P \simeq CB_t^4, \qquad (A.5)$$

where $$C = C_1 [\frac{\beta_\theta^2}{T} (\frac{1}{qA})^2]^2 \overline{\sigma v} V_p.$$

The toroidal field strength is affected by the radius of the torus, hence,

$$B_t = (\frac{r_v + \Delta_m}{R}) B_{max}^{TFC}.$$

From Figure 2.1, it can be seen that

$$r_v = R - (r_w + \Delta_B + \Delta_s + \Delta_m),$$

with B_{max}^{TFC} as the maximum field strength at the surface of the oroidal field coils. This yields

$$B_t = \left(\frac{R - (r_w + \Delta_B + \Delta_s + \Delta_m) + \Delta_m}{R}\right) B_{max}^{TFC}$$

$$= \left(1 - \frac{r_w + \Delta_B + \Delta_s}{R}\right) B_{max}^{TFC}. \quad (A.6)$$

Substituting this relation into Equation A.5, yields the reactor power equation,

$$P = C \left(1 - \frac{r_w + \Delta_B + \Delta_s}{R}\right) (B_{max}^{TFC})^4, \quad (A.7)$$

or

$$P \propto \left(1 - \frac{r_w + \Delta_B + \Delta_s}{R}\right) (B_{max}^{TFC})^4.$$

A.2. Injector Power Flow

Figure A.1 shows the power flow diagram for a neutral beam injector system of the type proposed for the TFTR. As given by Stacey, et al. (Reference 47), the power component equations are

$$P_{supply} = P_{in} - P_{TR} - P_{DC}, \quad (A.8)$$

$$P_{DC} = \eta_{DC} (P_{D2,3} + P_{D+}), \quad (A.9)$$

$$P_{TR} = \eta_{TR} (P_{LS} + P_{L1} + P_{L2}), \quad (A.10)$$

$$P_{in} = kP_+ \sum_1^3 \Gamma_j, \quad (A.11)$$

$$P_{out} = P_+ \sum_1^3 \Gamma_j \quad (A.12)$$

$$P_{LS} = (k - 1) P_+ \sum_1^3 \Gamma_j \quad (A.13)$$

$$P_{D2,3} = \tau_1 P_+ \sum_1^3 (1 - \varepsilon_j) \Gamma_j, \quad (A.14)$$

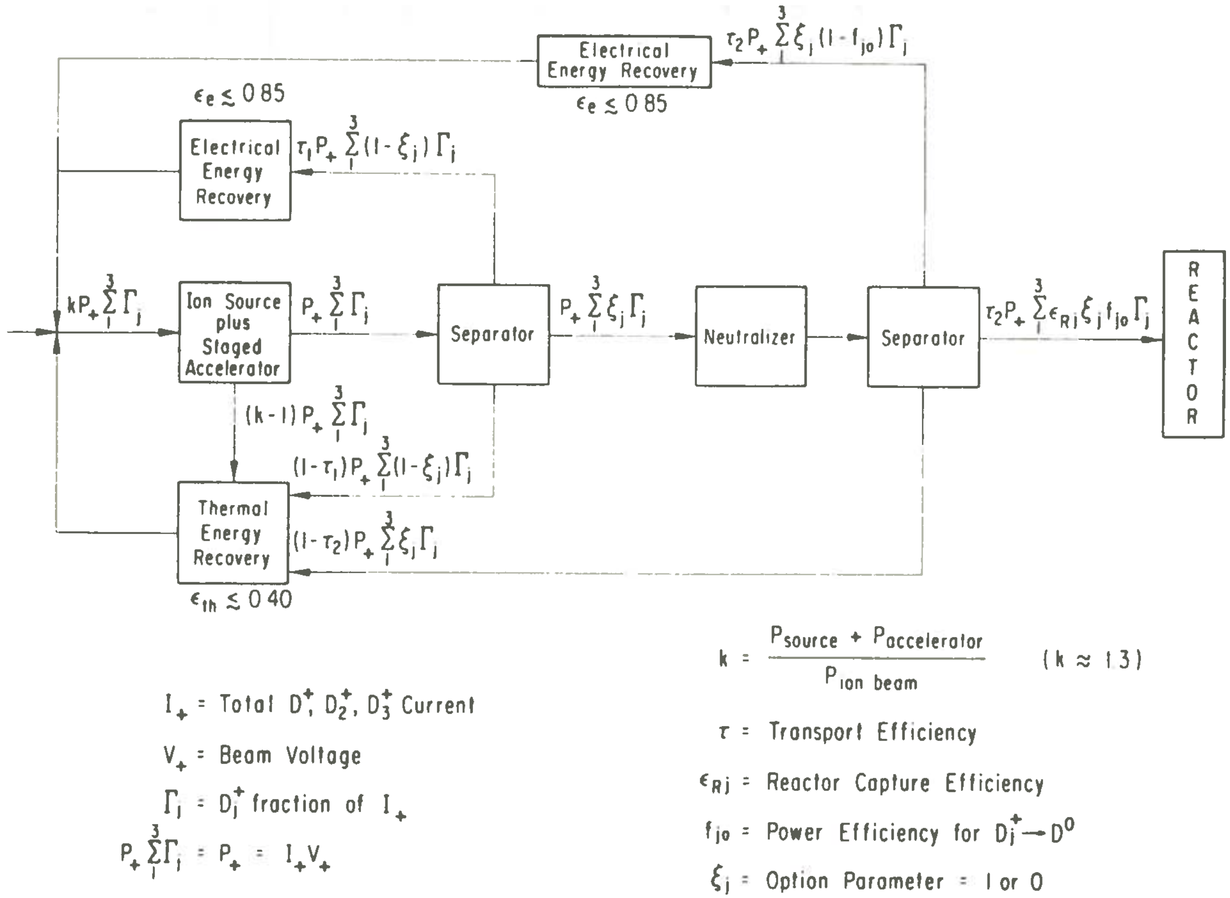

Figure A.1. ANL neutral-beam production model for $D_j^+ \rightarrow D^o$, j = 1, 2, 3, with the ion beam accelerated to full energy before optional removal of molecular components. (Nuclear Technology, 30, 3, Sept. 1976, page 284).

$$P_{L1} = (1 - \tau_1)\ P_+ \sum_1^3 (1 - \varepsilon_j)\ \Gamma_j, \qquad (A.15)$$

$$P_N = P_+ \sum_1^3 \varepsilon_j\ \Gamma_j, \qquad (A.16)$$

$$P_{D+} = \tau_2\ P_+ \sum_1^3 \varepsilon_j\ (1 - f_{jo})\ \Gamma_j, \qquad (A.17)$$

$$P_{L2} = (1 - \tau_2)\ P_+ \sum_1^3 \varepsilon_j\ \Gamma_j, \qquad (A.18)$$

and

$$P_B = \tau_2\ P_+ \sum_1^3 \varepsilon_{Rj}\ \varepsilon_j\ f_{jo}\ \Gamma_j. \qquad (A.19)$$

For a D° injector, Stacey, et al. (Ref. 47) suggests a beam composed of 75% D^+, 18% D_2^+, and 7% D_3^+. This yields values of 0.75, 0.18, and 0.07 for Γ_1, Γ_2, and Γ_3, respectively. The reactor capture efficiency is identical for all particles, therefore,

$$\varepsilon_{R1} = \varepsilon_{R2} = \varepsilon_{R3} = 0.95.$$

Since D^+ is the beam component of interest, then the option parameters ε_1, ε_2, and ε_3 are given as 1,0, and 0, respectively. The bending magnet transport efficiencies (τ_j) are 1.0 for magnet #1 and 0.8 for magnet #2. The ratio (k) of power entering the ion source and accelerator, to power leaving with the ion beam is 1.3. And the energy recovery efficiencies are 40% for the thermal system (n_{TR}) and 85% for the direct conversion beam dumps (n_{DC}).

For the reactor in question, the neutral beams must deliver 40 Mw of power, and will require 160 Mw of ion source and accelerator power. Therefore,

$$P_B = 40 \text{ Mw}$$

and

$$P_{in} = 160 \text{ Mw}.$$

Since $\sum_{1}^{3} \Gamma_j = 1$, then

$$P_{in} = kP_+ = 1.3\ P_+.$$

Therefore, $P_+ = \frac{P_{in}}{1.3} = 123$ Mw.

Since $P_B = \tau_2\ P_+ \sum_{1}^{3} \varepsilon_{Rj}\ \varepsilon_j\ f_{jo}\ \Gamma_j$,

then $40\ \text{Mw} = 0.8 \times 123 \times [(0.95 \times f_{10} \times 0.75) + 0 + 0]$,

and $f_{10} = 0.57$.

Using these values, the power flow quantities become

$$P_{supply} = 84.8\ \text{Mw},$$

$$P_{DC} = 53.1\ \text{Mw},$$

$$P_{TR} = 22.1\ \text{Mw},$$

$$P_{in} = 160\ \text{Mw},$$

$$P_{out} = 123\ \text{Mw},$$

$$P_{LS} = 37\ \text{Mw},$$

$$P_{D2,3} = 30.8\ \text{Mw},$$

$$P_{L1} = 0.0\ \text{Mw},$$

$$P_N = 92.2 \text{ Mw},$$

$$P_{D+} = 31.7 \text{ Mw},$$

$$P_{L2} = 18.5 \text{ Mw},$$

and

$$P_B = 40 \text{ Mw}.$$

It should be mentioned that

$$P_N \neq P_{D+} + P_{L2} + P_B,$$

since 5% of the beam entering the plasma is not used. This quantity is about 2 Mw, so

$$P_N = P_{D+} + P_{L2} + P_D + 2 \text{ Mw}.$$

APPENDIX B

ANISN Parameter Studies

B.1. General Considerations

As mentioned earlier, the parameter studies of ANISN were instituted to clarify numerous questions involving the impacts of various inputs on the solution method. The most critical of these appeared to be cross section library selection, the order of scatter and order of angular quadrature, and the number of mesh intervals. In addition, the impacts due to the input data required in the 16* array of ANISN were questionable. For reference purposes, a summary of ANISN inputs is included at the end of Appendix B.

B.2. Cross Section Comparison

Two cross section libraries were available for use in the ANISN calculations. Both have neutron energy spectrums which are peaked in the MeV range, so that they are compatible with fusion reactor problems. The libraries were DLC-37D, with 100 neutron and 21 gamma groups, and DLC-41/VITAMIN C, with 35 neutron and 21 gamma groups. In the comparison runs, it was planned to collapse DLC-37D to 7 neutron and 1 gamma groups, and check it against uncollapsed DLC-41 results. However, attempts to collapse DLC-37D using ANISN were plagued with poor convergence, and were eventually abandoned.

One difference between the two cross section libraries, which could have affected fusion problem results, was that DLC-41 contained cross sectional data for deuterium and tritium, while

DLC-37D did not. For this reason, it was necessary to run DLC-37D problems with a hydrogen plasma. To nullify any possible discrepancies which might result from comparing a D-T plasma to one composed of hydrogen, the problems were run using shell sources located at the plasma outer radius.

The results shown in Table B.1 are for a DLC-41 run and an uncollapsed run of DLC-37D. As can be seen, the average difference between the results is about 5%, and does not support the choice of one library set over the other. Therefore, the decision to use DLC-41/VITAMIN C in preference to DLC-37D was made based on other factors. Most important of these was that the DLC-41 library contained cross section data for deuterium and tritium. In addition, due to the problems encountered in attempting to collapse DLC-37D, it was decided to use uncollapsed DLC-41 data. This meant that the total flux results could be correlated in about one-third the time.

B.3. Source Term Comparison

As stated above, a shell source was used in the cross section comparison runs to remove any discrepancies caused by plasma composition. In fact, shell sources were used in a number of the early runs in which other parameters were being compared. All other factors being equal, the percent difference in results caused by the variation of a particular parameter will be the same regardless of the source term.

It was anticipated that the DOT3.5 problems would have a D-T plasma represented by a distributed rather than a shell source.

Table B.1

Comparison of ANISN Total Neutron Fluxes for DLC-37D vs. DLC-41/VITAMIN C

Total Flux ($n - cm^{-2}-sec^{-1}$)*

Distance from Plasma Axis (cm)	DLC-37D	DLC-41/VITAMIN C
245	5.96 (14)	5.96 (14)
280	3.61 (13)	3.45 (13)
300	5.76 (12)	6.34 (12)
310	2.29 (12)	2.55 (12)
315	2.08 (12)	2.30 (12)
336	3.65 (11)	4.12 (11)
338	1.87 (11)	1.87 (11)

* Normalized to 1st wall flux in JAERI reactor of 5.96 (14) $n - cm^{-2}-sec^{-1}$.

Therefore, the author decided to test the impact of the source configuration on a shielding problem such as this. The results are shown in Table B.2, and indicate that a distributed source will result in a total flux which differs from that produced by a shell source by an average of less than 3%.

B.4. Order of Scatter and Order of Angular Quadrature

Two areas of interest in the parameter sensitivity testing of ANISN were the effects of the order of the Legendre polynomial expansion (ℓ), and the order of angular quadrature (N). It was known that the accuracy of the solution was dependent on the scatter order, ℓ, since this increases the number of roots in the approximation. Furthermore, it was known that odd-order approximations ($P_{2\ell-1}$) were often used instead of even-order ($P_{2\ell}$) solutions, since both contain the same number of roots (ℓ).

P_ℓ variations were checked with $\ell = 1$ and $\ell = 2$. The results are shown on Figure B.1, and listed in Table B.3a). It was found that P_1 calculations averaged 138% higher total flux values than P_2. In addition, for this particular problem, the P_1 run used about 20% less CPU time than the P_2 solution. However, it was observed on other problems that using a P_2 rather than a P_1 calculation enhanced the convergence of the solution, and actually reduced computer time.

The order of angular quadrature was checked for N = 4 and N = 10. As can be seen in Table B.3b), the S_{10} solution resulted in fluxes which were about 8% higher than the S_4 values.

Table B.2

Comparison of ANISN Total Neutron Fluxes for Distributed vs. Shell Sources

Total Flux (n - cm^{-2}-sec^{-1})*

Distance from Plasma Axis (cm)	Distributed Source	Shell Source
245	5.96 (14)	5.96 (14)
280	3.61 (13)	3.45 (13)
300	6.06 (12)	6.34 (12)
310	2.43 (12)	2.55 (12)
315	2.19 (12)	2.30 (12)
336	3.89 (11)	4.12 (11)
338	1.77 (11)	1.87 (11)

* Normalized to 1st wall flux in JAERI reactor of 5.96 (14) n - cm^{-2}-sec^{-1}.

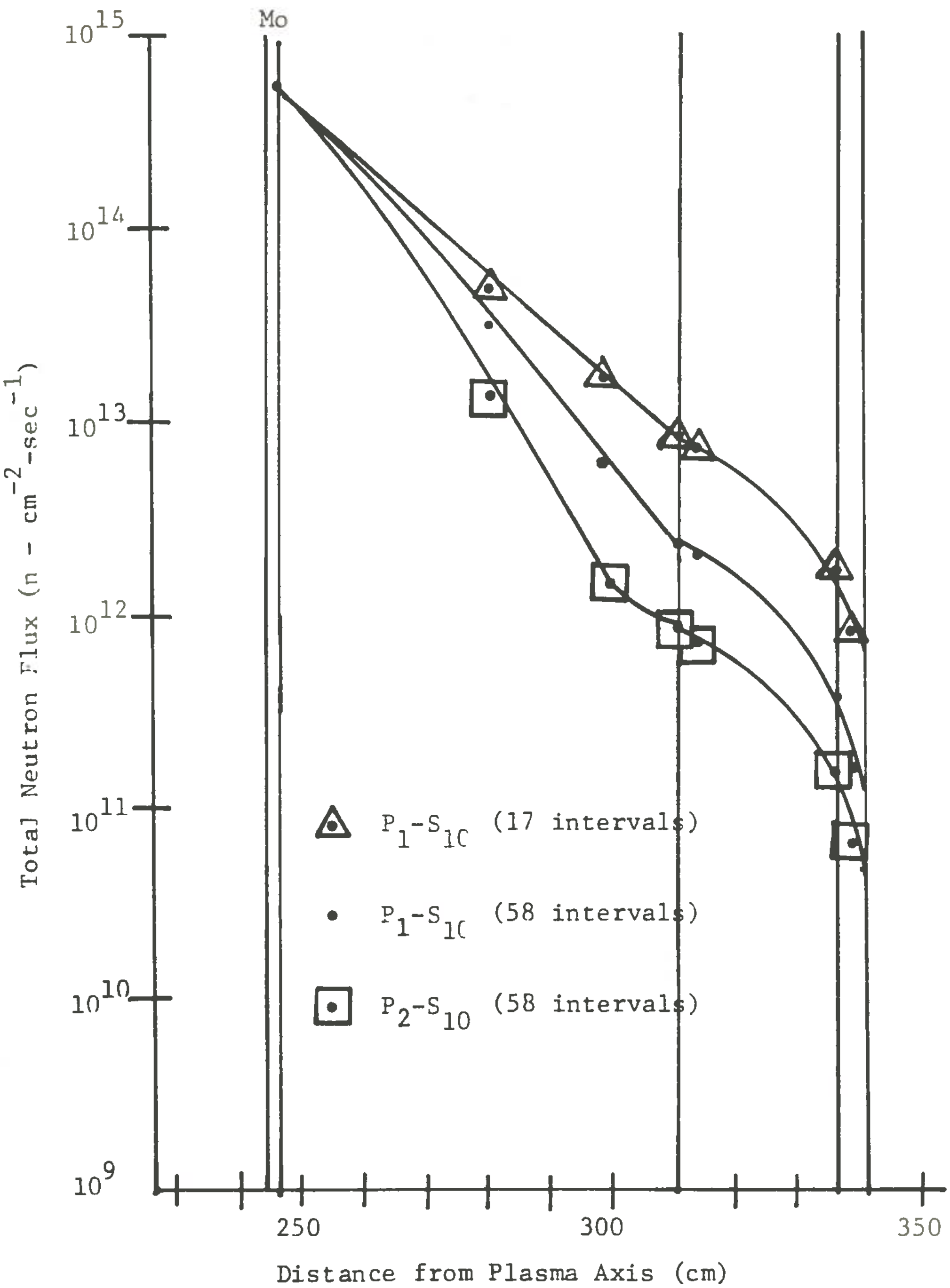

Figure B.1. Effects of scatter order and interval number variations on ANISN total fluxes calculated for the JAERI Tokamak.

Table B.3

Comparison of ANISN Total Neutron Fluxes for P_1 vs. P_2 and S_4 vs. S_{10} Calculations

Total Flux ($n - cm^{-2}-sec^{-1}$)*

Distance from Plasma Axis (cm)		
a) Order of Scatter (P_ℓ)	$\ell = 1$	$\ell = 2$
245	5.96 (14)	5.96 (14)
280	3.70 (13)	1.34 (13)
300	6.08 (12)	2.24 (12)
310	2.39 (12)	8.97 (11)
315	2.13 (12)	8.05 (11)
336	3.77 (11)	1.63 (11)
338	1.67 (11)	6.46 (10)
b) Order of Angular Quadrature (S_N)		
	N = 4	N = 10
245	5.96 (14)	5.96 (14)
280	3.42 (13)	3.70 (13)
300	5.53 (12)	6.08 (12)
310	2.17 (12)	2.39 (12)
315	1.94 (12)	2.13 (12)
336	3.31 (11)	3.77 (11)
338	1.49 (11)	1.67 (11)

* Normalized to 1st wall flux in JAERI reactor of 5.96 (14) $n - cm^{-2}-sec^{-1}$.

B.5. Number of Mesh Intervals

As stated above, in a discrete ordinate solution, the problem is solved in terms of a number of mesh intervals. It should be apparent that the greater the number of intervals, then the better the approximation will be. It should also be apparent that by increasing the number of intervals, the complexity of the problem will be increased. Hence, the time required to model and run the program will increase. Since the mesh interval number will become even more important in a two-dimensional DOT3.5 run, it was decided to test the response of ANISN to the mesh interval number.

Table B.4 describes the two models considered. One has 17 intervals, while the other has 58 intervals. All other factors are identical. The behavior of the results is illustrated by Figure B.1. Interestingly enough, drastically reducing the number of intervals on this problem reduced the CPU time by only 50%. This was apparently caused by the poorer convergence properties of the 17 interval model. Clearly, care should be taken in any attempt to greatly reduce the mesh spacing of a large problem. A good rule-of-thumb in sizing mesh spaces is that very low density regions, or regions with low cross sections can consist of few intervals. High density or strongly interacting regions require a fine mesh structure.

B.6. Cylinder Height

One factor which can greatly affect the results of an ANISN run in cylindrical geometry is cylinder height, variable DY in the

Table B.4

Interval Number per Region for ANISN Calculations
Using the JAERI Tokamak Models

Region	17 Interval Model	58 Interval Wall
Plasma	3	11
Vacuum	3	10
1st Wall	2	2
Blanket (Li_2O)	5	24
Blanket (Graphite)	3	10
Outer Wall	1	1
	17	58

16* array. The parameter is included to account for neutron leakage from the ends of the cylinder, since in a one-dimensional problem, only left and right boundary conditions can be specified. This differs from the procedure used in DOT3.5, since in a two-dimensional code, boundary conditions can be specified for the top, bottom, left, and right.

In the JAERI problem, the fusion reactor was a torus composed of wedge-shaped sections. One wedge was modeled and assumed to have a height equal to the outer radius of the blanket/shield structure. This yielded DY = 340 cm, and ANISN was run with 58 intervals as a P_2-S_{10} problem. Next, it was assumed that since a torus is an "endless" cylinder, then the cylinder height should be infinite. To approximate this, a cylinder height of 1×10^6 cm was arbitrarily chosen so that DY >> R. Naturally, this resulted in a decrease in leakage, and increased the total flux by an average of 150%. The comparison between DY = 340 cm and DY = 1×10^6 cm is shown in Figure B.2.

B.7. Other Parameters

Variation in boundary conditions, from reflective to white with an albedo of 1.0, brought no change in ANISN. However, the DOT3.5 manual warns that a white boundary is more difficult to converge. This caveat was taken, and reflective boundary conditions were used in the DOT3.5 runs.

A great many other parameters were encountered in the ANISN runs. These included the fission spectrum (1*), the flux guess (3*), and the variables in the 15* array. None of these items were

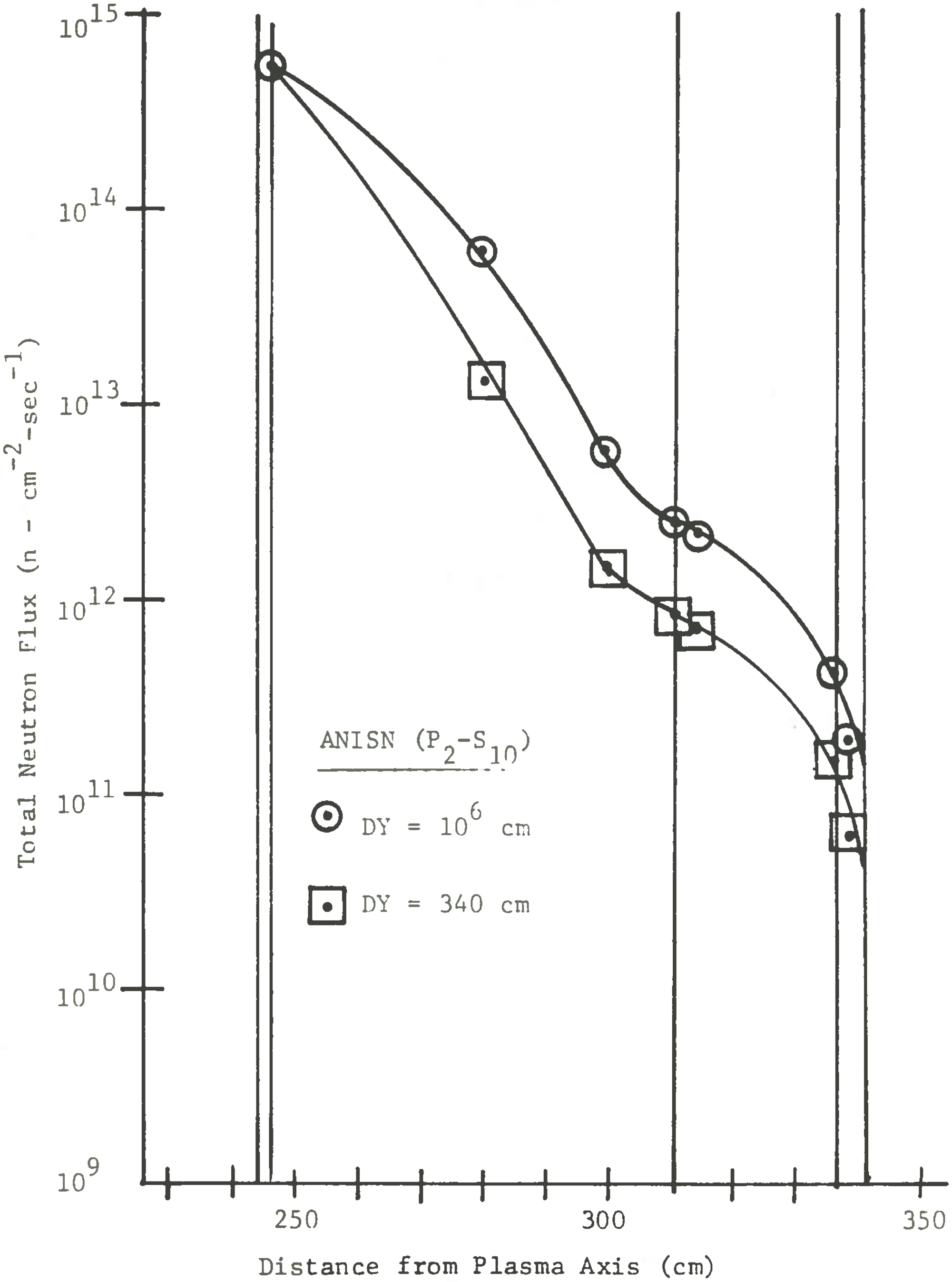

Figure B.2. Effects of cylinder height parameter on ANISN total fluxes calculated for the JAERI Tokamak.

found to affect the solution of this particular problem. This does not necessarily indicate that they can be disregarded in all situations. It does mean that within the range of values recommended for use in this problem, variations in these variables was not critical.

B.8. Multigroup vs. Few Group Calculations

One of the major limiting factors on the run time of a DOT3.5 problem is the number of energy groups to be treated. This follows from the fact that the program performs its calculations on a group-by-group basis. Hence, if a problem were reduced from 56 groups to only 7 groups, one might suppose that the CPU time required would be reduced by a factor of eight. When this supposition was tested using ANISN, it was found that CPU time did indeed drop, but by a factor of 6.3.

The ANISN 7 group run was performed using cross section data on cards. The cards were prepared from an ANISN run which collapsed the cross sections on the 56 group, DLC-41/VITAMIN C group independent tape into 6 neutron groups and one gamma group. The problem solved was for the ANL model, and the total flux results were compared in Figure B.3.

The method used to determine the number of multigroups per few group involves developing few group energy boundaries which result in nearly constant lethargy increments per few group. Since lethargy is defined as

$$u_n = \ln E_o/E_n, \tag{B.1}$$

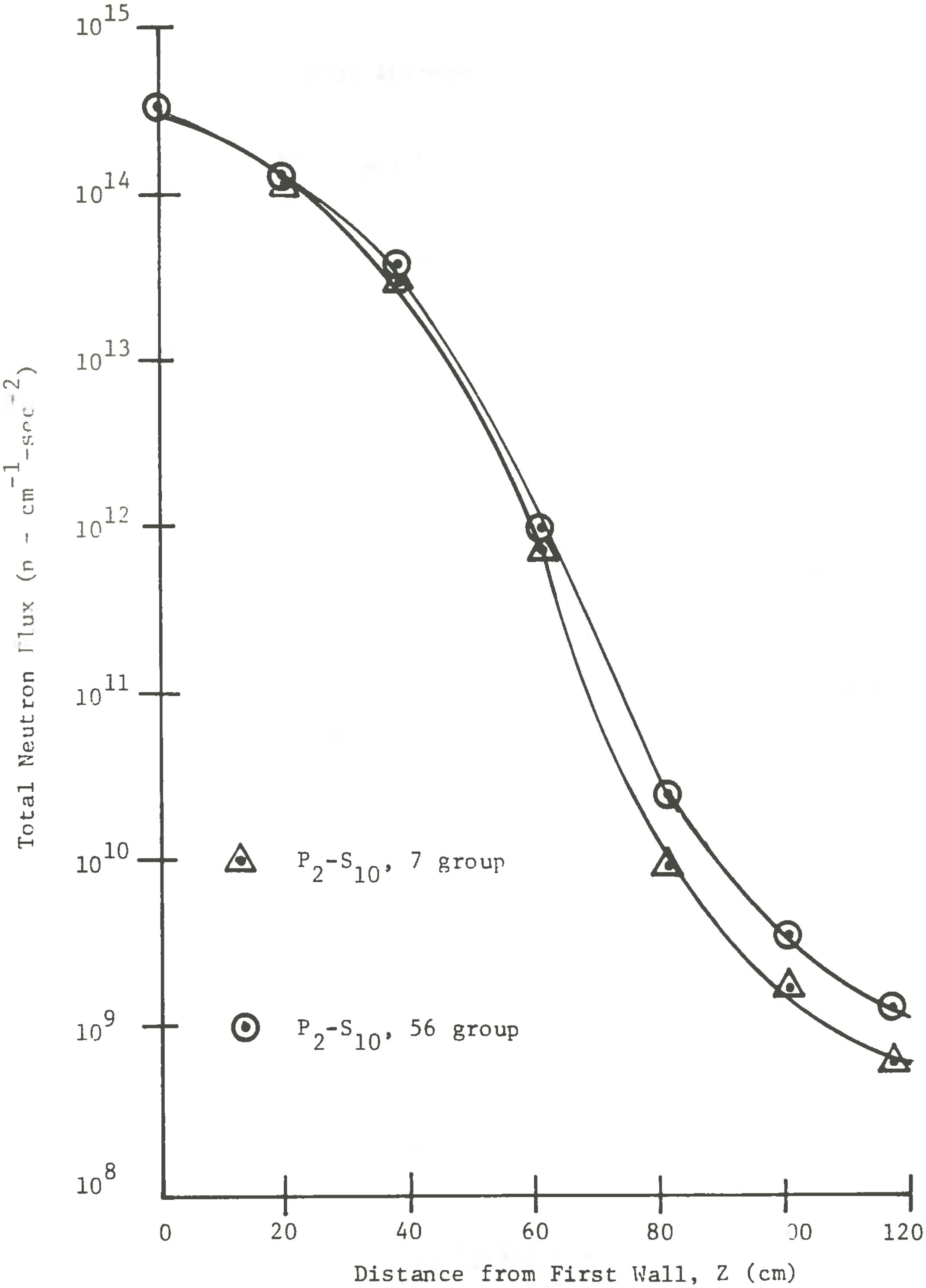

Figure B.3. Effects of cross section collapsing on ANISN total fluxes calculated for the ANL Tokamak.

it follows that the lethargy increment given by

$$\Delta u = u_{n+1} - u_n \qquad \text{(B.2)}$$

$$= \ln \frac{E_o}{E_{n+1}} - \ln \frac{E_o}{E_n}$$

can be written as

$$\Delta u = \ln \frac{E_n}{E_{n+1}} \, . \qquad \text{(B.3)}$$

In DLC-41/VITAMIN C, group 35 contains thermal neutrons. Likewise, in the collapsed cross section set, group 6 neutrons are thermals. In both cases, the thermal energy range is from 0.414 eV to 0.0001 eV. It follows that since 0.414 eV is the upper energy boundary of few group 6, it is also the lower energy boundary of group 5. Since fusion neutrons are under consideration, then the upper energy limit on the neutrons produced is 14.918 MeV. This means that from the upper limit of few group 1 to the lower limit of few group 5, the neutron energy range is 14.918 MeV $\geq E_n \geq$ 0.414 eV. Therefore, the total lethargy decrease is

$$\Delta u_{total} = \ln \frac{E_1}{E_5} \qquad \text{(B.4)}$$

$$= \ln \frac{14.918 \times 10^6}{0.414}$$

$$\Delta u_{total} = 17.4 .$$

For five energy groups, the uniform lethargy decrease is

$$\Delta u_g = \frac{\Delta u_{total}}{5} \tag{B.5}$$

$$= \frac{17.5}{5}$$

$$\Delta u_g = 3.48.$$

From Equation B.3,

$$\Delta u_g = \ln \frac{E_g}{E_{g+1}} , \tag{B.6}$$

where

E_g is the few group upper limit,

and E_{g+1} is the lower limit.

Since $$\Delta u_g = \ln \frac{E_g}{E_{g+1}} ,$$

then $$e^{\Delta u_g} = \frac{E_g}{E_{g+1}} ,$$

and $$E_{g+1} = E_g e^{-\Delta u_g} . \tag{B.7}$$

If $$\Delta u_g = 3.48,$$

then $$E_{g+1} = 0.0308\ E_g. \tag{B.8}$$

This relationship was used to develop the idealized few group boundaries shown in Table B.5a). For example, few group 1 has an upper limit of 14.918 MeV, therefore, E_1 = 14.918 MeV.

Table B.5

Energy Boundaries of Idealized and Approximated Few Groups

Group	Energy Range	Δu_g
a) Idealized Few Group Boundaries*		
1	14.918 - 0.459 MeV	3.48
2	459 - 14.137 KeV	3.48
3	14.137 - 0.435 KeV	3.48
4	435 - 13.398 eV	3.48
5	13.398 - 0.414 eV	3.48
6 (Thermals)	0.414 - 0.0001 eV	--
7 (Gammas)	14.0 - 0.010 MeV	--

Group	Multigroup	Energy Range	Δu_g
b) Multigroups per Few Group**			
1	1-7	14.918 - 0.449 MeV	3.50
2	8-23	449 - 15.034 KeV	3.397
3	24-27	15.034 - 0.454 KeV	3.50
4	28-30	454 - 10.677 eV	3.75
5	31-34	10.677 - 0.414 eV	3.25
6	35	0.414 - 0.0001 eV	--
7	36-56	14.0 - 0.01 MeV	--

* Calculated to yield constant Δu_g.

** Selected from DLC-41/VITAMIN C to approximate constant Δu_g.

From Equation B.8,

$$E_2 = 0.0308\ E_1$$
$$= 0.0308 \times 14.918 \text{ MeV}$$
$$E_2 = 0.459 \text{ MeV.}$$

In other words, an energy group which covers the range of 14.918 MeV to 459 KeV represents a group with a lethargy decrease of 3.48.

Once the ideal boundaries were found for the first five few groups, the matching of multigroups to few groups was performed (recall that few group 6 represents thermal neutrons and few group 7 represents gamma rays). Using the multigroup energy boundaries for DLC-41/VITAMIN C (see Appendix C), an attempt was made to select the appropriate number of multigroups for inclusion in each few group. The criterion was that the total energy range for each set of multigroups match as nearly as possible with the idealized few group range. The lethargy decrease for each set of multigroups was also compared to 3.48 to assess the accuracy of the selected boundaries. The following example deals with few group 1.

Few group 1 has an upper boundary of 14.918 MeV, as does multigroup 1. It also has a lower limit of 459 KeV. The closest lower boundary to this is 449 KeV for multigroup 7. Therefore, few group 1 contains multigroups 1 through 7. From the above equations, the few group has a calculated lethargy decrease of 3.50. An entire list of few group compositions is given in Table B.5b).

B.9. ANISN Summary

Since the ANISN runs were a learning process, and a time of considerable trial and error, it was decided to refrain from giving a complete listing of program inputs until the end of this Appendix. In this way, the reader will have gained a better understanding of the inputs which affect ANISN before reaching this section. The author's choices of inputs should then be clear to the reader. The ANISN run chosen for this presentation was the run of the ANL problem, using 7 groups, with the cross section data submitted on cards. This case represents the sum total of experience gained from previous ANISN runs presented in Appendix B. It is also the basis for the DOT3.5 calculations which follow in Appendix D. Table B.6 is a listing of the inputs (excluding the cross section data on the 14* array).

Table B.6

ANISN Card Image and Input Summary

```
ANL PROBLEM - ANTSN, 7GROUP, CARDS
                                              PRT ON          00
                                              15$                   7000            0            2           10            2
                                                        3              0           38          149            0            7
                                                        3              4           10            0          114            0
                                                      114              0            0            1            0            0
                                                      100              0            0            0            0            5
                                                        2              0            0            0            1            1
                                                        0
                                              16*                    0.0          0.0        .0010      1.42089      1000000
   15$ ARRAY     36 ENTRIES READ
                                                      0.0            0.0          1.0          0.0          0.5        .0010
                                                      .05          .0030          .75  T

   16* ARRAY     14 ENTRIES READ
    OT

37956 LOCATIONS WILL BE USED FOR THIS PROBLEM
 8220 LOCATIONS WILL BE USED TO READ CROSS SECTIONS
                                              14*
   14* ARRAY    7960 ENTRIES READ

    OT
                                              17*        48       1.0  F      0.0  1

   17* ARRAY    1043 ENTRIES READ

    OT
                                              3*          F       1.0  T

   3* ARRAY    1043 ENTRIES READ

    OT
                                              1*          F       1.0
                                              4*        2I0.0         1I210.0            240.0        241.014I242.0

   1* ARRAY      7 ENTRIES READ
                                                    272.0 1I273.0      9I276.0      4I291.0     25I296.0     5I361.0
                                              1I370.0     1I436.3           439.8        440.8       441.05      441.55
                                                    441.8        442.05 1I443.3              447.3        448.3       449.05
                                              1I449.8  39I451.0      4I521.0      1I529.8             531.0       531.75
                                                    532.5 1I533.5          533.5        538.75        539.0       539.25
                                                   539.75        540.           541.        544.5    545.
                                              5*          F 1.0
```

Table B.6 (continued)

```
4* ARRAY    150 ENTRIES READ
5* ARRAY      7 ENTRIES READ
6* ARRAY     35 ENTRIES READ
7* ARRAY     35 ENTRIES READ
8$ ARRAY    149 ENTRIES READ
9$ ARRAY     33 ENTRIES READ
19$ ARRAY    34 ENTRIES READ
26* ARRAY     7 ENTRIES READ
0T
```

```
6*               0.0          .033336 1N         2      .046884      .025842

1N          2    0.0          .054022      .0170996     .038422 1N         4
      .048884    .0170996     .054936      .0137132 1N        4   0.0
      .033336     .025842     .038422      .0137132      .03845 1N         5
7*               -.22695      -.14887  1M         1     -.50166      -.4334

   -.14887  1M          2     -.73376      -.67941      -.4334      -.14887
1M          3   -.9012        -.86506      -.67941      -.4334      -.14887
1M          4  -.98886        -.97391      -.86506     -.67941      -.4334
   -.14897  1M          5
8$          4R          1 2R         2            3         4155          5

            6 2R      710R           8 5R       926R       10 CF         11
2R         12 2R        13          14            15        16            17
           18           19 2R       20            21        22            23
2R       2440R          25 5R       26 2R         27        28            29
           30 2R        31          32            33        34            35
           36           37          38

9$                       1           4             7        10            13

           16           19          22            25        28            31
           34           37          40            43        46            49
           52           55          58            61        64            67
           70           73          76            79        82            85
           88           91          94            97       100           103
          106          109         112
19$            F         2

26*            F 1.0

T
```

ANL PROBLEM - ANISN, 7GROUP, CARDS

ID	PROBLEM ID NO.	7003
ISCT	ORDER OF SCATTERING	[illegible]
IGE	1/2/3 = PLA/CYL/SPH	2
IBR	RT. B.C. SAME AS LEFT B.C.,IBL	0
IM	NO. OF INTERVALS	14[illegible]
IGM	NO. OF GROUPS	7
IHS	POS. OF SIGMA GG	4
MS	MIXING TABLE LENGTH	0
MTP	NO. MATLS. FROM LIB TAPE	0
IDFM	0/1=NONE/DENSITY FACTORS(21*)	0
IQM	0/1=NONE/DIST. SOURCE	1
IPP	INTERVAL OF SHELL SOURCE	0
ID1	0/1/2/3=NO/PRNT ND/PNCH N/BOTH	0
ID3	0/N=NO/N ACT. BY ZONE	0
ICM	OUTER ITER. MAX.	5
IDAT2	0/1=NO/DIFFUSION(24$)	0
IFLU	0/1/2=BOTH/LINEAR/STEP	0
IPRT	0/1 = PRINT X-SEC/DO NOT	1
EV	EIGENVALUE GUESS	0.0
EPS	PRECISION DESIRED	1.00000E-03
DY	CYL OR PLA HEIGHT	1.00000E+06
DFM1	HT. FOR VOID CORR.	0.0
PV	IPVT=1/2 - K/ALPHA	0.0
XLAL	PT CNVRG EPS. IT .NE.0	1.00000E-03
EQL	EV CHANGE EPS.-SEARCH	1.00000E-03
ITH	0/1 = REG./ADJ.	0
ISN	QUADRATURE ORDER	12
IBL	0/1/2/3 = NO REFL/REFL/PER/WHITE	3
IZM	NO. OF ZONES	33
IEVT	0/1/2/3/4/5/6=Q/K/ALPHA/C/Z/R/H	0
IHT	POS. OF SIGMA T	3
IHM	TABLE LENGTH	10
MCR	NO. MATLS. FROM CARDS	114
MT	NO. OF MATLS.	114
IPVT	0/1/2=NONE/K/ALPHA	0
IPM	0/1/IM=NONE/S(MM,IPP)/S(MM,IM)	0
IIM	INNER ITER. MAX.	100
ID2	0/1/2=NO/X-SEC TAPE/PREV	0
ID4	0/1=NO/N ACT. BY INT.	0
IDAT1	0/1/2=NO/MIN/MAX TAPE	2
IFG	0/1=NO/FEW GRP.	0
IFN	0/1/2=INPUT 2*/3*/PREV. CASE	1
IXTR	0/1=CALC/READ P-L CONSTANTS	0
EVM	EIGENVALUE MODIFIER	0.0
BF	BUCKLING FACTOR	1.42089E+00
DZ	PLANE DEPTH	0.0
XNF	NORM. FACTOR	1.00000E+00
PTF	LAMBDA2 RELAXATION	5.00000E-01
XLAH	1-LAMBDA MAX.-SEARCH	5.00000E-02
XNPM	NEW PARAM. MOD.-SEARCH	7.50000E-01

APPENDIX C

Cross Section Preparation

C.1. DLC-41/VITAMIN C Data

Since DLC-41/VITAMIN C is the preferred cross section library for use in this thesis project, only its basic data is included. DLC-37D information is left to the reader's interest. The following tables present the lower energy boundary per multigroup (Table C.1) and the element identification numbers (Table C.2) for DLC-41/VITAMIN C elements used in the ANL problem.

C.2. TAPEMAKER

The Oak Ridge National Laboratory program, TAPEMAKER, was used to convert selected cross section data from the DLC-41/VITAMIN C library into a group independent tape. This tape was then used to supply cross-section input in the 56 group runs, as well as multigroup data for the 7 group collapses. For this reason, the inputs for this program are also included in this Appendix (Table C.3). In addition, Table C.4 presents a listing of materials with elemental composition and the atom density of each component.

The TAPEMAKER input can be deciphered as follows:

13$ array: This is the information in Table C.2. As the program selects materials by the use of DLC-41 I.D. numbers, it reassigns new element numbers based on position in the

13$ array. Therefore, P_o for H^2 (DLC-41 ID = 233) becomes element number 52.

10$ array: Based on 13$ array, there are MTP = 54 elements to be taken off DLC-41/VITAMIN C. The 10$ array contains element numbers for the mixtures being created. These numbers begin with MTP + 1 = 55, and continue through all mixtures created. When regions contain previously numbered materials, then no number is inserted in the array.

11$ array: This array contains the new element numbers, MTP = 1 through 54, as needed to create the new mixtures in 10$ array. It merely designates which elements comprise which materials. The zeros are present to initialize the P_o, P_1, and P_2 values for each material.

12$ array: This array is merely atom densities for each component element in a material. These values are also initialized. This data is listed in Table C.4.

Table C.1

Lower Boundary per Energy Group for Neutron and Gamma Rays in DLC-41/VITAMIN C

Group	Energy (eV)	Group	Neutron Lower Energy (eV)
Neutrons			
1	1.3499 (07)*	19	2.2371 (05)
2	1.2214 (07)	20	1.4996 (05)
3	1.0000 (07)	21	8.6517 (04)
4	8.1873 (06)	22	3.1828 (04)
5	6.7032 (06)	23	1.5034 (04)
6	5.4881 (06)	24	7.1018 (03)
7	4.4933 (06)	25	3.3546 (03)
8	3.6788 (06)	26	1.5846 (03)
9	3.0119 (06)	27	4.5400 (02)
10	2.4660 (06)	28	1.0130 (02)
11	2.0190 (06)	29	2.2603 (01)
12	1.6530 (06)	30	1.0677 (01)
13	1.3534 (06)	31	5.0435 (00)
14	1.1080 (06)	32	2.3824 (00)
15	9.0718 (05)	33	1.1254 (00)
16	7.4274 (05)	34	4.1400 (-01)
17	4.9787 (05)	35	1.0000 (-04)
18	3.3373 (05)		

* Upper energy for neutron group 1 is 1.4918 (07).

Table C.1 (con't)

Group	Gamma Lower Energy (eV)	Group	Gamma Lower Energy (eV)
Gamma Rays			
1	1.2 (07)*	12	3.5 (06)
2	1.0 (07)	13	3.0 (06)
3	8.0 (06)	14	2.5 (06)
4	7.5 (06)	15	2.0 (06)
5	7.0 (06)	16	1.5 (06)
6	6.5 (06)	17	1.0 (06)
7	6.0 (06)	18	4.0 (05)
8	5.5 (06)	19	2.0 (05)
9	5.0 (06)	20	1.0 (05)
10	4.5 (06)	21	1.0 (04)
11	4.0 (06)		

* Upper energy for gamma group 1 is 1.4 (07).

Table C.2

Element Identification Numbers Prepared for ANL Tokamak Using TAPEMAKER and DLC-41/VITAMIN C

1	P0	NI	CASE FOR COMBINED CTR & CRBR PROCESSIN
2	P1	NI	CASE FOR COMBINED CTR & CRBR PROCESSIN
3	P2	NI	CASE FOR COMBINED CTR & CRBR PROCESSIN
5	P0	CR	CASE FOR COMBINED CTR & CRBR PROCESSIN
6	P1	CR	CASE FOR COMBINED CTR & CRBR PROCESSIN
7	P2	CR	CASE FOR COMBINED CTR & CRBR PROCESSIN
9	P0	FE	CASE FOR REM SHIELDING PROBLEM
10	P1	FE	CASE FOR REM SHIELDING PROBLEM
11	P2	FE	CASE FOR REM SHIELDING PROBLEM
21	P0	CU	CASE FOR COMBINED CTR & CRBR PROCESSIN
22	P1	CU	CASE FOR COMBINED CTR & CRBR PROCESSIN
23	P2	CU	CASE FOR COMBINED CTR & CRBR PROCESSIN
25	P0	HE4	CASE FOR COMBINED CTR & CRBR PROCESSIN
26	P1	HE4	CASE FOR COMBINED CTR & CRBR PROCESSIN
27	P2	HE4	CASE FOR COMBINED CTR & CRBR PROCESSIN
29	P0	C-12	CASE FOR COMBINED CTR & CRBR PROCESSING
30	P1	C-12	CASE FOR COMBINED CTR & CRBR PROCESSING
31	P2	C-12	CASE FOR COMBINED CTR & CRBR PROCESSING
33	P0	O-16	CASE FOR COMBINED CTR & CRBR PROCESSIN
34	P1	O-16	CASE FOR COMBINED CTR & CRBR PROCESSIN
35	P2	O-16	CASE FOR COMBINED CTR & CRBR PROCESSIN
37	P0	AL-27	CASE FOR COMBINED CTR & CRBR PROCESSIN
38	P1	AL-27	CASE FOR COMBINED CTR & CRBR PROCESSIN
39	P2	AL-27	CASE FOR COMBINED CTR & CRBR PROCESSIN
41	P0	PB	CASE FOR COMBINED CTR & CRBR PROCESSIN
42	P1	PB	CASE FOR COMBINED CTR & CRBR PROCESSIN
43	P2	PB	CASE FOR COMBINED CTR & CRBR PROCESSIN
53	P0	B-10	CASE FOR COMBINED CTR & CRBR PROCESSIN
54	P1	B-10	CASE FOR COMBINED CTR & CRBR PROCESSIN
55	P2	B-10	CASE FOR COMBINED CTR & CRBR PROCESSIN
57	P0	H-1	CHECK CASE FOR COMBINED LIBRARY PROCESSI
58	P1	H-1	CHECK CASE FOR COMBINED LIBRARY PROCESSI
59	P2	H-1	CHECK CASE FOR COMBINED LIBRARY PROCESSI
73	P0	B-11	CASE FOR COMBINED CTR & CRBR PROCESSIN
74	P1	B-11	CASE FOR COMBINED CTR & CRBR PROCESSIN
75	P2	B-11	CASE FOR COMBINED CTR & CRBR PROCESSIN
77	P0	TI	CASE FOR COMBINED CTR & CRBR PROCESSIN
78	P1	TI	CASE FOR COMBINED CTR & CRBR PROCESSIN
79	P2	TI	CASE FOR COMBINED CTR & CRBR PROCESSIN
101	P0	N-14	CASE FOR COMBINED CTR & CRBR PROCESSIN
102	P1	N-14	CASE FOR COMBINED CTR & CRBR PROCESSIN
103	P2	N-14	CASE FOR COMBINED CTR & CRBR PROCESSIN
105	P0	MO	CASE FOR COMBINED CTR & CRBR PROCESSIN
106	P1	MO	CASE FOR COMBINED CTR & CRBR PROCESSIN
107	P2	MO	CASE FOR COMBINED CTR & CRBR PROCESSIN
137	P0	NB-93	CASE FOR COMBINED CTR & CRBR PROCESSIN
138	P1	NB-93	CASE FOR COMBINED CTR & CRBR PROCESSIN
139	P2	NB-93	CASE FOR COMBINED CTR & CRBR PROCESSIN
197	P0	H3	CASE FOR COMBINED CTR & CRBR PROCESSIN
198	P1	H3	CASE FOR COMBINED CTR & CRBR PROCESSIN
199	P2	H3	CASE FOR COMBINED CTR & CRBR PROCESSIN
233	P0	H-2	CASE FOR COMBINED CTR & CRBR PROCESSIN
234	P1	H-2	CASE FOR COMBINED CTR & CRBR PROCESSIN
235	P2	H-2	CASE FOR COMBINED CTR & CRBR PROCESSIN

Table C.3

TAPEMAKER Card Image for ANL Tokamak Modeling

```
    *    *    *    *    *    *    CARD IMAGE OF INPUT SUBMITTED    *    *    *    *

CARD COLUMNS
             1         2         3         4         5         6         7         8
    12345678901234567890123456789012345678901234567890123456789012345678901234567890    CARD COLUMNS
CARD NO.
 1        150000
 2      56     3     4    59   159     0    54    36     0     0
 3  10$          1I55.0             57.1 3Q          3Q          1I58.0
 4          60.1 3C          1I61.0             63.1 3Q          3Q                 3
 5   3C          3C          3C          1I64.0             66.1 3Q                 4
 6   3C          3Q          3Q          3Q          3Q          3C                 5
 7   1I67.C             69.1 3Q          3C          3C          1I70.0             6
 8          72.1 3C          3C          3Q          3Q          3Q                 7
 9   3C          1I73.0             75.1 3Q          1I76.0             78.1        8
10   3C          1I79.0             81.1 3Q          3Q          3Q                 9
11   1I82.0             84.1 3Q          3Q          1I85.0             87.1       10
12   3C          3Q          3Q          3Q          3Q          3Q                11
13   3C          3C          3Q          1I88.0             90.1 3Q                12
14  11$          3R        0 4I49.0             54.1 3B        0 1I17.0            13
15           9.1 3B        0 7I1.0               9.1 1I16.0             18.1       14
16   1I43.0             45.1 3R        0 7I1.0               9.1 4I16.0            15
17          21.1 1I31.0             33.1 1I43.0             45.1 3R        0       16
18   1I16.0             18.1 1I28.0             30.1 1I34.0             36.1       17
19   3B        0 4I16.C             21.110I25.0             36.1 3R        0       18
20   1I22.0             24.1 3R        0 1I40.0             42.1 3R        0       19
21   4I16.0             21.1 1I31.0             33.1 3R        0 4I19.0            20
22          24.1 3R        016I1.0              18.1 1I37.0             39.1       21
23   4I43.0             48.1 3R        0 1I13.0             15.1                   22
24  12*          3B    0.0   6B   1.0-10 3R    0.0   3R   5.0-13 3R    0.0         23
25   3B   .01004 3B   .01499 3R   .05805 3R    8.0-5 3B    .0016 3R 0.0            24
26   3B    .0031 3R    .0047 3B    .0182 3R    2.5-5 3R     .023 3R     .046       25
27   3B    5.0-4 3B    0.0   3R   .07943 3B    2.5-4 3R   .00103 3R 0.0            26
28   3R     .019 3R     .003 3R     .005 3R    .0014 3R     .036 3B    .0056       27
29   3B    0.0   3B   .06024 3R    0.0   3R   .03347 3R    0.0   3R     .066       28
30   3B    .0132 3R     .198 3R    0.0   3R    .0654 3R    .0436 3R 0.0            29
31   3F    .0044 3R    .0066 3R    .0255 3R    .0348 3B   .00402 3R    3.5-4       30
32   3B    8.5-4 3R    .0C07 3R    8.3-4 3R    0.0   3R    .0168                   31
33  13$          1I1.0               3.1 1I5.0               7.1 1I9.0             32
34          11.1 1I21.C             23.1 1I25.0             27.1 1I29.0            33
35          31.1 1I33.0             35.1 1I37.0             39.1 1I41.0            34
36          43.1 1I53.0             55.1 1I57.0             59.1 1I73.0            35
37          75.1 1I77.0             79.1 1I101.0           103.1 1I105.0           36
38         107.1 1I137.0           139.1 1I197.0           199.1 1I233.0           37
39         235.1  T
```

Table C.4

Material Compositions for ANL Tokamak Modeling

Material	Elemental Data: Composition	Elemental Data: Atom Density (atoms-barn^{-1}-cm^{-1})
Plasma	50% D	1.0 (-10)
	50% T	1.0 (-10)
Vacuum	100% Fe (sputtered 1st wall material)	5.0 (-13)
Type 316 SS	68.4% Fe	0.05805
	18.0% Cr	0.01499
	11.0% Ni	0.01004
	2.5% Mo	0.00160
	0.1% C	0.00008
SS + H_2O coolant	31.3% 316 SS	
	Fe	0.0182
	Cr	0.0047
	Ni	0.0031
	Mo	5.0 (-04)
	C	2.5 (-05)
	68.7% H_2O	
	H	0.046
	O	0.023
Graphite + 1% Boron	99% C	0.07943
	1% B (natural)	
	B^{10}	0.00025
	B^{11}	0.00103
Lead Mortar (2.5 g/cm^3)	2.4 wt. % H	0.036
	3.3 wt. % O	0.003
	5.0 wt. % B (natural)	
	B^{10}	0.0014
	B^{11}	0.0056
	15.2 wt. % C	0.019
	73.6 wt. % Pb	0.005
	0.5 wt. % Miscellaneous	0.0

Table C.4 (con't)

Material	Elemental Data: Composition	Atom Density (atoms-barn^{-1}-cm^{-1})
Aluminum	100% Al^{27}	0.06024
Liquid nitrogen	100% N^{14}	0.03347
Epoxy ($C_{10}H_{30}O_2$)	C	0.066
	H	0.198
	O	0.0132
Alumina (Al_2O_3)	Al	0.0654
	O	0.0436
Toroidal Field Coils	44% 316 SS	
	Fe	0.0255
	Cr	0.0066
	Ni	0.0044
	Mo	0.0007
	C	3.5 (-04)
	41% Cu	0.0348
	3% Nb Ti	
	Nb	0.00083
	Ti	0.00085
	12% He (liquid)	0.00402
Helium Bath (50% liquid-50% gas)	100% He	0.0168

APPENDIX D

DOT3.5 Test Runs

D.1. Program Input Data

Considering the body of information included in the preceding sections, explanatory information on the DOT3.5 program inputs can be kept to a minimum. Table D.1 includes variable names, definitions, and selected values based on the ANL problem. These include arrays 61$, 62$, and 63*. In addition, the table also contains data for the following arrays:

7* - Angular Quadrature Direction Cosines (mu and eta)

6* - Angular Quadrature Weights

17* - Fixed Volume, Distributed Source Terms (per group)

31$ - Order of Scatter (per group)

3* - Initial Flux Guess

1* - Fission Spectrum

2* - Axial (Z) Interval Boundaries

4* - Radial (R) Interval Boundaries

5* - Velocities

8$ - Zone Number by Interval

9$ - Materials by Zone

29$ - Order of Angular Quadrature (per group)

Cross section data read from cards in the 14* array has not been reproduced here.

Table D.1

DOT3.5 Inputs for ANL Tokamak Modeling

```
ANL PROBLEM 1--7 GROUP--85CM DUCT

 A02 =     0        0/1 = FORWARD/ADJOINT CALCULATION
 A03 =     2        MAXIMUM ORDER OF SCATTERING
 IZM =    38        NUMBER OF MATERIAL ZONES
  IM =     6        NUMBER OF RADIAL INTERVALS
  JM =   149        NUMBER OF AXIAL  INTERVALS

 IGM =     7        NUMBER OF ENERGY GROUPS
 IHT =     3        POSITION OF TOTAL CROSS SECTION
 IHS =     4        POSITION OF SELF-SCATTER CROSS SECTION
 ITL =    10        CROSS SECTION TABLE LENGTH PER GROUP
 M01 =     0        MIXING TABLE LENGTH

 MCR =   114        NUMBER OF MATERIALS FROM CARDS
 MTP =     0        NUMBER OF MATERIALS FROM NLIB
  MT =   114        TOTAL NUMBER OF MATERIALS
 IP5 =     0        0/1 = FLUXES AND MOMENTS IN CORE/STORED EXTERNALLY
 A04 =    16        MAXIMUM NUMBER OF ANGLES IN ANGULAR QUADRATURE

 IGE =     1        0/1/2 = X-Y/R-Z/R-THETA GEOMETRY
 B01 =     1        LEFT BOUNDARY CONDITION, 0/1/2/4/6 = VACUUM/REFLECTED/PERIODIC/BOUNDARY SOURCE(CARDS)/BOUNDARY SOURCE(TAPE)
 B02 =     1        RIGHT BOUNDARY CONDITION, 0/1/2/3/4/5/6 = 0,1,2,4,6 SAME AS FOR B01, 3/WHITE, 5/ALBEDO
 B04 =     1        BOTTOM BOUNDARY CONDITION, SAME AS FOR B02
 B03 =     0        TOP BOUNDARY CONDITION, SAME AS FOR B02

 D05 =     1        OUTER ITERATION MAXIMUM
 S04 =    20        INITIAL INNER ITERATION MAXIMUM, USED UNTIL ABS(LAMBDA-1.0).LT.10*EPS
 G07 =   100        INNER ITERATION MAXIMUM PER GROUP (IF NEGATIVE, LIMIT IS IN 28$ ARRAY)
 FIT =     0        0/1/2/3/4 = MIXED/LINEAR/STEP/WEIGHTED/MIXED LINEAR WEIGHTED
 I04 =     0        0/1/2/3/4/5/6/-6 = Q/K/ALPHA/C/Z/BNDRY SRC/USE 1ST COLL SRC ON NPSO/CALC ANALYTIC 1ST COLL SRC, WRITE ON NPSO

 IP1 =     2        0/1/2  = REGULAR SCALING/OVER-RELAXATION/SPACE DEPENDENT
 S02 =     0        0/1/2 = NO PARAMETRIC EIGENVALUE SEARCH/K/ALPHA
  IZ =     0        NUMBER OF RADIAL ZONES FOR ZONE THICKNESS SEARCH
  JZ =     0        NUMBER OF AXIAL  ZONES FOR ZONE THICKNESS SEARCH
 IZC =     0        0/N = NO EFFECT/ENTER N ZONE NUMBERS IN 32$ ARRAY FOR ZONES OF CONVERGENCE

 IPA =     1        0/1 = NO EFFECT/ENTER ORDER OF SCATTER PER GROUP BY GROUP IN 31$ ARRAY
 ISC =     1        0/1 = NO EFFECT/ENTER NUMBER OF QUADRATURE ANGLES PER GROUP BY GROUP IN 29$ ARRAY, ZERO FOR DIFFUSION THEORY
 IZ3 =     0        0/N = NO EFFECT/ENTER N NUMBERS IN 33* AND 34* ARRAYS, ANGULAR DISTRIBUTION OF POINT SOURCE FOR I04=-6
 M07 =     0        FLUX INPUT, 0/1/2/3/4/5 = A(G)/N(I,J)*G/A(G)*N(I,J)/A(G)*B(I)*C(J)/(B(I)*C(J))*G/FLUX GUESS ON NFLUX1
 M06 =     1        DISTRIBUTED SOURCE INPUT, SAME AS M07, EXCEPT            5=SOURCE ON LOGICAL UNIT NBSC

 IZ1 =     0        -N/N = INTERIOR BOUNDARY SOURCE AT RADIAL BOUNDARY N INPUT FROM TAPE/CARDS
 IZ2 =     0        -N/N = INTERIOR BOUNDARY SOURCE AT AXIAL BOUNDARY N INPUT FROM TAPE/CARDS
 IB5 =     0        -N/N = ANGULAR FLUX LEFT/RIGHT AT RADIAL BOUNDARY N WRITTEN ON NBFT BY GROUP
 IB6 =     0        -N/N = ANGULAR FLUX DOWN/UP AT AXIAL BOUNDARY N WRITTEN ON NBFT BY GROUP
 IZ4 =     0        0/N = NO EFFECT/FINAL TOTAL SCATTERING SOURCE WRITTEN ON N BY GROUP

 IB2 =     1        0/1/2/3 = NO EFFECT/NO X-S PRINT/NO FLUX PRINT/BOTH
 M05 =     0        -N/N = CALCULATE N ZONEWISE ACTIVITIES/N ZONE AND POINT ACTIVITIES
 IB1 =     0        0/N = NO EFFECT/ENTER N ZONE NUMBERS IN 30$ ARRAY FOR ZONE BALANCE TABLES
 IP3 =     0        0/1 = NO EFFECT/PUNCH FISSION DISTRIBUTION
IAPT =     0        0/1/2/3 = NO ANGULAR FLUX OUTPUT/WRITE ON LOG NAFT/PRINT/BOTH

 IP4 =     0        0/1 = NO EFFEC /ANG    F U    O    TRA OUT     RAT
 IS2 =     0        SPARE
 IS3 =     0        SPARE
```

Table D.1 (continued)

```
  IZ5 =     8          MINIMUM SPS ITERATIONS (0 DEFAULT = 8)
  IZ6 =   100          MAXIMUM SPS ITERATIONS (0 DEFAULT = 100)

  IMG =     2          NUMBER OF INNER ITERATIONS BEFORE SPACE-POINT RESCALING
  IP2 =     1          NUMBER OF INNER ITERATIONS BETWEEN SUCCESSIVE SPACE-POINT RESCALINGS
  IB3 =     4          DAMPING CONSTANT FOR SPACE-POINT RESCALINGS
  ITI =     0          SPARE
IFLUX=      0          0/INN = NO EFFECT/PREPARE A FLUX GUESS FROM LOGICAL UNIT NN AS SPECIFIED BY I, WRITE ON NFLUX1

  IGMI=     0          NUMBER OF GROUPS FOR FLUX GUESS INPUT
 IA03I=     0          ORDER OF SCATTER FOR FLUX GUESS INPUT
 IA04I=     0          NUMBER OF ANGLES FOR FLUX GUESS INPUT
 ISRCE=     0          0/N = NO EFFECT/COPY FIXED SOURCE FROM LOGICAL UNIT N TO NBSO FOR I04 = 5, TO NPSO FOR I04 = 6
 IGIXS=     0          0/N = NO EFFECT/COPY GROUP - ORGANIZED CROSS-SECTION TAPE FROM LOGICAL UNIT N TO NCB1

  IPRT=     0          0/1/2 = NO PRINT/PRINT UNCOLLIDED FLUX, MUS AND ETAS/AS 1 + PRINT FIRST COLLISION SOURCE

   NCB1        16      DATA SET REF NO., SCRATCH (0 DEFAULT = 2)
 NFLUX1        17      DATA SET REF NO., SCRATCH (0 DEFAULT = 3)
 NSCRAT        18      DATA SET REF NO., SCRATCH (0 DEFAULT = 4)
   NBSO        16      DATA SET REF NO., BOUNDARY OR VOLUME-DIST. SOURCE INPUT (0 DEFAULT = 14)
   NPSO        16      DATA SET REF NO., FIRST COLLISION SOURCE INPUT (0 DEFAULT = 15)

  NFLSV        18      DATA SET REF NO., SCALAR FLUX AND MOMENTS OUTPUT (0 DEFAULT = 9)
   NAFT        16      DATA SET REF NO., ANGULAR FLUX OUTPUT (0 DEFAULT = 10)
   NBFT        15      DATA SET REF NO., INTERIOR BOUNDARY ANGULAR FLUX OUTPUT (0 DEFAULT = 11)
   NGAM        17      DATA SET REF NO., ACTIVITY OUTPUT (0 DEFAULT = 12)
   NZBT         3      DATA SET REF NO., SCRATCH FOR ZONE BALANCE TABLES (0 DEFAULT = 13)

   NLIB         8      CROSS SECTION LIBRARY UNIT NUMBER
   NBUF       120      NUMBER OF K-BYTES ALLOWED FOR BUFFER AREA
   JBRL         0      0/N = NO EFFECT/LOWER AXIAL INTERVAL FOR ANGULAR FLUX OUTPUT
   JBRU         0      0/N = NO EFFECT/UPPER AXIAL INTERVAL FOR ANGULAR FLUX OUTPUT

  S01 = 0.10000E+01    SOURCE NORMALIZATION FACTOR
  EPS = 0.10000E-02    GENERAL CONVERGENCE CRITERION(INTEGRAL INNER ITERATION, LAMBDA AND FISSION DENSITY)
  G06 = 0.0            POINTWISE FLUX ERROR CRITERION (INTEGRAL INNER ITERATION TEST USED IF G06=0.0)
  G05 = 0.10000E+04    MAXIMUM CPU TIME FOR THIS PROBLEM
  S03 = 0.0            PARAMETRIC EIGENVALUE FOR SEARCH (K OR ALPHA)

   EV = 0.0            FIRST EIGENVALUE GUESS
  EVM = 0.0            EIGENVALUE INCREMENT TO BE ADDED TO EV
  LAL = 0.0            LINEAR EXTRAPOLATION USED WHEN CONVERGED CLOSER THAN LAL
 EPSA = 0.0            CONVERGENCE CRITERION FOR CHANGING EV IN SEARCH
  LAM = 0.0            UPPER LIMIT ON ABS(LAMBDA-1.0) IN LINEAR SEARCH, R.V. = 0.05

  POD = 0.0            PARAMETER OSCILLATION DAMPER, R.V. = 0.75
   SH = 0.0            HEIGHT OF POINT SOURCE
  HSA = 0.0            COSINE OF ANGLE WITH Z AXIS  INTO WHICH SOURCE IS EMITTED
   SF = 0.0            SOURCE MAGNITUDE
 ZBIC = 0.0            EXCLUDED RADIUS

  ORF = 0.0            SPARE
  SPR = 0.0            SPARE
  SPE = 0.10000E-03    SPACE-POINT RESCALING CONVERGENCE CRITERION (0 DEFAULT = 1.E-4)
```

Table D.1 (continued)

```
****** DOT 3.5 (ORNL 28 FEB 77) ******
THIS CODE SHOULD ALWAYS BE REFERRED TO BY THE DESIGNATION ABOVE.
FOR REPRODUCIBLE RESULTS IT IS ESSENTIAL TO USE QUALITY-ASSURANCE DATA SETS.
                                          PRT ON        00
                                          61$                   0        2        38        6       149
                                                      7         3        4        10        0       114
                                                      0       114        0        16        1         1
                                                      1         1        0         1       20       100
                                                      0         0        2         0        0         0
                                                      0         1        1         0        0         1
                                                      0         0        0         0        0         1
                                                      0         0        0         0        0         0
                                                      0         8      100         2        1         4
                                                      0         0        0         0        0         0
                                                      0         0
                                          62$                  16       17        18       16        16
   61$ ARRAY     61 ENTRIES READ
                                                     18        16       15        17        3         8
                                                    120         0        0
                                          63*                 1.0     .001     0.0    1000.13R      0.0
   62$ ARRAY     14 ENTRIES READ
                                                  .0001  T
   63* ARRAY     18 ENTRIES READ
    0T
ARRAY ORDER -->  /61$,62$,63*/7*/6*/64$,65*,66*/13$,14*/17*/18*/15*/31$/3*/OTHER/
                                          7*            -0.44261   -0.881920   -0.33333  M         2   -0.4714
                                              -0.33333  M      1  Q         8 5R -0.33333 3R -0.88192 5R  0.33333
                                          3R   0.88192  T
   7* ARRAY      32 ENTRIES READ
   0T                                     6*           0.0 4R  0.08333      0.0 2R  0.08333  Q        8
                                            T
   6* ARRAY      16 ENTRIES READ
   0T
PROBLEM REQUIRES   65099 LOCATIONS FOR COMPUTATION, VS. AVAILABLE  470016
PROBLEM REQUIRES    9169 LOCATIONS FOR CROSS SECTION INPUT, VS. AVAILABLE  470016
                                          14*
```

Table D.1 (continued)

```
14* ARRAY   7980 ENTRIES READ
 0T                                  17*        240  1.0     F  0.5     1

17* ARRAY    894 ENTRIES READ
 0T                                  17*         F C.0       T

17* ARRAY    894 ENTRIES READ
 0T                                  17*         F C.0       T

17* ARRAY    894 ENTRIES READ
 0T                                  17*         F C.0       T

17* ARRAY    894 ENTRIES READ
 0T                                  17*         F 0.0       T

17* ARRAY    894 ENTRIES READ
 0T                                  17*         F 0.0       T

17* ARRAY    894 ENTRIES READ
 0T                                  17*         F C.0       T

17* ARRAY    894 ENTRIES READ
 0T                                  31*         F        2  T

31* ARRAY      7 ENTRIES READ
 0T                                   3*         F      1.0  T

 3* ARRAY      7 ENTRIES READ
 0T                                   1*         F C.0
                                      2*        210.0    11210.0         240.0      241.0141242.0
 1* ARRAY      7 ENTRIES READ
```

Table D.1 (continued)

```
                                      272.0 11273.0     91276.0     41291.0    251296.0     51361.0
                                 11370.0    11436.3        439.8       440.8      441.05      441.55
                                      441.8     442.05 11442.3         447.3      446.3       449.05
                                 11449.0  391451.0    11451.0     11529.0         531.0       531.75
                                      532.5 11533.5        538.5      538.75      539.0       539.25
                                      539.75       540.       541.      544.5     545.
                                 4*                0.0        42.5       43.5        46.5      150.0
 2* ARRAY    150 ENTRIES READ
                                      155.0   200.
                                 5*          5 1.0
 4* ARRAY      7 ENTRIES READ
                                 8$12481 14R2 4R3 2R2 3 3R4 2R2 3 3R5 14Q6 2R2 3 3R6 2R2 3 3R7 2R2 3 3R7
 5* ARRAY      7 ENTRIES READ
                                 2R2 3 3R8 9Q6 2R2 3 3R9 4Q6 2R2 3 3R10 25Q6 2R2 3 3R11 5Q6 2R2 3 2R2 12
                                 1Q6 2R2 3 2R2 13 1Q6 2R2 3 2R2 14 2R2 3 2R2 15 2R2 3 2R2 16 2R2 3 2R2 17
                                  2R2 3 2R2 18 2R2 3 2R2 19 2R2 3 2R2 20 1Q6 2R2 3 2R2 21 2R2 3 2R2 22
                                 2R2 3 2R2 23 2R2 3 2R2 24 1Q6 2R2 3 2R2 25 39Q6 2R2 3 2R2 26 4Q6 2R2 3
                                 2R2 27 1Q6 2R2 3 2R2 28 2R2 3 2R2 29 2R2 3 2R2 30 2R2 3 2R2 31 1Q6 2R2 3
                                  2R2 32 2R2 3 2R2 33 2R2 3 2R2 34 2R2 3 2R2 35 2R2 3 2R2 36 2R2 3 2R2 37
                                  2R2 3 2R2 38
                                  9$                  -1          -4          -7         -10         -13
 8$ ARRAY    894 ENTRIES READ
                                         -16         -19         -22         -25         -28         -31
                                         -34         -37         -40         -43         -46         -49
                                         -52         -55         -58         -61         -64         -67
                                         -70         -73         -76         -79         -82         -85
                                         -88         -91         -94         -97        -100        -103
                                        -106        -109        -112
                                 29$           E       16   T           T
 9$ ARRAY     38 ENTRIES READ
29$ ARRAY      7 ENTRIES READ
 0T
```

D.2. Calculation Tests

Detailed parametric analyses of DOT3.5 were not performed, since it was assumed that the impacts of variations on the inputs would be similar to the impacts illustrated for ANISN in Appendix B. Only two analyses were performed, one of calculation methods and the other of radial interval number.

The calculation methods tested were of two forms: the mixed linear-step method and the mixed linear-weighted method. The first method uses linear difference equations and step equations to recompute fluxes if they become negative. According to the DOT3.5 manual, negative fluxes can result from the use of linear difference equations in regions of high σ^T. The other method uses weighted difference equations to correct negative fluxes. According to the manual, this may be more accurate than the first method.

Table D.2 provides a comparison of these two methods using non-normalized total fluxes. As can be seen, the difference between them was not significant for this problem. Also, the CPU time expended was similar. Elapsed time was more than doubled for the linear-weighted method, however, that factor can be subject to other impacts, and was not used as a mode of comparison. A purely subjective choice was made to use the linear-step technique.

The other column in Table D.2 illustrates the effect of the selection of an inner iteration convergence test. From the DOT3.5 manual, the value of variable GØ6 determines which test is used. If GØ6 is set equal to zero, then the regions are subjected to an

Table D.2

Comparison of the Effects of DOT3.5 Calculation Methods on CPU Time and Total Flux

Method		Mixed Linear-Step		Mixed Linear-Weighted
FXT		0		4
GØ6		0.0	0.001	0.001
CPU Time (minutes)		4.33	8.08	8.16
Total Flux at (4,59)* per Group	1	1.753 (-08)	1.753 (-08)	1.607 (-08)
	2	4.561 (-08)	4.571 (-08)	4.637 (-08)
	3	2.258 (-08)	2.267 (-08)	2.310 (-08)
	4	1.956 (-08)	1.965 (-08)	2.007 (-08)
	5	5.576 (-09)	5.600 (-09)	5.719 (-09)
	6	2.247 (-10)	2.257 (-10)	2.339 (-10)
	7	8.687 (-08)	8.716 (-08)	8.766 (-08)

* Fluxes are not normalized to first wall loading.

integral iteration test of convergence, such that

$$\frac{1}{V}\int \left| \frac{\phi^{n}(\bar{r}) - \phi^{n-1}(\bar{r})}{\phi^{n}(\bar{r})} \right| d\bar{r} \leq \text{EPS},$$

where $\phi^{n}(\bar{r})$ and $\phi^{n-1}(\bar{r})$ are the fluxes in question, V is the volume of the system,

and EPS is the convergence criterion.

For GØ6 not equal to zero, then a pointwise scalar flux criterion is used. Therefore,

$$\text{MAX}\left\{ \left| \frac{\phi^{n}(\bar{r}) - \phi^{n-1}(\bar{r})}{\phi^{n}(\bar{r})} \right| \right\} \leq \text{G}\emptyset 6.$$

No substantial difference exists in the flux results for GØ6 values of 0.0 and 0.001, when used with the linear-step technique. However, the CPU time requirement for the integral iteration test is only about half that of the pointwise scalar flux criterion. This rendered the integral iteration test as the preferred technique for convergence in the problems involved.

D.3. <u>Interval Tests</u>

As shown in Appendix B, ANISN accuracy was greatly affected by the number of intervals chosen in the modeling of a problem. It was found in the ANISN calculations of the ANL problem that 149 intervals sufficed for an accurate representation. Therefore, 149 intervals were used in the Z-direction against three different numbers of intervals in the R-direction. Figure D.1 demonstrates the difference between these mesh configurations (6 x 149, 20 x 149, and 35 x 149) along a line 5 cm from the duct.

It will be recalled that a comparison between the 35 interval total flux and the ANL results was provided in Chapter 3. It illustrated good correlation between the two fluxes. Considering this, the results in Figure D.1 reconfirm the ANISN determination that the finer the mesh spacing becomes, the more accurate the final solution will be.

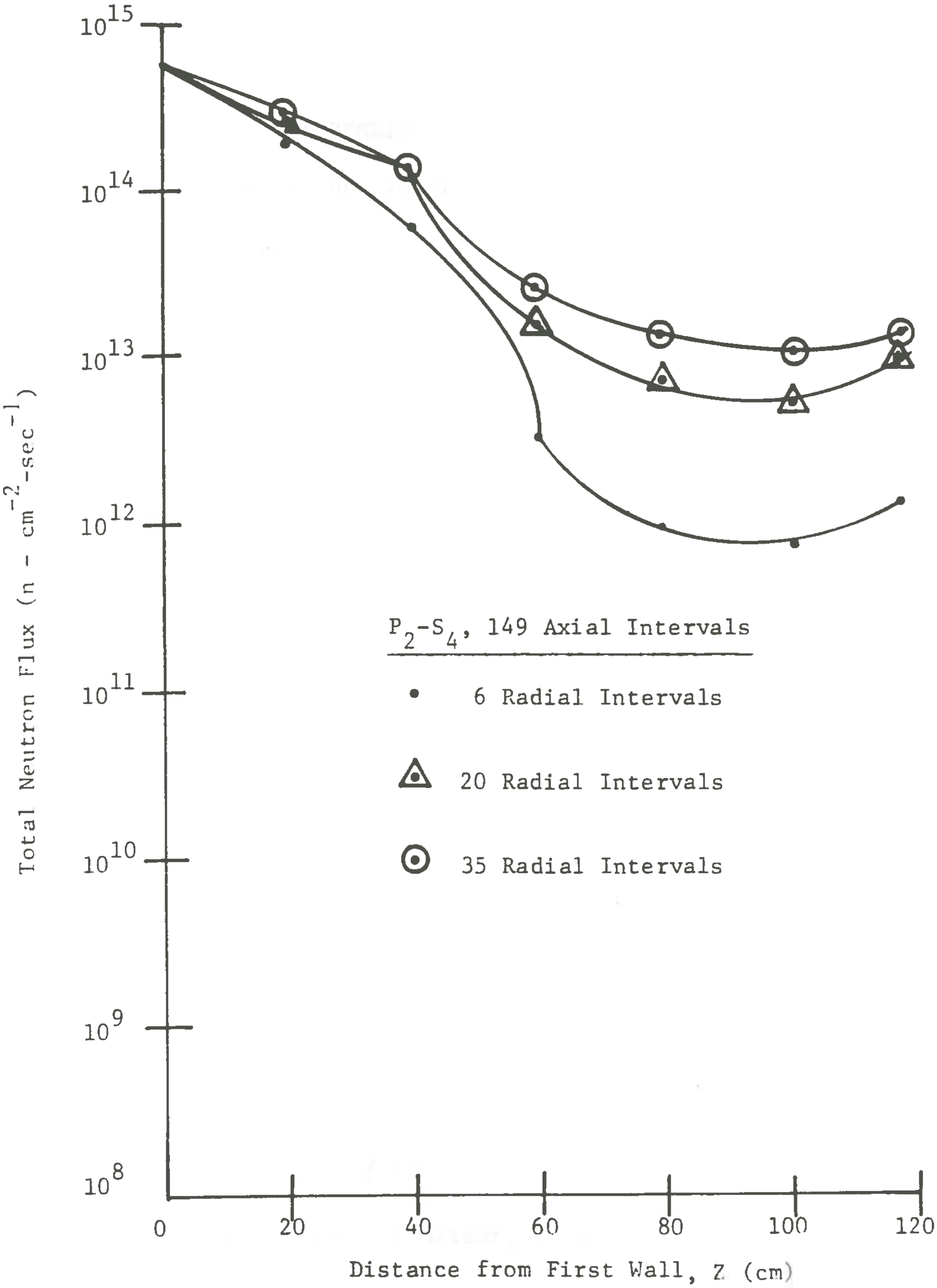

Figure D.1. Effects of radial interval number variations on DOT3.5 total fluxes calculated for the ANL Tokamak.

APPENDIX E

Duct Representation Techniques

For a cylindrical duct of diameter, d = 2a, the uncollided flux at z is given by

$$\phi_u(z) = \frac{N_o}{2} \ln \left[1 + \frac{a^2}{z^2}\right], \tag{E.1}$$

for an isotropic source of strength N_o.

For z >> a, the uncollided flux can be approximated by

$$\phi_u(z) \simeq \frac{N_o A}{2\pi z^2}, \tag{E.2}$$

where $$A = \pi a^2.$$

Therefore,

$$\phi_u(z) \simeq \frac{N_o a^2}{2 z^2}$$

and $$\left.\frac{\phi_u(z)}{N_o}\right)_{cyl.} \simeq \frac{a^2}{2 z^2}. \tag{E.3}$$

For a rectangular duct of height, H, and width, W,

$$\phi_u(z) = \frac{2\phi_o}{\pi} \tan^{-1} \frac{ab}{\sqrt{1 + a^2 + b^2}}, \tag{E.4}$$

where $$a = \frac{H/2}{z}$$

and $$b = \frac{W/2}{z}\ .$$

For a square duct,

$$s = H = W$$

so, $$a = b = \frac{s}{2z}.$$

Therefore, $$\phi_u(z) = \frac{2\phi_o}{\pi} \tan^{-1} \frac{s^2}{2z\sqrt{4z^2 + 2s^2}} \qquad (E.5)$$

For $z >> s$, Equation E.5 can be approximated as

$$\phi_u(z) \simeq \frac{2\phi_o}{\pi} \tan^{-1} \frac{s^2}{4z^2}$$

$$\simeq \frac{2\phi_o}{\pi} \cdot \frac{s^2}{4z^2}$$

$$\phi_u(z) \simeq \frac{\phi_o s^2}{2\pi z^2}\ .$$

Therefore, $$\left.\frac{\phi_u(z)}{\phi_o}\right)_{sq.} \simeq \frac{s^2}{2\pi z^2}\ . \qquad (E.6)$$

For a duct of either shape, as duct length increases ($z \rightarrow \infty$), then shape becomes irrelevant. So, for $z >> a$ and $z >> s$. then the area of the square duct will be approximately equal to the area of the cylindrical duct. This can be written

$$s^2 \simeq \frac{\pi}{4} d^2$$

$$\simeq \pi a^2 .$$

Therefore, $$\frac{s^2}{\pi} \simeq a^2 . \tag{E.7}$$

Multiplying both sides of Equation E.7 by $1/2z^2$ yields

$$\frac{s^2}{2\pi z^2} \simeq \frac{a^2}{2z^2} .$$

From Equation E.3 and E.6 this means that

$$\left.\frac{\phi_u(z)}{\phi_o}\right)_{sq.} \simeq \left.\frac{\phi_u(z)}{N_o}\right)_{cyl.} . \tag{E.8}$$

Furthermore, since $\phi_u(z)$ for square and cylindrical ducts become indistinguishable as $z \to \infty$, then

$$\phi_o \simeq N_o .$$

If it is assumed that the relation between the fluxes for cylindrical and square ducts is equivalent for all values of z, then

$$\left.\frac{\phi_u(z)}{\phi_o}\right)_{sq.} = \left.\frac{\phi_u(z)}{N_o}\right)_{cyl.} , \tag{E.9}$$

or $$\frac{2}{\pi} \tan^{-1} \frac{s^2}{2z\sqrt{4z^2 + 2s^2}} = \frac{1}{2} \ln \left[1 + \frac{a^2}{z^2}\right]. \tag{E.10}$$

This equation can be rewritten

$$\theta = \frac{\pi}{4} \ln x, \qquad (E.11)$$

where

$$\theta = \tan^{-1} \frac{s^2}{2z\sqrt{4z^2 + 2s^2}},$$

and

$$x = 1 + \frac{a^2}{z^2} .$$

Equation E.11 can be used to derive an equation for circular duct diameter in terms of the length of a side for a square duct. Since

$$\theta = \frac{\pi}{4} \ln x,$$

then

$$x = e^{4\theta/\pi} .$$

Recalling the definition of x, then

$$1 + \frac{a^2}{z^2} = e^{4\theta/\pi} .$$

Therefore,

$$a = z \ (e^{4\theta/\pi} - 1)^{1/2},$$

or

$$d = 2z \ (e^{4\theta/\pi} - 1)^{1/2}. \qquad (E.12)$$

where z is not much larger than s or d.

Recalling Equation E.7 for $z >> d$ and $z >> s$,

$$\frac{s^2}{\pi} \simeq a^2.$$

Since $a = 2d$, then $a^2 = 4d^2$, and the equation becomes

$$\frac{s^2}{\pi} \simeq 4d^2.$$

Solving for duct diameter yields

$$d \simeq \frac{2s}{\sqrt{\pi}}. \tag{E.13}$$

Figure E.1 demonstrates the variation between d and s as given by Equations E.12 and E.13. As can be seen on the graph, the approximation for circular duct diameter as a function of square duct side length (Equation E.12) gives results equal to the exact equation (E.13) for values of $s < 200$ cm. Even after $s = 200$ cm, the divergence of the two methods is very slow. In fact, as the side length doubles from 200 to 400 cm, the difference between the curves is only about 5%. Therefore, for the duct diameters in question, it was possible to use the approximate relationship

$$d = \frac{2s}{\sqrt{\pi}}. \tag{E.14}$$

This means that the flux from a square duct with side lengths less than 200 cm can be estimated by the flux from a cylindrical duct, if the side length is given by

$$s = \frac{\sqrt{\pi}d}{2}. \tag{E.15}$$

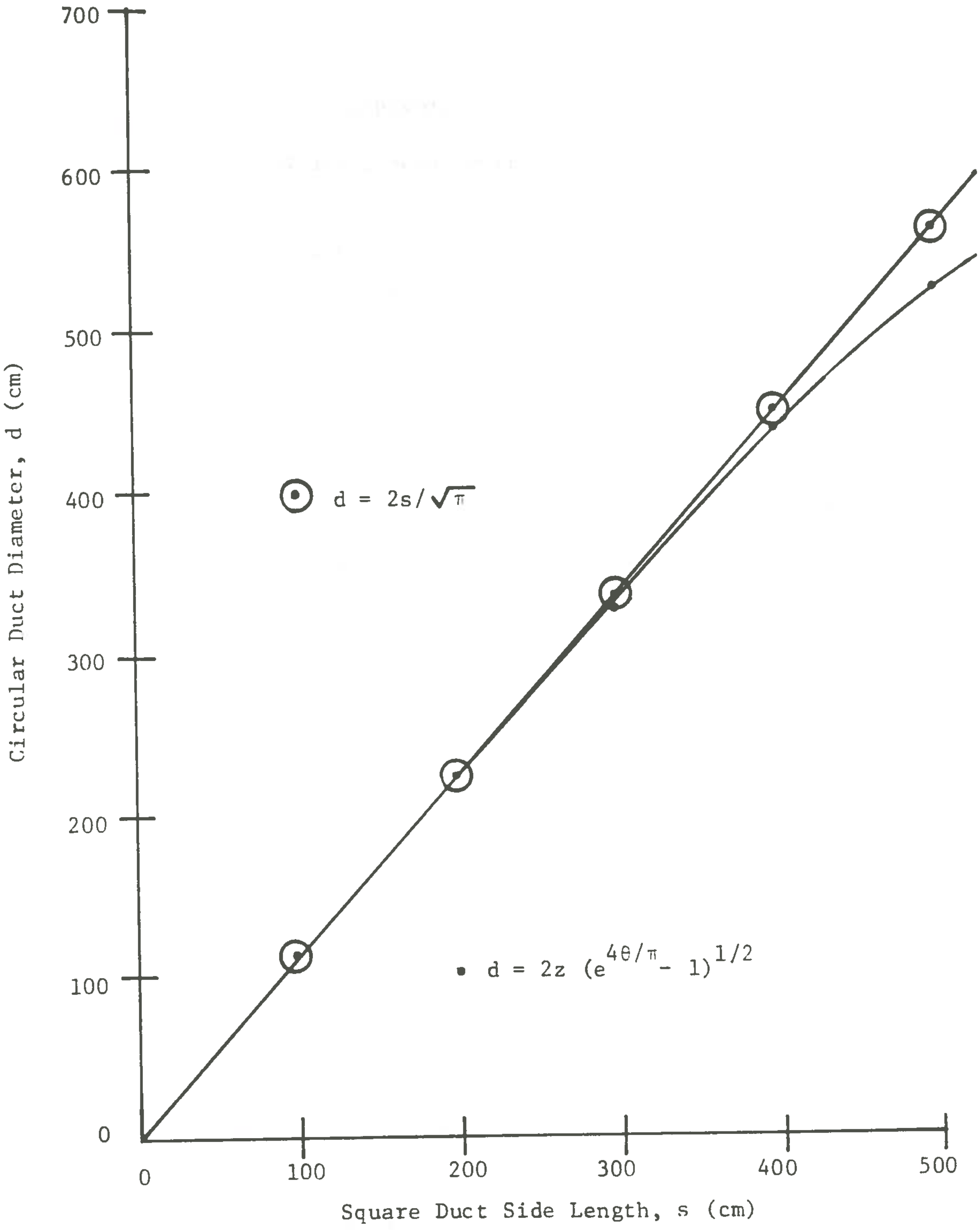

Figure E.1. Comparison of dimensions for circular and square ducts, based on shielding calculation methods.

APPENDIX F

Neutral Beam Dynamics

F.1. Phase Space Notations

In the sections which follow, it will be apparent to the reader that the three-dimensional, Cartesian coordinate system has been modified to deal with the problems presented by the phase space of the neutral beam. Phase space is a concept arising from the fact that the behavior of particles in the beam is governed by Hamilton's canonical equations. These equations can be derived from statistical thermodynamics, notably Lagrange's equations of motion. These state that

$$\frac{d}{dt}\left(\frac{\partial L}{\partial \dot{x}_i}\right) - \frac{\partial L}{\partial x_i} = 0 \; , \qquad \text{(F.1)}$$

where x_i = position of $i^{\underline{th}}$ particle,

$$\dot{x}_i = \frac{\partial x_i}{\partial t} \; ,$$

and L is the difference between the kinetic and potential energies of the assembly of particles.

The Hamiltonian is described as

$$H = \sum P_i \, x_i - L \; , \qquad \text{(F.2)}$$

where $P_i = \frac{\partial L}{\partial \dot{x}_i}$.

This relation reduces to

$$- \frac{\partial L}{\partial x_i} = \frac{\partial H}{\partial x_i} \qquad \text{(F.3)}$$

Using Equations F.1 and F.3, it is possible to develop Hamilton's canonical equations as

$$- \dot{p}_i = \frac{\partial H}{\partial x_i} \qquad \text{(F.4)}$$

and

$$\dot{x}_i = \frac{\partial H}{\partial p_i} \; . \qquad \text{(F.5)}$$

There are twice as many equations as there are degrees of freedom, f, for such a system. Thus, the motion of a particle in the beam can be represented as the trajectory of a point in 2f-dimensional space. This is the phase space, which consists of six dimensions for a three-dimensional beam. The Cartesian directions (x, y, and z) make up three of the dimensions; while the other three are related to particle momentum (x', y', and z'). This type of six-dimensional notation will be used in Chapter 4 and in this Appendix.

F.2. Geometrical Transport

As noted in Chapter 4, the matrices for the beam behavior downstream of a converging magnetic quadrapole lens are

$$\begin{pmatrix} x \\ x' \end{pmatrix} = \begin{pmatrix} A & B \\ C & D \end{pmatrix} \begin{pmatrix} x_1 \\ x_1' \end{pmatrix} \; .$$

More specifically, the matrices are

$$\begin{pmatrix} x \\ x' \end{pmatrix} = \begin{pmatrix} 1 & S \\ 0 & 1 \end{pmatrix} \begin{pmatrix} \cos\theta & \frac{1}{K}\sin\theta \\ -K\sin\theta & \cos\theta \end{pmatrix} \begin{pmatrix} x_1 \\ x_1' \end{pmatrix}, \tag{F.7}$$

where

$x' = \frac{dx}{dz}$,

S = free field distance downstream of magnet

$\theta = KL$

$K^2 = \frac{1}{B_r} \frac{dB_y}{dx}$,

L = magnet length,

B_r = particle rigidity,

B_y = field strength

and x_1 = position of beam of magnet entrance.

This compares well with the horizontal and vertical transfer matrices for beam transport in the injector system. Those matrices are

$$\begin{pmatrix} x_6 \\ x_6' \\ dp/p \end{pmatrix} = \begin{pmatrix} 1 & S & 0 \\ 0 & 1 & 0 \\ 0 & 0 & 1 \end{pmatrix} \begin{pmatrix} 1 & 0 & 0 \\ \frac{1}{\rho} \tan \mu_2 & 1 & 0 \\ 0 & 0 & 1 \end{pmatrix}$$

$$\begin{pmatrix} \cos \phi & \frac{\rho}{\delta} \sin \phi & \frac{\rho}{\delta^2} (1 - \cos \phi) \\ -\frac{\delta}{\rho} \sin \phi & \cos \phi & \frac{1}{\delta} \sin \phi \\ 0 & 0 & 1 \end{pmatrix}$$

$$\begin{pmatrix} 1 & 0 & 0 \\ \frac{1}{\delta} \tan \mu_1 & 1 & 0 \\ 0 & 0 & 1 \end{pmatrix} \begin{pmatrix} 1 & S_1 & 0 \\ 0 & 1 & 0 \\ 0 & 0 & 1 \end{pmatrix} \begin{pmatrix} x_1 \\ x_1' \\ dp/p \end{pmatrix} \qquad \text{(F.8)}$$

and

$$\begin{pmatrix} z_6 \\ z_6' \end{pmatrix} = \begin{pmatrix} 1 & S \\ 0 & 1 \end{pmatrix} \begin{pmatrix} 1 & 0 \\ -\frac{1}{\rho} \tan \mu_2 & 1 \end{pmatrix} \begin{pmatrix} \cos \psi & \frac{\rho}{\varepsilon} \sin \psi \\ -\frac{\varepsilon}{\rho} \sin \psi & \cos \psi \end{pmatrix}$$

$$\begin{pmatrix} 1 & 0 \\ -\frac{1}{\rho} \tan \mu_1 & 1 \end{pmatrix} \begin{pmatrix} 1 & S_1 \\ 0 & 1 \end{pmatrix} \begin{pmatrix} z_1 \\ z_1' \end{pmatrix}, \qquad \text{(F.9)}$$

where

S_1 = free-field distance from exit grid to first bending magnet,

ρ = radius of orbit with momentum p,

μ_1 = angle at which magnet entrance face is slanted with respect to perpendicular to p ordit,

μ_2 = exit face angle, similar to μ_1 in definition,

$\phi = \delta\theta = (1 - n)^{1/2}\ \theta,$

θ = magnet bending angle,

n = magnet field index

$= -\ (\frac{r}{B})\ \frac{dB}{dr}\ ,$

S = free-field distance from exit of magnet,

x_j = horizontal displacement,

z_j = vertical displacement,

$\psi = \varepsilon\theta = \sqrt{n}\ \theta.$

For the injector in question, $n = \frac{1}{2}$ and $\mu_1 = 0$. For the monoenergetic D° component of the beam, $\mu_2 = 0$ and $\Delta p/p = 0$. This results in a simplification of the above variables such that,

$$\varepsilon = \sqrt{n} = 1/\sqrt{2}$$

$$\delta = (1 - 1/2)^{1/2} = 1/\sqrt{2}$$

$$\psi = \sqrt{1/2}\ \ \theta = \theta/\sqrt{2}$$

$$\phi = (1 - 1/2)^{1/2}\ \theta = \sqrt{1/2}\ \theta = \theta/\sqrt{2}$$

$$\psi = \phi = \theta/\sqrt{2}$$

$$\tan \mu_1 = 0$$

and $$\tan \mu_2 = 0.$$

Accordingly, the matrices become,

$$\begin{pmatrix} x_6 \\ x'_6 \\ 0 \end{pmatrix} = \begin{pmatrix} 1 & S & 0 \\ 0 & 1 & 0 \\ 0 & 0 & 1 \end{pmatrix} \begin{pmatrix} 1 & 0 & 0 \\ 0 & 1 & 0 \\ 0 & 0 & 1 \end{pmatrix} \begin{pmatrix} \cos \frac{\theta}{\sqrt{2}} & \rho\sqrt{2} \sin \frac{\theta}{\sqrt{2}} & 2\rho\left(1 - \cos \frac{\theta}{\sqrt{2}}\right) \\ -\frac{1}{\rho\sqrt{2}} \sin \frac{\theta}{\sqrt{2}} & \cos \frac{\theta}{\sqrt{2}} & 2 \sin \frac{\theta}{\sqrt{2}} \\ 0 & 0 & 0 \end{pmatrix} \begin{pmatrix} 1 & 0 & 0 \\ 0 & 1 & 0 \\ 0 & 0 & 1 \end{pmatrix} \begin{pmatrix} 1 & S_1 & 0 \\ 0 & 1 & 0 \\ 0 & 0 & 1 \end{pmatrix} \begin{pmatrix} x_1 \\ x'_1 \\ 0 \end{pmatrix}$$

and

$$\begin{pmatrix} z_6 \\ z'_6 \end{pmatrix} = \begin{pmatrix} 1 & S \\ 0 & 1 \end{pmatrix} \begin{pmatrix} 1 & 0 \\ 0 & 1 \end{pmatrix} \begin{pmatrix} \cos \frac{\theta}{\sqrt{2}} & \rho\sqrt{2} \sin \frac{\theta}{\sqrt{2}} \\ -\frac{1}{\rho\sqrt{2}} \sin \frac{\theta}{\sqrt{2}} & \cos \frac{\theta}{\sqrt{2}} \end{pmatrix} \begin{pmatrix} 1 & 0 \\ 0 & 1 \end{pmatrix} \begin{pmatrix} 1 & S_1 \\ 0 & 1 \end{pmatrix} \begin{pmatrix} z_1 \\ z'_1 \end{pmatrix}$$

Since the momentum terms vanish in the horizontal displacement matrices, then the matrices can be reduced from 3 x 3 to 2 x 2. Also, for the identity matrix, I,

$$AI = A$$

where $$A = \begin{pmatrix} a & b \\ c & d \end{pmatrix}$$

and $$I = \begin{pmatrix} 1 & 0 \\ 0 & 1 \end{pmatrix}.$$

Therefore, the matrices become,

$$\begin{pmatrix} x \\ x' \end{pmatrix} = \begin{pmatrix} 1 & S \\ 0 & 1 \end{pmatrix} \begin{pmatrix} \cos \frac{\theta}{\sqrt{2}} & \rho\sqrt{2} \sin \frac{\theta}{\sqrt{2}} \\ \frac{1}{\rho\sqrt{2}} \sin \frac{\theta}{\sqrt{2}} & \cos \frac{\theta}{\sqrt{2}} \end{pmatrix} \begin{pmatrix} 1 & S_1 \\ 0 & 1 \end{pmatrix} \begin{pmatrix} x_1 \\ x_1' \end{pmatrix} \tag{F.10}$$

and

$$\begin{pmatrix} z \\ z' \end{pmatrix} = \begin{pmatrix} 1 & S \\ 0 & 1 \end{pmatrix} \begin{pmatrix} \cos \frac{\theta}{\sqrt{2}} & \rho\sqrt{2} \sin \frac{\theta}{\sqrt{2}} \\ \frac{1}{\rho\sqrt{2}} \sin \frac{\theta}{\sqrt{2}} & \cos \frac{\theta}{\sqrt{2}} \end{pmatrix} \begin{pmatrix} 1 & S_1 \\ 0 & 1 \end{pmatrix} \begin{pmatrix} z_1 \\ z_1' \end{pmatrix} \tag{F.11}$$

It is apparent from the above matrices that the horizontal and vertical displacements for this beam are identical. This will result in a beam with a square cross-sectional area, and will allow the generalization of the displacement matrices. Therefore, both matrices can be written in the form

$$\begin{pmatrix} y \\ y' \end{pmatrix} = \begin{pmatrix} A & B \\ C & D \end{pmatrix} \begin{pmatrix} y_o \\ y_o' \end{pmatrix}, \tag{F.12}$$

where y represents either x or z, with the subscript o to designate the beam at the accelerator grid. The other elements of the matrix are

$$A = \cos \frac{\theta}{\sqrt{2}} - \left(\frac{S}{\rho\sqrt{2}}\right) \sin \frac{\theta}{\sqrt{2}} ,$$

$$B = S_1 \cos \frac{\theta}{\sqrt{2}} + \rho\sqrt{2} \sin \frac{\theta}{\sqrt{2}} + S\left(\cos \frac{\theta}{\sqrt{2}} - \left(\frac{1}{\rho\sqrt{2}}\right) \sin \frac{\theta}{\sqrt{2}}\right),$$

$$C = - \left(\frac{1}{\rho\sqrt{2}}\right) \sin \frac{\theta}{\sqrt{2}} ,$$

and

$$D = \cos \frac{\theta}{\sqrt{2}} - \left(\frac{S_1}{\rho\sqrt{2}}\right) \sin \frac{\theta}{\sqrt{2}} .$$

It should be noted that in these terms, ρ is the D^+ beam bending radius and θ is the bending angle for the D^+ beam.

F.3. Emittance Methods

As mentioned in Chapter 4, emittance is merely a quantitative measure of the quality of a non-laminar beam. It is related to the projection on a plane of the volume in phase space occupied by the particles which constitute the beam. Since most beams are axially symmetrical or else have two planes of symmetry, then the beam can be considered symmetrical about the xz and yz planes. The y-plane emittance for such a beam is defined as

$$\varepsilon_y = \frac{S_{yy'}}{\pi} , \qquad \text{(F.13)}$$

where $S_{yy'}$ is the area in yy' space occupied by the particles of the beam at a given distance z along the beam.

The mathematical development of this method begins with the paraxial equation for a non-laminar particle beam. This equation defines the motion of the beam, and for the case considered in Chapter 4, takes the form

$$Y'' + K(s)Y = 0, \tag{F.14}$$

where Y is a reduced variable = $y\sqrt{\beta\gamma}$, and K(s) is a function of the distance of beam travels, s. K(s) includes both the external focusing force and the linear self-force. Also, $\beta\gamma$ is similar to the index of refraction in light optics.

The equation can be transformed into phase variables as follows. Let

$$Y = A\omega(s) \cos \left\{ \psi(s) + \phi \right\} , \tag{F.15}$$

where $\psi' = \frac{1}{\omega^2}$, and $\omega(s)$ is the beamlet half-angle divergence. Therefore,

$$Y' = A[\omega'(s) \cos \left\{ \psi(s) + \phi \right\} - \frac{1}{\omega(s)} \sin \left\{ \psi(s) + \phi \right\}]. \tag{F.16}$$

From this, Equation F.14 can be written as

$$A(\omega'' - \frac{1}{\omega^3}) \cos (\psi + \phi) + KA\omega \cos (\psi + \phi) = 0,$$

or more simply,

$$\omega'' + K\omega - \frac{1}{\omega^3} = 0. \tag{F.17}$$

To solve this equation, a relationship must be found between Y, Y', ω, ω', and A.

Rewriting Equation F.15 yields

$$\cos\left\{\psi(s) + \phi\right\} = \frac{Y}{A\omega(s)} .$$

Since

$$\cos^2 \phi + \sin^2 \phi = 1 ,$$

it follows that

$$\sin^2\left\{\psi(s) + \phi\right\} = 1 - \cos^2\left\{\psi(s) + \phi\right\}$$

$$= 1 - \frac{Y^2}{A^2\omega^2}$$

Therefore,

$$\sin\left\{\psi(s) + \phi\right\} = \left(1 - \frac{Y^2}{A^2\omega^2}\right)^{1/2} .$$

Making these substitutions, Equation F.16 becomes

$$Y' = A\left[\omega' \frac{Y}{A\omega} - \frac{1}{\omega}\left(1 - \frac{Y^2}{A^2\omega^2}\right)^{1/2}\right].$$

Solving this equation for A^2 yields

$$A^2 = \frac{Y^2}{\omega^2} + (Y^2 \omega'^2 - 2\omega\omega' YY' + \omega^2 Y'^2),$$

or

$$A^2 = \gamma_o Y^2 + 2\alpha_o YY' + \beta_o Y'^2 , \qquad \text{(F.18)}$$

where $\alpha_o = - \omega\omega'$,

$\beta_o = \omega^2$,

and $\gamma_o = \frac{1}{\omega^2} + \omega'^2 = \frac{1 + \alpha_o{}^2}{\beta_o}$

The resulting equation for A^2 represents an ellipse in the YY' plane (where Y can denote any direction). The size, eccentricity, and orientation of the ellipse depend on A and the coefficients α_o and β_o are merely functions of the variables ω and ω'. The area of the ellipse defined by this equation is

$$S = \pi A^2 (\beta_o \gamma_o - \alpha_o^2)^{-1/2} , \qquad \text{(F.19)}$$

where
$$\beta_o \gamma_o - \alpha_o^2 = \beta_o \left(\frac{1 + \alpha_o^2}{\beta_o}\right) - \alpha_o^2$$

$$= 1.$$

Therefore, $S = \pi A^2$.

At the beginning of the section, the emittance was defined as

$$\varepsilon = \frac{S}{\pi} .$$

From the above equation for ellipse area, it is apparent that

$$A^2 = \frac{S}{\pi} .$$

Therefore, emittance = $\varepsilon = A^2$.

It follows that

$$\varepsilon = \gamma_o Y^2 + 2\alpha_o YY' + \beta_o Y'^2 . \qquad \text{(F.20)}$$

From Figure F.1, it can be seen that $y_{o_{max}} = y_2$ and $\omega_o = y'_4$, where ω_o is the maximum initial half-angle divergence of the beam. For any ellipse, the area is given by

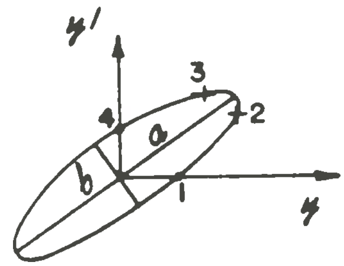

$$y_1 = \sqrt{\varepsilon/\gamma} \qquad y_3 = -\alpha\sqrt{\varepsilon/\gamma}$$

$$y_2 = \sqrt{\beta\varepsilon} = y_{max} \qquad y_3' = \sqrt{\varepsilon\gamma}$$

$$y_2' = -\alpha\sqrt{\varepsilon/\beta} \qquad y_4' = \sqrt{\varepsilon/\beta} = \omega_o$$

Figure F.1. Geometric properties of the phase space ellipse. (TNS Scoping Studies, Vol. V (1978), page 5.5-29).

$$S = \pi ab,$$

where a and b are the major and minor radii. However, for the orientation in Figure F.1, the area is given by

$$S = \pi\omega_o y_{o_{max}} .$$

The emittance is then

$$\varepsilon = \omega_o y_{o_{max}} , \qquad (F.21)$$

where

$$y = x \text{ or } z.$$

As can be seen, the emittance formula (Equation F.20) is in terms of initialized coefficients α_o, β_o, and γ_o, and reduced variables Y and Y'. However, the coefficients and variables of interest are α, β, γ, y and y'. To transform the emittance equation, it is necessary to invoke the geometrical transport matrices. Recall that Equation F.12 was

$$\begin{pmatrix} y \\ y' \end{pmatrix} = \begin{pmatrix} A & B \\ C & D \end{pmatrix} \begin{pmatrix} y_o \\ y'_o \end{pmatrix}.$$

Therefore,

$$y = Ay_o + By'_o$$

$$y' = Cy_o + By'_o \quad .$$

It follows that

$$y'_o\ (DA - BC) = Ay' - Cy$$

and
$$y_o = (DA - BC) = Dy - By',$$

where (DA - BC) reduces to unity.

This yields

$$y_o = Dy - By'$$

and
$$y'_o = Ay' - Cy.$$

Substituting the relations into Equation F.20 gives

$$\varepsilon = \gamma y^2 + 2\alpha yy' + \beta y^2, \qquad \text{(F.22)}$$

where
$$\alpha = - \gamma_o DB + \alpha_o\ (BC + DA) - AC\beta_o,$$

$$\beta = \gamma_o B^2 - 2\alpha_o BA + \beta_o A^2,$$

and
$$\gamma = \gamma_o D^2 - 2\alpha_o DC + \beta_o C^2.$$

In this equation, y and y' replaced the reduced variables Y and Y', respectively.

This is the emittance of the phase space ellipse with area

$$S = \pi\omega_o\ y_{o_{max}}.$$

Using these equations, it is possible to determine the shape, size, and orientation of the phase space ellipse at any distance (s) away from the ion source. The beam half-width will be

$$y_{max} = \sqrt{\beta\varepsilon} ,$$

where β is defined above.

A slight modification is sometimes used, since the beam phase space is nearly rectangular. This assumes that the phase space is composed of four quadrants, each of width equal to $y_{o_{max}}$ and height equal to ω_o. The resulting phase space area is

$$S = 4\omega_o \, y_{o_{max}} ,$$

and the emittance becomes

$$\varepsilon = \frac{4}{\pi} \omega_o \, y_{o_{max}} . \qquad \text{(F.23)}$$

This allows more of the beam to be included in the phase space area, which increases injector efficiency. To utilize this "effective" phase space area as given above, it is necessary to re-define ω_o and introduce a re-defined coefficient, β_o, into the previous calculations.

Therefore,

$$\omega_o \rightarrow \frac{4\omega_o}{\pi} ,$$

and

$$\omega_o = \sqrt{\frac{\varepsilon}{\beta_o}} \rightarrow \frac{4\omega_o}{\pi} = \sqrt{\frac{\varepsilon}{\beta_o}}$$

and

$$\frac{4\omega_o \beta_o}{\pi} = \sqrt{\varepsilon\beta_o} = y_{o_{max}} .$$

Therefore,

$$\beta_o = \frac{\pi y_{omax}}{4\omega_o} . \qquad \text{(F.24)}$$

APPENDIX G

DOT3.5 Modeling for Varying Beam Shapes

From Appendix E, the relationship between ducts of circular and square cross section was found to be

$$d = \frac{2s}{\sqrt{\pi}} ,$$

where d is the duct diameter, and s is the square duct side length < 200 cm. Table G.1 lists the duct diameters resulting from the square duct dimensions present in Table 4.1 of the text. Figure G.1 shows the duct models for the three cases. As can be seen, the variations in duct diameter are very small. It should be mentioned that the r_1 dimensions in Figure G.1 are one-half of the first wall opening sizes given in Table G.1. Also, the r_2 dimensions represent calculated values at Z = 544.5 cm. They are based on the slopes of the duct liner models between the first wall openings and the neutralizer exits.

As mentioned in Chapter 3, a duct which is not perpendicular to the plasma axis presents a difficult modeling situation. This is also true for ducts which are perpendicular, but whose walls taper inward or outward. However, due to the relatively small changes in duct diameter with respect to length, it was possible to develop models of the duct without increasing the problem size more than 43%.

Table G.1

Conversion of Square to Circular Dimensions
for Beam Transport Calculations

	Case I		Case II		Case III	
	s	d*	s	d*	s	d*
Initial Beam Size (cm)	34.8	39.3	34.8	39.3	34.8	39.3
Beam Size at Neutralizer:						
Entrance (cm)	48.7	55.0	48.7	55.0	57.2	64.5
Exit (cm)	33.0	37.2	34.4	38.8	47.2	53.3
First Wall Opening (cm)	30.6	34.5	39.0	44.0	30.4	34.3

* $d = 2s/\sqrt{\pi}$

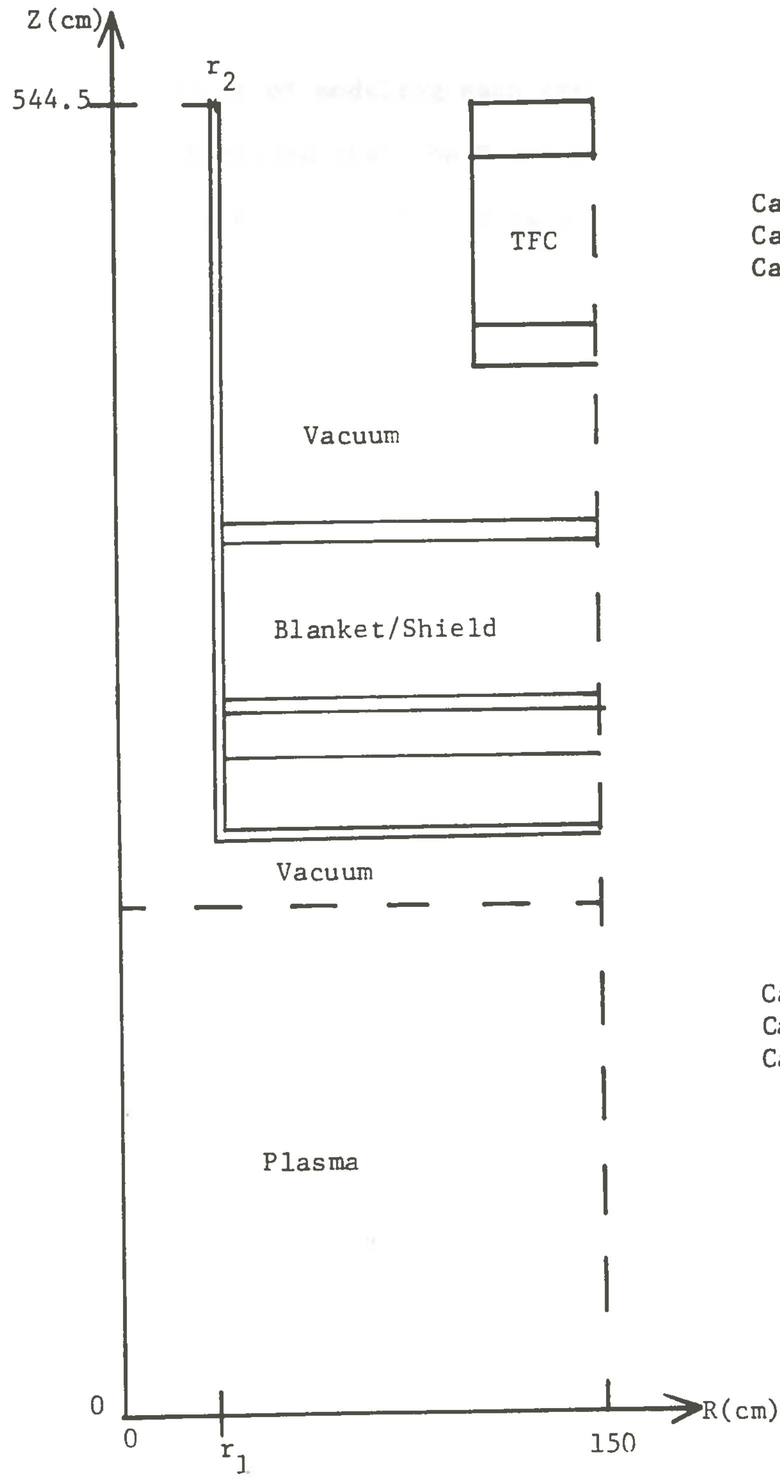

	r_2 (cm)
Case I	18.21
Case II	20.16
Case III	23.88

	r_1 (cm)
Case I	17.25
Case II	22.00
Case III	17.15

Figure G.1. Duct model developed to test the effects of beam transport calculations on DOT3.5 results.

The end result of modeling each case is given in Figure G.2. It must be remembered that the R and Z axes are not the same scale, nor does the R scale remain constant for all three models.

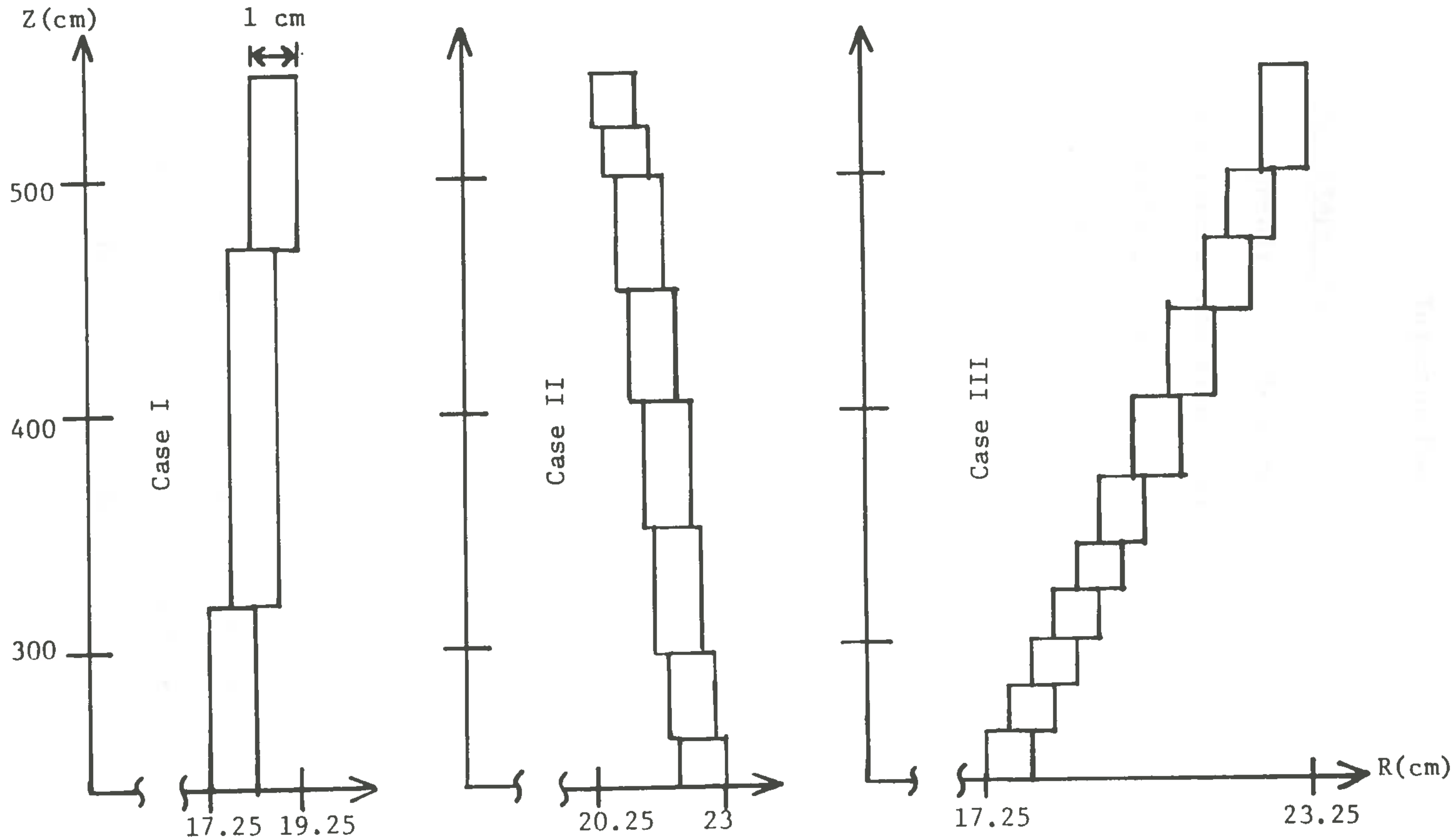

Figure G.2. Duct liner models developed for input to the 8∅ array of DOT3.5 to test the effects of beam transport calculations.

APPENDIX H

Injector Power Losses

H.1. Beam Scrape Off

In Appendix A, a development of the injector power flow for a TFTR-type reactor was given. Referring back to those equations, the author would like to introduce several new quantities in an effort to approximate the effects of particle scrape off in the beam duct. These are

$$P'_B = (1 - f_{so})P_B \tag{H.1}$$

and

$$P_{so} = P_B - P'_B \,, \tag{H.2}$$

where P_B is the usable power delivered to the plasma when no scrape off occurs (see Equation A.20).

P'_B is the same quantity if scrape off occurs,

and P_{so} is the power loss due to scrape off.

In Equation H.1, f_{so} represents the number of neutral particles which do not reach the plasma after leaving the second bending magnet, hence, f_{so} is the fraction scraped off. If it is assumed that the fraction of particles scraped off is inversely proportional to the duct area, then

$$f_{so} \propto \frac{1}{A_{duct}} = \frac{1}{S^2_{duct}} \,.$$

From this, it follows that at some maximum duct size, S_{max}, the number of particles lost will be at a minimum. Therefore, at S^2_{max},

$$f_{so} = f_{so_{min}} .$$

Using these relations, it is possible to calculate the scrape off fraction for any duct size by the following equation,

$$\frac{f_{so}}{f_{so_{min}}} = \frac{S^2_{max}}{S^2_{duct}} ,$$

or

$$f_{so} = f_{so_{min}} \left(\frac{S_{max}}{S_{duct}}\right)^2 , \qquad \text{(H.3)}$$

From Appendix A, for P_B = 40 Mw, P_{supply} = 84.8 Mw. Since the injector data remains constant regardless of the power requirements, it can be found that

$$P_{supply} = \frac{84.8 \text{ Mw}}{40 \text{ Mw}} P_B ,$$

or

$$P_{supply} = 2.12 \; P_B . \qquad \text{(H.4)}$$

From Equation H.1, it follows that

$$P_B = (1 - f_{so})^{-1} P'_B .$$

Therefore, the power supply required for a given beam power delivered to the plasma with some losses due to scrape off is

$$P_{supply} = 2.12\ (1 - f_{so})^{-1} P'_B \ . \qquad \text{(H.5)}$$

Substituting Equation H.3 into this relation gives

$$P_{supply} = 2.12\ [1 - f_{so_{min}}\ (\frac{S_{max}}{S_d})^2]^{-1} P'_B \ . \qquad \text{(H.6)}$$

Equation H.6 is especially important, since it allows a correlation between changes in duct size and changes in the amount of power supplied to the injector.

H.2. Dissociative Collisions

Another possible source of power losses is present in the injector system. This involves collisions between the energetic particles of the neutral beam and molecules of deuterium gas. As mentioned in Chapter 2, the deuterium is bled into the neutralizer portion of the injector as a source of electrons. This results in the neutralization of about 30% of the D^+ beam, with excess gas flowing toward the plasma. After leaving the second bending magnet, the D^o beam must pass through this gas as it travels through the beam duct.

The first step in determining the impact of the collisions is to find the number of gas particles per cm^3 present in the neutralizer. As a workable case, it was assumed that the gas is distributed uniformly throughout the duct, but does not enter the plasma chamber. Also, no gas flows back toward the ion source. Therefore, the gas density is

$$n = N/V_d \qquad \text{(H.7)}$$

where N = number of gas molecules in beam duct

and V_d = beam duct volume.

From the Ideal Gas Law,

$$pV = NRT,$$

where V = volume of gas,

p = absolute pressure of gas,

T = absolute temperature of gas,

and R = constant

$= 82.06$ atm.-cm^3-gm mole^{-1}-°K^{-1}.

This equation can be rewritten as

$$N = pV/RT. \qquad \text{(H.8)}$$

or

$$N = \dot{g}t/RT, \qquad \text{(H.9)}$$

where $\dot{g}$ = gas flow out of the neutralizer (Torr-ℓ-sec^{-1})

and t = reactor ignition time (sec).

The volume of the beam duct will be approximated using the configuration shown in Figure H.1. This geometry yields

$$V_d = \frac{1}{3} L \, (S_i^2 + S_i S_o + S_o^2), \qquad \text{(H.10)}$$

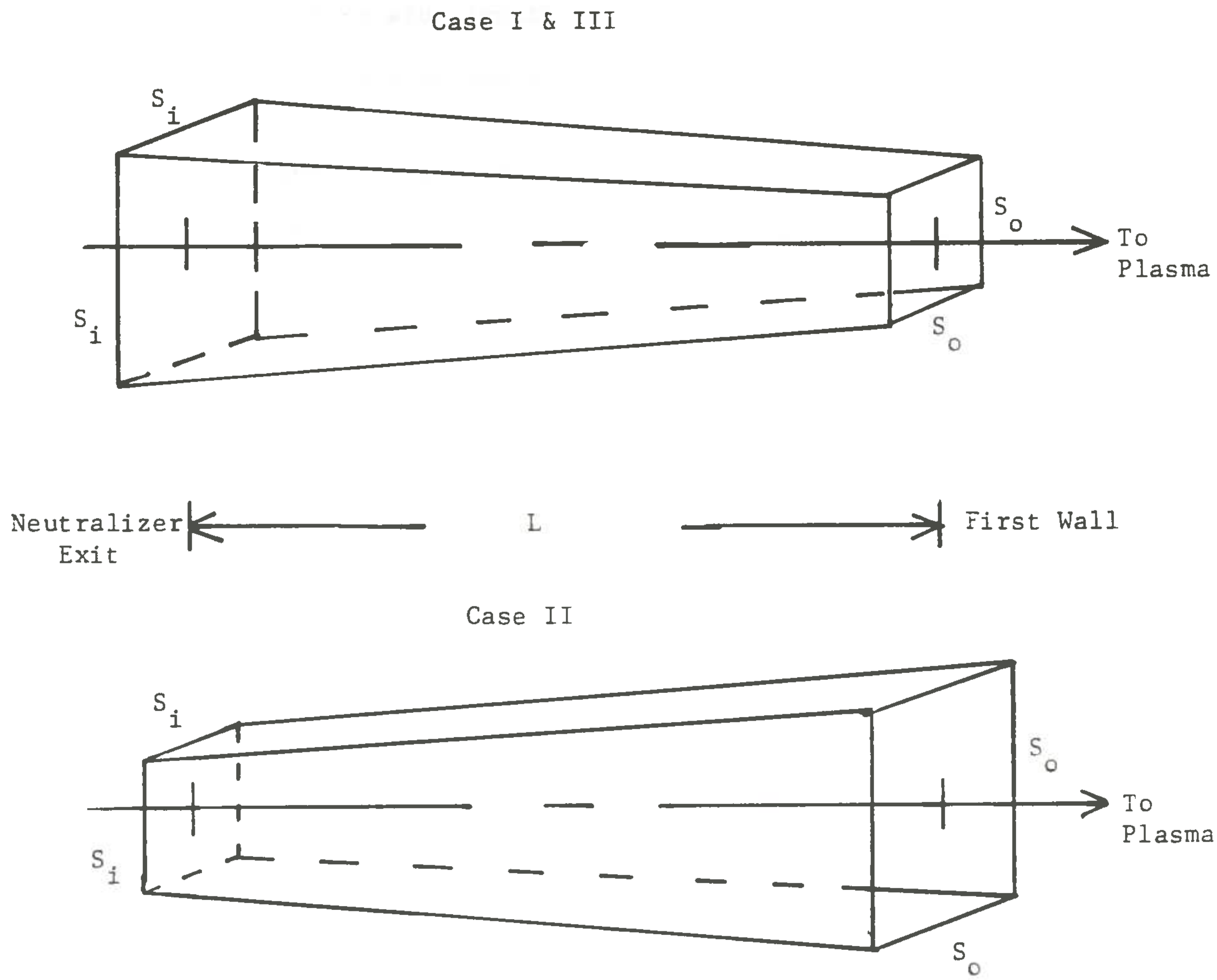

S_i = duct side length at neutralizer

S_o = duct side length at first wall

Figure H.1. Geometrical approximations used to calculate the volumes of beam ducts resulting from the beam transport calculations.

where L = duct length,

S_i = side length at neutralizer exit,

and S_o = side length at 1st wall opening.

For a reactor ignition time of 5 seconds, and a gas temperature of 60°F, the results of Equations H.7, H.9, and H.10 are given in Table H.1. The cases used are the same as those in Table 4.1.

Once the gas density in the duct had been determined, it was possible to select a method of calculating its impact. As mentioned in Chapter 5, the method selected was taken from Kammash (Ref. 49). This method makes use of binary collision theory to approximate neutral deuteron heating of a deuterium plasma. It is questionable whether this is the appropriate method to calculate beam energy losses, however, it should be adequate for determination of penetration effects.

The following values were used for deuteron-deuteron collisions:

$$\alpha = \frac{2.00 \times 10^{2}}{kT} ,$$

$$\beta = 1.73 \times 10^{-15} \frac{n^{1/2}}{(kT)^{3/2}} ,$$

and

$$\gamma = 1.49 \times 10^{-32} \frac{n}{(kT)^{2}} ,$$

Table H.1

Duct Gas Loading Data for Beam Transport Calculation Methods

Case	I	II	III
Neutralizer Exit, S_i (cm)	33.0	34.4	47.2
First Wall Opening, S_o (cm)	30.6	39.0	30.4
Duct Volume, V_d (cm^3)	6.78 (05)	6.04 (05)	7.04 (05)
Gas Flow, $\dot{g}$ (Torr-ℓ-sec^{-1})	68.5	74.0	142.0
Gas Quantity, N (molecules)	1.15 (16)	1.22 (16)	2.34 (16)
Gas Density, $\underline{n}$ (molecules-cm^{-3})	1.69 (10)	2.02 (10)	3.38 (10)

where n is given in Table H.1 for each case, and kT is the energy of the target molecules in KeV.

For deuterium gas at 60°F (288.7°K), target energy is 2.48×10^{-5} KeV. This results in a value of 8.065×10^{6} for α, with the values of β and γ as shown in Table H.2 for each case.

According to Kammash's development (Ref. 49), if $\beta^2 << 1$, then binary collision theory will give a decent approximation for low energy target particles. Since $\alpha >> 1$, the probable energy loss for a Maxwellian plasma is

$$L \simeq \frac{\pi}{\mu} \left(\frac{e_1 e_2}{\nu}\right)^2 \left[\frac{2m}{m + M} \phi(R) - Re^{-R^2}\right] \ln \left(\frac{1}{\beta^2}\right). \qquad \text{(H.14)}$$

In this equation,

$\phi(R)$ is the error function

$$= \frac{2}{\sqrt{\pi}} \int_0^R e^{-t^2} \, dt,$$

and $R^2 = \frac{M}{2kT} \nu^2$ (or $R = \sqrt{E/kT}$).

Also, μ is the reduced mass,

m and M are masses of beam and target particles, respectively,

e_1 and e_2 are beam and target charges, respectively,

and ν is the speed of the beam particle.

For the situation in question, the beam energy (E) is 150 KeV. Therefore, E >> kT and so, R >> 1. This causes the exponential term in Equation H.14 to become vanishingly small, and forces the error function to unity. Equation H.14 reduces to

$$L \simeq \frac{\pi}{\mu} \left(\frac{e_1 e_2}{\nu}\right)^2 \left(\frac{2m}{m + M}\right) \ln \left(\frac{1}{\beta^2}\right) . \qquad \text{(H.15)}$$

For purposes of comparison, the author used this equation to calculate the percent difference energy losses for Cases II and III with respect to Case I. Case I was selected as the Base Case, since it has the lowest gas density in the beam duct. To make the comparison, it was only necessary to solve the equation

$$\Delta_{a-b}\% = \frac{L_a - L_b}{L_b} = \frac{L_a}{L_b} - 1 ,$$

where a represents Case I and b represents either Case II or III.

Since all factors in Equation H.15, except β, are constant for all cases, then the above difference formula yields

$$\Delta_{a-b}\% = \frac{\ln (1/\beta_a^2)}{\ln (1/\beta_b^2)} - 1 . \qquad \text{(H.16)}$$

Table H.2 shows the results of Equation H.16.

Using the previously derived injector power flow equations, it is possible to estimate the effects of $\Delta_{a-b}\%$ on the heating system. From these equations,

$$P_B' = (1 - f_{so_{min}})P_B ,$$

Table H.2

Dissociative Collision Parameters for Beam Transport Calculation Methods

Case	I	II	III
β	1.82 (-03)	1.99 (-03)	2.57 (-03)
γ	4.10 (-13)	4.90 (-13)	8.18 (-13)
$\Delta_{a-b}\%$	0	+ 1.4	+ 5.8

where P_B is the beam power before scrape off,

and P_B' is the beam power delivered to the plasma.

To account for collision losses, let

$$P_B = (1 - f_c)P_{M2} , \qquad (H.17)$$

where P_{M2} is the beam power at the exit of the second bending magnet,

and f_c is the fractional collision loss $= \Delta_{a-b}\%/100\%$.

This substitution yields

$$P_B' = (1 - f_{so}) (1 - f_c)P_{M2} ,$$

or

$$P_{M2} = P_B' (1 - f_{so})^{-1} (1 - f_c)^{-1} . \qquad (H.18)$$

Equation H.4 states that for a system with no beam particle losses or energy losses between the exit of the second bending magnet and plasma chamber,

$$P_{supply} = 2.12 P_B .$$

If such losses occur, then the equation must be rewritten as

$$P_{supply} = 2.12 P_{M2} ,$$

where P_{M2} is defined by Equation H.18.

Therefore,

$$P_{supply} = 2.12\ (1 - f_{so})^{-1}\ (1 - f_c)^{-1} P_B'. \qquad (H.19)$$

The equations developed here are also applicable during the burn phase of a beam-driven reactor. In such a situation, f_c will be about 35 to 40% greater due to the effect of higher volumes of gas in the duct.

VITA

Joe L. Burton was born in Blytheville, Arkansas on March 17, 1951. Upon graduation from Blytheville Sr. High School in 1969, he was admitted to Mississippi State University. He received a Bachelor of Science degree in Nuclear Engineering from that institution in 1973. Upon graduation, he was employed by Gulf States Utilities Company as an engineer. Since 1975, he has pursued, on a part-time basis, the degree of Master of Science in Nuclear Engineering at Louisiana State University.

He is currently employed by Gulf States Utilities Company as Maintenance Engineer at Louisiana Generating Station and is a registered Professional Engineer in Texas and Louisiana. He is married to the former Karin K. Zinn of Essen, West Germany.

LOUISIANA STATE UNIVERSITY

THE GRADUATE SCHOOL

APPLICATION FOR ADMISSION TO CANDIDACY FOR A MASTER'S DEGREE

) the Graduate Council:

I HEREBY apply for admission to candidacy for the degree of Master of Science at the ommencement of December 1979. Degrees held (colleges and dates) Bachelor of Science, Mississippi State University, 1973

lajor Department (Graduate) Nuclear Engineering Minor None

ist all LSU graduate courses that apply toward this degree:

Major Courses: NS 4494, NS 4570, NS 4991, NS 4992, NS 7520, NS 7527, NS 7528, NS 7530, NS 7555, NS 7995, NS 8000

2. Minor Courses: None

pecial conditions, or transferred credits, if any: None

rogram for the remainder of the period of study (List courses by Majors and Minors) Major: NS 8000

Title of Thesis: An Analysis of the Neutral Beam Injector Penetrations in Current Tokamak Fusion Reactor Designs

Recommended:

Major professor: Robert E. Miles (signed)

Dr. Robert E. Miles (type name in full)

Dept. Head: William F. Curry (signed)

Applicant: Joe Lynn Burton (signed)

Joe Lynn Burton (type name in full)

September 21, 1979 (date)

Approved by the Dean of the Graduate School James G. Traynham